UNIVERSITY OF TURKU

Dynamic Modelling and Simulation of a Single-Effect Absorption Chiller

Mechanical Engineering/Faculty of Technology

Master's thesis

Author(s):
Nilotpaul Saha

26.06.2026

Turku

Master's thesis

Subject: Mechanical Engineering
Author(s): Nilotpaul Saha
Title: Dynamic Modelling and Simulation of a Single-Effect Absorption Chiller
Supervisor(s): University Lecturer Jari Böling
Number of pages: 112 pages
Date: 26.06.2026

Abstract

Absorption refrigeration systems driven by low-grade thermal energy offer a sustainable alternative to conventional vapour-compression chillers, replacing the mechanical compressor with a thermochemical cycle driven primarily by waste heat (Florides *et al.*, 2003). The lithium bromide–water (LiBr/H_2O) working pair is well-suited for single-effect cooling, operating effectively with heat source temperatures of 75–120 °C and making it directly compatible with marine waste heat applications (Salmi *et al.*, 2017a). Because absorption machines possess large thermal inertia, dynamic simulation is essential for predicting transient responses, evaluating part-load performance, and designing effective control strategies (Kohlenbach and Ziegler, 2008a). This thesis presents the development and successful implementation of a dynamic, lumped-parameter simulation model for a single-effect LiBr/H_2O absorption chiller in MATLAB/Simulink. Following the state-space framework of Wen *et al.*, (2019), the model is governed by coupled first-order ordinary differential equations derived from conservation of mass, species, and energy. Thermodynamic properties are computed using the correlations of Pátek and Klomfar, (2006) and Florides *et al.*, (2003), with specific heat capacity derived as the analytical temperature derivative of the enthalpy correlation to ensure thermodynamic consistency. To overcome the numerical instability of the baseline model, two architectural modifications were introduced: a dynamic condenser pressure scaling mechanism proportionally linked to instantaneous liquid refrigerant mass, and an 8-stage spatially discretised counter-flow solution heat exchanger with finite thermal mass at each node. These modifications yield a robust, fully functional integrated model. Simulation results across three parametric scenarios demonstrate stable transient convergence, with a baseline COP of 0.718 (driving heat input is waste heat) establishing a computationally efficient tool for predicting absorption chiller behaviour under varying operational conditions.

Key words: Absorption chiller, dynamic modelling, Simulink, state-space model, transient simulation, thermodynamic instability, waste heat recovery.

Acknowledgements

I would like to express my sincere gratitude to my supervisor, Jari Böling, for his continuous guidance, constructive feedback, and dedicated support throughout every stage of this thesis.

I would also like to thank Anam Tahir for generously giving her time and providing valuable assistance with the development of the simulation model.

I am grateful to the University of Turku and the Faculty of Technology for providing the academic environment, resources, and opportunity to undertake this research.

Finally, and most deeply, I would like to thank my loved one for her unwavering patience and encouragement, my parents for their unconditional support throughout my studies, and my little brother for always being a source of motivation. I also extend my gratitude to everyone who has supported me along the way.

Nilotpaul Saha

Turku, June 2026

Use of Artificial Intelligence Tools

In the preparation of this thesis, the AI assistant Perplexity (Perplexity AI, June 2026) was used minimally to assist with grammar correction and sentence structure refinement. All technical content, including the dynamic simulation model, state-space formulation, thermodynamic equations, numerical results, Simulink architecture, figures, and scientific analysis presented in this thesis, is entirely the author's own work. The author takes full responsibility for the accuracy and integrity of the entire contents of this thesis.

List of Abbreviations

Abbreviation	Description
CFD	Computational Fluid Dynamics
COP	Coefficient of Performance
DAE	Differential-Algebraic Equation
EES	Engineering Equation Solver
GUI	Graphical User Interface
HEX	Heat Exchanger
HVAC	Heating, Ventilation, and Air Conditioning
LiBr	Lithium Bromide
LPM	Lumped-Parameter Model
MATLAB	Matrix Laboratory
NIST	National Institute of Standards and Technology
ODE	Ordinary Differential Equation
REFPROP	Reference Fluid Thermodynamic and Transport Properties Database
SHX	Solution Heat Exchanger

Subscript	Description
abs	Absorber
con	Condenser
eva	Evaporator
gen	Generator
in	Inlet
out	Outlet
ref	Refrigerant (water, H_2O)
shx	Solution heat exchanger
sol	Solution (LiBr/H_2O mixture)
strong	Strong solution (high LiBr concentration)
weak	Weak solution (low LiBr concentration)

Table of contents

1 Introduction

1.1 Background and Motivation

Global energy demand continues to rise alongside growing environmental concerns over greenhouse gas emissions and the consumption of fossil fuels. In the maritime sector, cruise ships and large commercial vessels represent a particularly energy-intensive domain, where onboard energy consumption is broadly divided between propulsion and hotel services — the latter encompassing heating, ventilation, and air conditioning (HVAC), refrigeration, lighting, and passenger amenities (Salmi *et al.*, 2017). HVAC systems alone constitute a significant fraction of the total hotel load, and these cooling demands are conventionally met by vapour-compression refrigeration systems, which require substantial electrical power generated by engines burning marine fuel (Salmi *et al.*, 2017).

A substantial portion of the fuel energy consumed by marine engines is rejected as low- to medium-grade waste heat through exhaust gases, jacket cooling water, and other thermal streams. This waste heat, typically available at temperatures between 75 °C and 275 °C depending on the source, represents a significant recoverable energy resource that is largely unutilised in conventional vessel designs (Salmi et al., 2017). Absorption refrigeration technology offers a compelling pathway to recover this thermal energy directly for cooling purposes, thereby reducing the electrical load on the ship's generators and improving overall energy efficiency.

Absorption chillers operate on a thermochemical cycle that replaces the energy-intensive mechanical compressor of a conventional vapour-compression system with a thermally driven absorption-desorption process, requiring only a small solution pump for mechanical work (Florides *et al.*, 2003). The coefficient of performance (COP) of an absorption chiller is defined as the ratio of useful cooling output to the thermal energy input at the generator — the driving waste heat (Florides *et al.*, 2003). This thermal COP typically falls in the range of 0.6–0.8 for a single-effect LiBr/H_2O cycle (Kohlenbach and Ziegler, 2008a; Evola *et al.*, 2013), a value that may appear low to a reader familiar with heat pump COPs, which routinely exceed 3 (Salmi *et al.*, 2017). The distinction lies in the energy currency used in the denominator. A heat pump or vapour-compression chiller COP is defined as cooling output divided by electrical power input, making electricity a high-grade, costly energy form (Salmi *et al.*, 2017). In an absorption chiller, the denominator is thermal energy from a waste heat stream that is already available as

a by-product of engine operation and would otherwise be rejected to the environment at no productive use (Florides *et al.*, 2003; Salmi *et al.*, 2017). When the heat source is considered freely available, the effective electrical COP of the absorption system becomes very large, since the only electrical consumption is the small solution pump, which draws negligible power compared to a mechanical compressor of equivalent cooling capacity (Wen *et al.*, 2019). The thermal COP of 0.6–0.8 should therefore be understood not as a measure of inefficiency, but as a statement of how effectively each unit of waste heat is converted into useful cooling — a fundamentally different and complementary metric to the electrical COP used for conventional systems (Kohlenbach and Ziegler, 2008a).

The lithium bromide–water (LiBr/H_2O) working pair is among the most widely adopted for single-effect absorption cooling applications. In this pair, water acts as the refrigerant and lithium bromide serves as the absorbent. The cycle is well-suited to heat source temperatures in the range of 75–120 °C, making it directly compatible with low- and medium-grade waste heat streams available in marine and industrial environments (Florides *et al.*, 2003). Furthermore, LiBr/H_2O systems operate at sub-atmospheric pressures, carry no ozone depletion potential, and produce chilled water at temperatures suitable for air-conditioning applications above 0 °C (Wen *et al.*, 2019).

The viability of LiBr/H_2O absorption chillers for marine waste heat recovery has been demonstrated in existing literature. Salmi et al. (2017) investigated the use of ship engine waste heat as the energy source for an absorption refrigeration system and confirmed meaningful fuel savings and emissions reductions. Similarly, Garimella, Brown and Nagavarapu, (2011) modelled waste-heat-driven absorption systems for naval vessel applications, demonstrating the technical feasibility of such integration. These studies collectively establish a strong motivation for the continued development of accurate and reliable simulation tools for absorption chiller systems in marine contexts.

1.2 The Need for Dynamic Modelling

The performance analysis of absorption chillers has historically been approached using steady-state thermodynamic models, which assume constant operating conditions and are well-suited to design-point calculations, component sizing, and cycle optimisation (Kohlenbach and Ziegler, 2008a). However, in real operational environments — particularly in marine applications where waste heat availability fluctuates with engine load, and cooling demand

varies with ambient temperature and occupancy — the chiller is rarely operating at its design point. Part-load operation, start-up transients, and responses to disturbances are the norm rather than the exception.

Absorption chillers possess inherently large thermal inertia due to the significant mass of their internal heat exchangers, the stored LiBr/H_2O solution, and the external heat transfer media (Kohlenbach and Ziegler, 2008a). This thermal mass means that the time required for the system to reach a new steady state following a change in operating conditions can be on the order of 15 minutes or more — far slower than an equivalent vapour-compression system (Kohlenbach and Ziegler, 2008a). Steady-state models are fundamentally incapable of capturing this transient behaviour and therefore cannot provide time-dependent information required for control system design, system integration studies, or accurate prediction of energy performance over a realistic operating cycle.

Dynamic simulation models, formulated as systems of differential equations incorporating mass storage, thermal inertia, and transport delays, address this limitation directly. They allow the prediction of temperature, pressure, mass, and concentration profiles within each component as functions of time, enabling the evaluation of start-up behaviour, response to load changes, and the stability of proposed control strategies (Evola *et al.*, 2013). Dynamic modelling also exposes numerical challenges inherent to the stiff, highly nonlinear nature of the governing equations — challenges that must be systematically addressed to produce a stable and reliable simulation tool. The development of such a tool for the single-effect LiBr/H_2O absorption chiller is the central contribution of this thesis.

1.3 Objectives of the Thesis

Objective 1: Development of the Dynamic Mathematical Model

To derive the complete set of governing dynamic equations for each component of the single-effect LiBr/H_2O absorption chiller — generator, absorber, condenser, evaporator, solution heat exchanger, throttle valves, and solution pump — based on the strict conservation of mass, species, and energy. This includes the formulation of a thermodynamically consistent property library computing LiBr/H_2O solution vapour pressure, enthalpy, specific heat capacity, and density using the correlations of Pátek and Klomfar, (2006), Florides *et al.*, (2003), and Kaita, (2001), and recovering refrigerant saturation temperatures from pressure using the Antoine equation.

Objective 2: Implementation and Simulation of the Dynamic Model in Simulink

To implement the dynamic model in the MATLAB/Simulink environment, incorporating the necessary architectural modifications to the baseline state-space framework of Wen *et al.*, (2019) — specifically the dynamic condenser pressure scaling mechanism and the 8-stage spatially discretised counter-flow solution heat exchanger to achieve numerical stability and sustained self-consistent cyclic operation from cold-start conditions. Unlike the baseline framework of Wen et al. (2019), in which mass balance is satisfied by assuming that mass flows are always algebraically in balance rather than through any dynamic feedback mechanism, the present modifications allow the solver to maintain physical consistency during severe transients.

Objective 3: Subsystem-Level Verification

To adopt a modular, block-by-block construction methodology in Simulink, where each subsystem — generator, absorber, condenser, evaporator, solution heat exchanger, throttle valves, and pump — is individually built, verified for correct thermodynamic behaviour, and tested in isolation before integration into the dynamic model. This approach ensures that errors are identified and resolved at the component level before system-level simulation.

Objective 4: Investigation and Analysis of Results

To simulate the dynamic behaviour of the fully integrated model under a baseline operating condition and across three parametric scenarios representing realistic variations in marine operating conditions — changes in hot water inlet temperature, cooling water inlet temperature, and chilled water return temperature — and to analyse the resulting transient and steady-state performance in terms of temperatures, pressures, component masses, solution concentrations, heat transfer rates, and coefficient of performance (COP).

1.4 Scope and Limitations

1.4.1 Scope

The scope of this thesis is confined to the dynamic modelling and simulation of a single-effect $LiBr/H_2O$ absorption chiller under conditions relevant to marine waste heat recovery applications.

Single-effect cycle only.

The model is restricted to the single-effect LiBr/H_2O cycle architecture, consisting of one generator, one condenser, one evaporator, one absorber, one solution heat exchanger, one solution pump, and two throttling devices. Double-effect, triple-effect, or hybrid configurations are outside the scope of this work. The single-effect cycle was selected because it is the most commonly deployed configuration for low-temperature heat sources in the 75–120 °C range, including ship engine waste heat (Florides *et al.*, 2003; Salmi *et al.*, 2017), and because the Wen et al. (2019) state-space framework upon which this thesis is based was specifically developed for this configuration.

Lumped-parameter spatial representation.

Each component is treated as a single lumped control volume with one uniform temperature, pressure, and concentration at any instant. Spatial gradients within components are not resolved. This is consistent with the approach of Wen et al. (2019), Evola et al. (2013), and Kohlenbach and Ziegler (2008), and is well-justified for control-oriented dynamic modelling where computational efficiency is prioritised over spatial resolution. The sole exception is the solution heat exchanger, which is spatially discretised into 8 nodes to accurately capture counter-flow thermal transport delays and internal heat recovery dynamics.

Open-loop transient response analysis.

The simulation concerns the open-loop transient behaviour of the chiller model under prescribed external inputs — hot water supply temperature and flow rate, cooling water temperature and flow rate, and chilled water flow rate. No feedback control loops, PID controllers, or model-predictive control schemes are implemented. The open-loop framework is the necessary first step before any control design can be attempted, as it establishes the baseline dynamic characteristics of the plant (Misenheimer and Terry, 2017).

MATLAB/Simulink as the simulation platform.

The model is implemented exclusively in MATLAB/Simulink, using its graphical block diagram environment for signal routing and integration, and MATLAB function blocks for all thermodynamic property calculations. The choice of Simulink is motivated by its suitability for stiff dynamic systems modelling and its widespread adoption in control engineering research, making it well-positioned for future integration of control algorithms (Gediz Ilis, Demir and Saha, 2021).

Thermodynamic property formulations.

Thermophysical properties of the $LiBr/H_2O$ solution are computed using the polynomial correlations of Pátek and Klomfar (2006) and Florides et al. (2003). Specific heat capacity is derived as the exact analytical temperature derivative of the Florides et al. (2003) enthalpy correlation to ensure strict thermodynamic consistency. Properties of pure water as refrigerant — vapour enthalpy and liquid enthalpy — are computed from the curve-fit correlations of Florides et al. (2003), with saturation temperature recovered from pressure using the Antoine equation.

1.4.2 Limitations

No crystallisation modelling.

Lithium bromide solutions can crystallise at high concentrations and low temperatures, which would physically block the machine and cause operational failure. The model does not incorporate crystallisation detection or prevention logic. While guardrails clamp the LiBr concentration within the valid property range of the correlations used (Kaita, 2001; Florides *et al.*, 2003), no thermodynamic crystallisation boundary is explicitly enforced or tracked during simulation.

Negligible heat losses and pipe dynamics.

The model assumes all components are perfectly insulated — no heat losses to the ambient environment from component walls, piping, or connecting components are accounted for. Fluid transport delays and pressure drop in the interconnecting pipework between components are also neglected, with the exception of the hydrostatic head term in the throttle valve, which is computed dynamically from the instantaneous generator solution mass and density.

Lumped-parameter approximation.

Each main unit is modelled as a single well-mixed control volume with uniform temperature, pressure, and concentration. Spatial gradients within components — such as film flow non-uniformity in the absorber or refrigerant maldistribution in the evaporator — are not captured. This is a standard and well-accepted assumption in dynamic absorption chiller modelling (Kohlenbach and Ziegler, 2008a; Evola *et al.*, 2013).

No experimental validation.

The model is not validated against physical hardware measurements. Validation is limited to consistency with the published steady-state reference data of Wen *et al.*, (2019) and thermodynamically expected directional trends across the parametric scenarios tested.

Simplified density correlation.

The $LiBr/H_2O$ solution density is computed using a simplified empirical polynomial correlation. While adequate over the nominal operating concentration range, this correlation may carry reduced accuracy at the extremes of the operating envelope and does not account for pressure dependence of liquid density.

2 Literature Review

2.1 Principles of Absorption Refrigeration

Refrigeration is the process of transferring heat from a low-temperature reservoir to a high-temperature reservoir — a direction that is thermodynamically non-spontaneous and therefore requires work input of some form. In a conventional vapour-compression refrigeration system, this work is supplied as shaft work by a mechanically driven compressor. The absorption refrigeration cycle achieves the same thermodynamic outcome but replaces the energy-intensive mechanical compressor with a thermochemical compression process driven almost entirely by heat (Florides *et al.*, 2003).

The theoretical basis of the absorption cycle lies in the strong affinity between a refrigerant vapour and a liquid absorbent. The refrigerant is absorbed exothermically into the absorbent at low pressure in the absorber; the resulting liquid solution is pumped to high pressure with negligible work input because liquids are nearly incompressible; and the refrigerant is then desorbed endothermically from the solution at high pressure by the addition of external heat in the generator (Florides *et al.*, 2003). The net effect is that refrigerant vapour is transported from the low-pressure side to the high-pressure side of the cycle using thermal energy as the primary driving input, with only a small fraction of electrical energy consumed by the solution pump (Wen *et al.*, 2019).

2.1.1 The Single-Effect LiBr/H_2O Cycle

The single-effect LiBr/H_2O absorption chiller is built around five principal heat exchanger units — the generator, condenser, evaporator, absorber, and solution heat exchanger (SHX) — together with a solution pump and two throttling devices (Kohlenbach and Ziegler, 2008a; Evola *et al.*, 2013; Wen *et al.*, 2019). The system operates across two pressure levels: a high-pressure side comprising the generator and condenser, and a low-pressure side comprising the evaporator and absorber. Because water is the refrigerant, both sides operate at sub-atmospheric absolute pressures — the high side typically in the range of 6–10 kPa and the low side around 0.7–1.0 kPa under standard operating conditions (Kohlenbach and Ziegler, 2008a; Muhumuza and Strachan, 2010).

With reference to Figure 1, the operational sequence begins at the absorber. The weak solution — dilute in LiBr and rich in water refrigerant, with a LiBr mass fraction of

approximately 55 wt.% — leaves the absorber as a saturated liquid at low pressure and low temperature (Wen et al., 2019). The solution pump raises this liquid to the high-side pressure, consuming negligible work relative to the total thermal input (Salmi et al., 2017). The pressurised weak solution then traverses the solution heat exchanger, where it is preheated by the hot strong solution returning from the generator, before entering the generator (Evola et al., 2013; Wen et al., 2019).

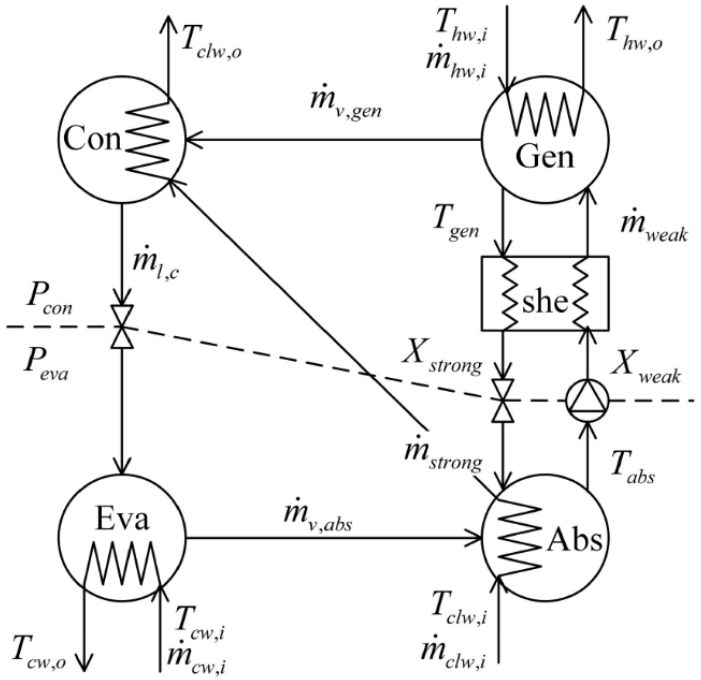

Figure 1: Schematic diagram of the single-effect LiBr/H_2O absorption chiller cycle

Source for figure: Wen et al. (2019), Figure 1

In the generator, external thermal energy — supplied by a low- to medium-grade heat source — typically hot water, steam, or recovered waste heat in marine and industrial applications — drives water vapour out of the weak solution until a strong solution with a LiBr mass fraction of approximately 60 wt.% remains (Wen et al., 2019; Kohlenbach & Ziegler, 2008). The liberated refrigerant vapour passes to the condenser, where it rejects heat to the cooling water circuit and condenses to saturated liquid. The strong solution flows back through the solution heat exchanger, transferring heat to the incoming weak solution, before being throttled to the low-side pressure and re-entering the absorber (Evola et al., 2013). The condensed liquid refrigerant throttles isenthalpically through the refrigerant expansion valve into the evaporator, where it absorbs heat from the chilled water circuit and evaporates, producing the useful cooling effect. The resulting refrigerant vapour returns to the absorber, where it is reabsorbed

into the arriving strong solution, releasing the combined heat of condensation and dilution to the cooling water and closing the cycle (Evola *et al.*, 2013; Wen *et al.*, 2019; Zhou *et al.*, 2023).

Mass and Species Balances

For each unit in the cycle, the overall mass balance and the LiBr species balance is satisfied simultaneously. Applied to the generator and absorber — which are the two units in which the solution concentration changes — these take the following general form. For any unit X containing LiBr solution, the overall mass conservation equation is (Wen et al., 2019; Evola et al., 2013; Zhou et al., 2023)

$$\frac{dM_X}{dt} = \dot{m}_{\text{in}} - \dot{m}_{\text{out}} - \dot{m}_v \qquad (2.1)$$

where M_X is the total solution mass stored in unit X, $\dot{m}_{\text{in}}$ and $\dot{m}_{\text{out}}$ are the inlet and outlet solution mass flow rates, and $\dot{m}_v$ is the mass flow rate of refrigerant vapours either leaving or entering the generator and absorber units respectively. The species balance for LiBr — which neither evaporates nor condenses and therefore accumulates only in the solution — is (Wen et al., 2019; Zhou et al., 2023)

$$\frac{d(M_X w_X)}{dt} = \dot{m}_{\text{in}} w_{\text{in}} - \dot{m}_{\text{out}} w_{\text{out}} \qquad (2.2)$$

where w_X, w_{in}, and w_{out} are the LiBr mass fractions of the solution inside the unit, at the inlet, and at the outlet, respectively. Because LiBr is non-volatile, it does not appear in the vapour mass flow term. At steady state, the time derivatives vanish, and these two equations together enforce a global salt balance across the entire solution circuit

$$\dot{m}_w w_w = \dot{m}_s w_s \qquad (2.3)$$

where $\dot{m}_w$ and $\dot{m}_s$ are the mass flow rates of the weak and strong solutions, and w_w and w_s are their respective LiBr mass fractions (Wen et al., 2019; Salmi et al., 2017). The refrigerant mass balance at steady state requires that the mass flow of vapour generated in the generator equals the mass flow evaporated in the evaporator and reabsorbed in the absorber

$$\dot{m}_r = \dot{m}_s - \dot{m}_w \qquad (2.4)$$

where $\dot{m}_r$ is the mass flow rate of pure water vapour (the refrigerant) circulating in the refrigerant loop.

Energy Balances

The energy balance for each unit is derived by applying the first law of thermodynamics to the respective control volume, including both the enthalpy transported by mass flows and any heat exchanged with external fluid circuits. For the generator, the energy balance is (Wen et al., 2019; Evola et al., 2013; Zhou et al., 2023)

$$\frac{d(M_g h_g)}{dt} = \dot{m}_w h_w - \dot{m}_s h_s - \dot{m}_r h_r + Q_{\text{gen}} \qquad (2.5)$$

where h_g, h_w, h_s, and h_r are the specific enthalpies of the solution in the generator, the incoming weak solution, the outgoing strong solution, and the outgoing refrigerant vapour, respectively, and Q_{gen} is the heat input from the external hot water circuit. For the absorber, the sign of the vapour flow reverses — refrigerant vapour enters and is absorbed — giving (Wen et al., 2019; Evola et al., 2013)

$$\frac{d(M_a h_a)}{dt} = \dot{m}_s h_s + \dot{m}_r h_r - \dot{m}_w h_w - Q_{\text{abs}} \qquad (2.6)$$

where Q_{abs} is the heat rejected to the cooling water circuit. For the condenser and evaporator, the refrigerant-side energy balances take the respective forms (Wen et al., 2019; Zhou et al., 2023)

$$\frac{d(M_c h_c)}{dt} = \dot{m}_r h_{r,\text{in}} - \dot{m}_l h_l - Q_{\text{con}} \qquad (2.7)$$

$$\frac{d(M_e h_e)}{dt} = \dot{m}_l h_l - \dot{m}_r h_{r,\text{out}} + Q_{\text{eva}} \qquad (2.8)$$

where $\dot{m}_l$ is the mass flow rate of liquid refrigerant entering the evaporator from the condenser via the refrigerant expansion valve, and h_l is its specific enthalpy (equal to the condenser outlet enthalpy since the throttle is adiabatic). At steady state, all time derivatives in Equations (2.5)–(2.8) are zero, and the four unit balances reduce to the global first-law relation for the complete cycle (Evola et al., 2013; Kohlenbach & Ziegler, 2008)

$$Q_{\text{gen}} + Q_{\text{eva}} = Q_{\text{abs}} + Q_{\text{con}} \qquad (2.9)$$

where the negligible pump work has been omitted. This steady-state relation serves as the fundamental consistency check against which the equilibrium output of the dynamic model is verified in Chapter 6.

2.1.2 Thermodynamic Performance and the Coefficient of Performance

The thermal performance of the absorption chiller is quantified by the coefficient of performance (COP), defined as the ratio of the useful cooling effect delivered at the evaporator to the driving heat input at the generator

$$\mathrm{COP} = \frac{Q_{\mathrm{eva}}}{Q_{\mathrm{gen}}} \qquad (2.10)$$

This definition follows directly from the steady-state global energy balance established in Equation (2.9): since $Q_{\mathrm{gen}} + Q_{\mathrm{eva}} = Q_{\mathrm{abs}} + Q_{\mathrm{con}}$, the COP expresses what fraction of the total thermal input to the cycle is directed toward the useful refrigeration effect rather than rejected to the cooling water circuit (Evola et al., 2013; Kohlenbach & Ziegler, 2008). For the standard single-effect LiBr/H_2O cycle under design conditions, the COP typically falls in the range of 0.6 to 0.8 (Modelling, Implementation and Simulation, 2010; Evola et al., 2013). While this is considerably lower than the COP of a vapour-compression system — typically 3 to 5 for a comparable temperature lift — the driving input is thermal rather than electrical, making absorption systems advantageous wherever low-cost or waste heat is available (Salmi et al., 2017).

A theoretical upper bound on the COP is obtained by applying the second law of thermodynamics to the reversible absorption cycle, treating the system as a combination of a reversible heat engine operating between the generator and the ambient rejection temperature, and a reversible refrigeration cycle operating between the ambient and the evaporator temperature. This yields the Carnot COP for the absorption chiller, which serves as the thermodynamic upper bound on thermal cooling performance — analogous to, but distinct from, the electrical COP used for heat pumps (Muhumuza and Strachan, 2010)

$$\mathrm{COP}_{\mathrm{max}} = \frac{T_g - T_a}{T_g} \cdot \frac{T_e}{T_a - T_e} \qquad (2.11)$$

where T_g, T_a, and T_e are the absolute temperatures of the generator, absorber, and evaporator, respectively, with the condenser assumed to operate at the same temperature as the absorber.

The first factor represents the Carnot efficiency of the driving heat engine; the second is the Carnot COP of the refrigeration sub-cycle (Modelling, Implementation and Simulation, 2010). Real cycles operate well below this upper bound because of irreversibilities including finite heat transfer temperature differences across each unit, viscous pressure losses in the solution circuit, and irreversible throttling across both expansion valves (Evola et al., 2013; Kohlenbach & Ziegler, 2008).

The COP is sensitive to the operating temperatures of all four units. Increasing the generator temperature T_g improves desorption and raises COP up to an optimum, beyond which excess concentration of the strong solution risks crystallisation and COP begins to decline (Salmi et al., 2017; Wen et al., 2019). Lowering the condenser and absorber temperature T_a — by using colder cooling water — consistently improves COP by reducing the concentration lift required of the solution circuit. Raising the evaporator temperature T_e similarly improves COP, which is why absorption chillers perform better at moderate chilled-water setpoints (e.g. 7–12 °C) than at very low setpoints (Salmi et al., 2017; Evola et al., 2013). These temperature dependencies are governed by the pressure–temperature–concentration relationships of the LiBr/H_2O solution, which are examined in Section 2.1.4.

2.1.3 The Role of the Solution Heat Exchanger

The solution heat exchanger (SHX) or (SHE) is a recuperative device interposed between the strong solution leaving the generator and the weak solution leaving the absorber. Its function is to transfer heat from the hot strong solution — which leaves the generator at approximately 90 °C and must be cooled before re-entering the absorber — to the cold weak solution entering the generator at approximately 35 °C, thereby reducing the generator heat input required and improving the overall COP (Wen et al., 2019; Evola et al., 2013).

In the foundational model of Wen et al. (2019), the SHX is treated as a quasi-steady component characterised by a fixed thermal effectiveness

$$\varepsilon_{\mathrm{SHX}} = \frac{T_{\mathrm{s,in}} - T_{\mathrm{s,out}}}{T_{\mathrm{s,in}} - T_{\mathrm{w,in}}} \qquad (2.12)$$

where $T_{\mathrm{s,in}}$ is the strong solution temperature at the generator outlet, $T_{\mathrm{s,out}}$ is the strong solution temperature at the SHX outlet, and $T_{\mathrm{w,in}}$ is the weak solution temperature at the absorber outlet.

This algebraic formulation carries no thermal storage and assumes the SHX reaches equilibrium instantaneously with its inlet conditions (Wen et al., 2019).

In the present work, however, the SHX is modelled using a more physically detailed approach. Rather than a single-stage effectiveness model, the SHX is discretised into eight cascaded counter-flow stages connected in series, replicating a counter-flow configuration at the macro level through discrete spatial discretisation. Each individual stage is modelled as a dynamic two-node lumped system. The governing energy balance for the hot-side node temperature $T_{h,i}$ and cold-side node temperature $T_{c,i}$ within each stage is

$$mc_p \frac{dT_{h,i}}{dt} = \dot{m}_s c_p \left(T_{h,i-1} - T_{h,i}\right) - UA_{\text{stage}} \left(T_{h,i} - T_{c,i}\right) \qquad (2.13)$$

$$mc_p \frac{dT_{c,i}}{dt} = \dot{m}_w c_p \left(T_{c,i+1} - T_{c,i}\right) + UA_{\text{stage}} \left(T_{h,i} - T_{c,i}\right) \qquad (2.14)$$

where m [kg] is the lumped fluid mass per stage, c_p [J/kg·K] is the specific heat capacity, and UA_{stage} [W/K] is the inter-stage thermal conductance. The inter-stage heat transfer rate is therefore

$$\dot{Q}_i = UA_{\text{stage}} \left(T_{h,i} - T_{c,i}\right) \qquad (2.15)$$

Each stage contains two Simulink integrators — one for the hot-side node and one for the cold-side node — making the eight-stage SHX a 16th-order dynamic subsystem with 16 state variables. This discretised dynamic approach is physically superior to the single-stage effectiveness model because it resolves the spatial temperature distribution along the SHX length and captures the transient thermal storage within the heat exchanger fluid mass (Evola et al., 2013).

2.2 The LiBr/H_2O Working Pair and Thermodynamic Properties

2.2.1 Thermodynamic Suitability and the Dühring Rule

The thermodynamic behaviour of a LiBr/H_2O absorption chiller is governed at every operating point by the coupled relationship between solution vapour pressure P, solution temperature T, and lithium bromide mass concentration x (wt%). Because water is the only volatile component, vapour–liquid equilibrium (VLE) requires equality of the chemical potential of water in both phases, directly coupling these three variables into the state surface $P =$

$f(T, x)$ (Kaita, 2001; Pátek and Klomfar, 2006). This surface governs refrigerant desorption in the generator, re-absorption in the absorber, and the pressure levels at both the condenser and evaporator. Accurate representation of this surface — and its associated enthalpy and entropy fields — is therefore a prerequisite for any meaningful dynamic simulation (Florides *et al.*, 2003).

The Dühring Rule and the Physical Basis of the p–T–x Surface

The empirical observation known as Dühring's rule states that the boiling-point temperature of a LiBr/H_2O solution at constant composition is approximately a linear function of the boiling point of pure water at the same pressure (Chua *et al.*, 2000)

$$T_{\text{sol}}(P, x) = A_D(x)\ T_{\text{dew}}(P) + B_D(x) \qquad (2.16)$$

where $A_D(x)$ is the Dühring gradient and $B_D(x)$ is the Dühring intercept, both functions of concentration only. Inverting Eq. (2.16), the vapour pressure of the solution follows directly

$$P(T, x) = P_{\text{sat}}\left(\frac{T - B_D(x)}{A_D(x)}\right) \qquad (2.17)$$

where P_{sat} is the saturation pressure of pure water at the argument temperature. Equation (2.17) is the analytical foundation of the Dühring chart, in which straight concentration-labelled lines connect solution operating points to the corresponding pure-water dew-point temperatures (Florides et al., 2003). As concentration increases, these lines shift to higher solution temperatures at the same pressure, meaning a more concentrated solution must be heated to a higher generator temperature to desorb the same mass of refrigerant — the mechanism that directly couples generator temperature to COP (Pátek and Klomfar, 2006).

The thermodynamic origin lies in vapour-pressure depression: dissolved LiBr ions reduce the chemical potential of water in the liquid phase, suppressing the equilibrium vapour pressure relative to pure water at the same temperature (Kaita, 2001). The linear relationship expressed by the Dühring rule, Eq. (2.16), is a remarkably accurate approximation over the full operating range of single-effect absorption machines, and Eq. (2.17) inherits this linear structure by direct inversion over the full operating range of single-effect absorption machines and forms the structural backbone of all three property formulations adopted in this work (Kaita, 2001; Florides et al., 2003; Pátek and Klomfar, 2006).

2.2.2 Property Correlations

Three formulations are employed in the present work. Each is presented below with its governing equations, valid range, and the specific role it plays in the Simulink model.

2.2.2.1 Kaita (2001)

Kaita (2001) developed extended property equations for the LiBr/H_2O system covering 40–65 wt% and 40–210 °C by assembling vapour-pressure data from three independent experimental campaigns: Iyoki and Uemura (1989), Jeter et al. (1992), and Feuerecker et al. (1993), supplemented at low temperatures by McNeely's tabulated values. The resulting formulation was validated simultaneously against all three datasets — a rigorous multi-source validation not performed by any prior correlation (Kaita, 2001).

Vapour pressure is obtained via a dew-point intermediate. The solution dew-point temperature T_D (°C) is computed from (Kaita, 2001)

$$T_D = \sum_{i=0}^{2}\sum_{j=0}^{3} A_{ij}(x-40)^j T^i \qquad (2.18)$$

with coefficients given in Table 2.2. Vapour pressure is then recovered through the Antoine-type relation for pure water (Kaita, 2001)

$$P = k_0 + \frac{k_1}{T_D + 273.15} + \frac{k_2}{(T_D + 273.15)^2} \qquad (2.19)$$

with $k_0 = 7.05$, $k_1 = -1603.54$, $k_2 = -104{,}095.5$ (P in kPa).

Table 1 - Kaita (2001) dew-point equation coefficients A_{ij} for Eq. (2.19)

j	A_{0j}	A_{1j}	A_{2j}
0	-9.133128×10^{0}	9.439697×10^{-1}	-7.324352×10^{-5}
1	-4.759724×10^{-1}	-2.882015×10^{-3}	-1.556533×10^{-5}
2	-5.638171×10^{-2}	-1.345453×10^{-4}	1.992657×10^{-6}
3	1.108418×10^{-3}	5.852133×10^{-7}	-3.924205×10^{-8}

Equation (2.18) achieved the lowest dew-point standard deviation of any published correlation — 0.23 °C overall — compared with 0.56–1.50 °C for McNeely's formulation and 0.47–1.36 °C for Patterson and Perez-Blanco's equation (Kaita, 2001). This advantage is most

significant at concentrations above 55 wt% and temperatures above 120 °C, precisely the conditions encountered in the generator of the modelled chiller.

Specific heat capacity is based on Rockenfeller's differential scanning calorimeter data (65–205 °C, 40–65 wt%), which Kaita (2001) identified as the most representative among four independent measurement campaigns

$$C_p(T, x) \;=\; (A_0 + A_1\, x) \;+\; (B_0 + B_1\, x)\; T \qquad (2.20)$$

with $A_0 = 3.462023$, $A_1 = -2.679895 \times 10^{-2}$, $B_0 = 1.3499 \times 10^{-3}$, $B_1 = -6.55 \times 10^{-6}$ (kJ kg⁻¹ °C⁻¹). Integrating Eq. (2.20) with corrections for the heat of dilution yields the solution enthalpy in closed form (Kaita, 2001)

$$H(T, x) \;=\; (A_0 + A_1\, x)\; T^{0.5} \;+\; (B_0 + B_1\, x)\; T^2 \;+\; D_0 + D_1\, x + D_2\, x^2 + D_3\, x^3 \qquad (2.21)$$

with $D_0 = 162.81$, $D_1 = -6.0418$, $D_2 = 4.5348 \times 10^{-3}$, $D_3 = 1.2053 \times 10^{-3}$ (kJ kg⁻¹), referenced to liquid water and 50 wt% solution at 0 °C. Agreement with Feuerecker et al.'s (1993) independently calculated enthalpy values is within 1% on average across the valid range (Kaita, 2001).

2.2.2.2 Florides et al. (2003)

Florides et al. (2003) assembled and documented a self-consistent set of correlations specifically for the design and simulation of single-effect LiBr/H₂O chillers. Their concentration equations for the weak solution leaving the absorber and the strong solution leaving the generator are formulated as direct polynomials in solution temperature and system pressure (Florides et al., 2003)

$$x \;=\; A + B\,T + C\,T^2 + D\,T^3 + E \cdot P + F \cdot P^2 \qquad (2.22)$$

where T is solution temperature (°C) and P is pressure (kPa), with coefficients fitted separately for absorber and generator conditions. While less thermodynamically rigorous than the Kaita (2001) or Pátek and Klomfar (2006) formulations, Eq. (2.22) possesses one decisive computational advantage: it is algebraically invertible. Given T and P at any operating point, the equilibrium concentration is recovered directly without iteration (Florides et al., 2003). This is essential for Simulink integration, where implicit iteration over property equations at each solver time step introduces algebraic loops that increase stiffness and threaten numerical

stability, particularly during the severe concentration transients of cold-start events. The correlations are valid over approximately 45–70 wt% and 60–180 °C, fully covering the operating range of single-effect machines (Florides et al., 2003).

2.2.2.3 Pátek and Klomfar (2006)

Pátek and Klomfar (2006) developed the most rigorous property formulations currently available for the LiBr/H_2O system, valid from 273 to 500 K and 0 to 75 wt%, based on a critically assessed dataset of 1,449 primary experimental data points from 16 independent sources. A structurally unique feature of their equations is the guaranteed explicit transition to pure-water properties as $x \to 0$, which no prior polynomial-in-wt% correlation achieves (Pátek and Klomfar, 2006). Their vapour pressure equation embeds the Dühring rule in an exponential functional form

$$p(T,x) \;=\; p'(\theta)\cdot\exp\left[\sum_{i=1}^{8} a_i \; x^{m_i}(0.4-x)^{n_i}\left(\frac{T}{T_c}\right)^{t_i}\right] \qquad (2.23)$$

where $\theta = C(x)\,T + D(x)$ is the Dühring-shifted temperature, $p'(\theta)$ is the IAPWS-95 saturation pressure of pure water at θ, and $T_c = 647.096$ K (Pátek and Klomfar, 2006). The coefficients and exponents are given in Table 2.

Table 2 - Pátek and Klomfar (2006) pressure equation coefficients for Eq. (2.25)

i	m_i	n_i	t_i	a_i
1	3	0	0	-2.41303×10^{2}
2	4	5	0	1.91750×10^{7}
3	4	6	0	-1.75521×10^{8}
4	8	3	0	3.25430×10^{7}
5	1	0	1	3.92571×10^{2}
6	1	2	1	-2.12626×10^{3}
7	4	6	1	1.85127×10^{8}
8	6	0	1	1.91216×10^{3}

The RMS deviation of Eq. (2.23) across all 1,449 primary data points is 2.1% — the lowest of any published pressure correlation for this system (Pátek and Klomfar, 2006). The corresponding enthalpy and entropy equations share the same functional structure, using IAPWS-95 pure-water reference quantities $h'(T)$ and $s'(T)$ (Pátek and Klomfar, 2006)

$$h(T,x) \;=\; (1-x)\,h'(T) \;+\; h_c\sum_{i=1}^{30} a_i \; x^{m_i}(0.4-x)^{n_i}\left(\frac{T_c}{T-T_0}\right)^{t_i} \qquad (2.24)$$

$$s(T,x) \;=\; (1-x)\,s'(T) \;+\; s_c \sum_{i=1}^{29} a_i \;x^{m_i}(0.4-x)^{n_i}\left(\frac{T_c}{T-T_0}\right)^{t_i} \qquad (2.25)$$

where $T_0 = 221$ K, $h_c = 37{,}548.5$ J mol^{-1}, and $s_c = 79.3933$ J mol^{-1} K^{-1}, with full coefficient tables provided in Pátek and Klomfar (2006). Maximum enthalpy deviations from this formulation are 8 kJ kg^{-1} relative to Kaita (2001) and 4 kJ kg^{-1} relative to Feuerecker et al. (1993) — both well within the experimental uncertainty of the source data (Pátek and Klomfar, 2006).

2.2.3 The Crystallisation Constraint

The p–T–x surface is not merely thermodynamic bookkeeping — it is operationally critical because of crystallisation risk. If the LiBr concentration anywhere in the solution circuit exceeds the solubility limit at the local temperature, solid LiBr hydrates precipitate and may irreversibly block heat exchanger tubes, valves, and the solution heat exchanger (Florides et al., 2003). The crystallisation boundary defines the maximum safe concentration as a function of temperature, commonly approximated as (Florides et al., 2003)

$$x_{\text{cryst}}(T) \;=\; \alpha_0 + \alpha_1\,T + \alpha_2\,T^2 \qquad (2.26)$$

At a typical absorber outlet of 40 °C, the maximum safe concentration is approximately 63–65 wt%; at 90 °C generator conditions, it rises to approximately 68–70 wt%, providing a working margin above the nominal strong-solution concentration of 62–64 wt% in a well-designed single-effect machine (Florides et al., 2003; Pátek and Klomfar, 2006). Crystallisation risk is most acute during dynamic transients — cold starts, abrupt load reductions, and hot-water supply failures — when the generator may temporarily operate at reduced temperature while carrying a concentrated strong solution. The present Simulink model enforces the constraint of Eq. (2.26) as a real-time check within the concentration state block, flagging violations during all simulated transient scenarios.

Property Selection for the Present Model

The three formulations are assigned distinct roles according to their respective computational and accuracy characteristics:

- **Kaita (2001)** (Eqs. 2.18–2.21) provides vapour pressure, enthalpy, and heat capacity for all state-point calculations within the generator, absorber, condenser, and evaporator. It is selected for its lowest published dew-point standard deviation (0.23 °C) and explicit validation across the 40–210 °C, 40–65 wt% range relevant to the modelled chiller (Kaita, 2001).

- **Florides et al. (2003)** (Eq. 2.22) provides the algebraically direct concentration inversion $x = f(T, P)$ at both the absorber and generator, eliminating implicit property iterations within the solver loop that would introduce stiffness and instability during transient events (Florides et al., 2003).

- **Pátek and Klomfar (2006)** (Eqs. 2.23–2.25) serve as the primary reference benchmark for validating steady-state operating points. Their superior accuracy (2.1% RMS pressure deviation) and IAPWS-95 thermodynamic consistency make them the most reliable standard against which model outputs can be assessed, while their computational overhead — 30-term summations with molar-fraction conversions and IAPWS-95 lookups — makes them unsuitable for real-time integration within the solver loop (Pátek and Klomfar, 2006).

All three formulations agree to within experimental uncertainties over the core single-effect operating window (50–63 wt%, 60–170 °C); the distinction between them therefore matters chiefly near the crystallisation boundary, where Kaita's (2001) high-concentration accuracy and Florides et al.'s (2003) computational simplicity together confer the greatest combined advantage.

2.3 Dynamic Modelling of Absorption Chillers

Steady-state models of absorption chillers assume quasi-equilibrium at all operating points and are adequate for annual energy calculations and component sizing (Florides et al., 2003). However, they cannot predict transient responses, cold-start behaviour, or control system interactions — the core objectives of this thesis. Because absorption chillers possess large thermal inertia due to the mass of their heat exchangers, internal solution inventory, and structural components, the time to reach a new steady state after a change in operating conditions typically exceeds 10–15 minutes (Kohlenbach and Ziegler, 2008a). Dynamic modelling is therefore essential for any meaningful analysis of part-load performance, system integration, or control strategy design.

2.3.1 Lumped-Parameter Modelling Framework

The dominant approach in the dynamic absorption chiller literature is the lumped-parameter method, in which each unit — generator, absorber, condenser, evaporator — is treated as a single well-mixed control volume characterised by a uniform temperature, pressure, and LiBr concentration at each time step (Wen et al., 2019). This 0-D spatial approximation is justified by the relatively slow time constants of the thermal and mass processes involved and dramatically reduces computational cost compared to distributed or CFD approaches.

The benchmark architecture for lumped-parameter dynamic modelling was established by (Kohlenbach and Ziegler, 2008a, 2008b). Their model introduces three fundamental dynamic mechanisms: solution transport delay between the generator and absorber, mass storage in the vessel sumps, and thermal storage distributed between an external part (responding to heat carrier temperatures) and an internal part (responding to refrigerant and solution temperatures). This split thermal mass formulation was a key architectural innovation, allowing the model to capture the distinct heat transfer dynamics on both sides of each heat exchanger tube bundle without requiring detailed spatial resolution. Experimental verification against a 10 kW commercial chiller demonstrated dynamic temperature deviations of approximately 10–25 seconds, with total time to new steady state of approximately 15 minutes following a 10 K generator inlet step (Kohlenbach and Ziegler, 2008b).

Evola et al. (2013) extended this framework by adding variable strong-solution mass flow rate as a function of pressure difference and solution level — a feature absent from Kohlenbach and Ziegler's original model — and validated the result against continuous real-world operational data from a solar-assisted installation over an entire summer season (107 days). Their model demonstrated that absolute errors in cumulated daily cold production remain below 0.3%, confirming that the lumped-parameter approach captures both short-term transient behaviour and long-term integrated performance with high fidelity (Evola et al., 2013).

The present model adopts this same lumped-parameter framework, applying mass, species, and energy balances to each unit as outlined in Chapter 3.

2.3.2 State-Space Formulation

While the models of Kohlenbach and Ziegler (2008a) and Evola et al. (2013) solve their governing equations using Newton–Raphson iterative procedures, Wen et al. (2019) demonstrated that the full system of dynamic conservation equations for a single-effect LiBr/H_2O chiller can be reduced to a compact six-order state-space representation of the form $\dot{\mathrm{x}} = f(\mathrm{x}, \mathrm{u})$, with the state vector

$$\mathbf{x} = \left[M_{\text{gen}},\ T_{\text{gen}},\ X_{\text{strong}},\ M_{\text{con}},\ T_{\text{abs}},\ X_{\text{weak}}\right]^T \qquad (2.27)$$

This reduction is achieved by applying the global LiBr mass conservation constraint and total refrigerant mass conservation to eliminate the accumulative masses in the absorber and evaporator as redundant intermediate variables (Wen et al., 2019). The result is a minimal-order model that is directly compatible with MATLAB/Simulink's ODE solver architecture and well-suited to control system design. Validation against a 6.5 kW laboratory chiller confirmed maximum steady-state relative errors below 2.15% for COP, concentration, and outlet temperatures (Wen et al., 2019).

The present model adopts the state-space formulation of Wen et al. (2019) as its baseline architecture, with modifications to the condenser pressure dynamics and solution heat exchanger representation described in Chapter 3.

2.3.3 Numerical Stability and Solver Considerations

A well-known challenge in dynamic absorption simulation is numerical stiffness: the strong nonlinear coupling between system pressure, solution concentration, and component temperatures creates differential equations whose time constants span several orders of magnitude. This forces ODE solvers to take very small time steps during transients, increasing computation time and — if not managed carefully — causing instability (Zhou *et al.*, 2023).
Zhou et al. (2023) demonstrated, using a Modelica finite-volume model of a single-effect LiBr/H_2O system, that dynamic responses exhibit strong cross-coupling between the generator and absorber: a step increase in cold-water temperature, for example, produces an initial overshoot in generator temperature followed by an inverse transient in absorber temperature before both variables settle to a new equilibrium. The same study identified initial inverse responses in evaporator vapour quality during cold-water flowrate steps — phenomena that

simple quasi-steady models cannot reproduce and that place severe demands on the numerical solver (Zhou et al., 2023).

In the present Simulink model, two specific architectural modifications are introduced to address stiffness and ensure robust solver performance during transients, particularly cold starts. First, a dynamic condenser pressure scaling mechanism is implemented, proportionally linking condenser pressure to the target liquid refrigerant mass, which self-regulates refrigerant flow and prevents the solver from encountering physically inconsistent states during initialisation. Second, the conventional quasi-steady ε-NTU approximation for the solution heat exchanger — used in both Kohlenbach and Ziegler (2008a) and Wen et al. (2019) — is replaced by a discretised 8-stage counter-flow model with finite thermal mass, which distributes the thermal transport delay across the heat exchanger length and suppresses the large enthalpy prediction errors that arise during transients when the solution temperature profile is far from its steady-state distribution. Both modifications are described in detail in Chapter 3.

3 System Description

3.1 Overview of the Simulated System

The system modelled in this thesis is a hot-water-driven, single-effect lithium bromide–water (LiBr/H_2O) absorption chiller with a nominal cooling capacity of approximately 7 kW. The target application context is marine HVAC: cruise ships and cargo vessels generate substantial engine waste heat that can serve as the thermal driving source for the generator, displacing electrically driven vapour-compression equipment and reducing onboard fuel consumption (Salmi et al., 2017). The LiBr/H_2O working pair is particularly well suited to this role because it operates at moderate generator temperatures of 75–120 °C — a range easily reached by jacket-water or exhaust-gas heat recovery — and is compatible with above-zero evaporator temperatures required for air-conditioning (Florides et al., 2003; Wen et al., 2019).

The chiller operates across two distinct pressure levels. The high-pressure side encompasses the generator and condenser, while the low-pressure side encompasses the absorber and evaporator. Three external water circuits interact with the chiller: a hot-water circuit that supplies thermal energy to the generator, a cooling-water circuit that removes heat from the absorber and condenser in series, and a chilled-water circuit that delivers cooling capacity from the evaporator to the building or HVAC load. Under nominal operating conditions, the hot-water inlet temperature is 368 K, the cooling-water inlet temperature is 305 K, and the chilled-water inlet temperature is 288 K, yielding a simulated steady-state COP of 0.718 (Wen et al., 2019).

The complete system state is governed by six dynamic state variables: the accumulated solution mass in the generator M_{gen}, the generator temperature T_{gen}, the strong solution concentration X_{strong}, the accumulated refrigerant mass in the condenser M_{con}, the absorber temperature T_{abs}, and the weak solution concentration X_{weak} (Wen et al., 2019). All thermodynamic properties of the LiBr solution — density, enthalpy, specific heat capacity, and surface vapour pressure — are evaluated using the polynomial fitting formulas of Kaita (2001), valid over the concentration range 40–65 wt.% and temperatures of 40–210 °C, which fully covers the operating envelope of a single-effect chiller.

3.2 System Layout and Component Description

The chiller consists of four main heat exchanger units — generator, condenser, evaporator, and absorber — connected by two throttling valves, one solution heat exchanger (SHX), and one solution pump, as illustrated in the system schematic of Wen et al. (2019). All four main units are modelled as shell-and-tube, counter-flow heat exchangers, each described by a lumped-parameter formulation that assigns a single uniform temperature, concentration, and pressure to the entire component interior. The following describes the role and thermodynamic function of each unit.

Generator. The generator is the thermally driven desorber of the cycle. Hot water from the waste heat source flows through the tube side, transferring heat to the LiBr/H_2O solution on the shell side. This heat drives the separation of refrigerant water vapour from the strong LiBr solution; the vapour exits toward the condenser while the now-concentrated strong solution exits toward the SHX and absorber. The generator therefore operates at high pressure and is the primary energy input point of the cycle (Florides et al., 2003).

Condenser. Refrigerant vapour leaving the generator enters the condenser, where it is cooled by the incoming cooling water and condenses to a saturated liquid. The released condensation heat is rejected to the cooling water. The condensed liquid refrigerant then passes through the refrigerant throttling valve, which reduces its pressure to the low-pressure evaporator level before it enters the evaporator (Wen et al., 2019).

Evaporator. The low-pressure liquid refrigerant entering the evaporator absorbs heat from the chilled-water circuit, evaporating at low temperature and low pressure to produce the useful cooling effect. The refrigerant vapour generated in the evaporator then flows to the absorber, driven by the vapour pressure difference between the two units (Wen et al., 2019).

Absorber. In the absorber, the dilute (weak) LiBr solution returning from the SHX absorbs the refrigerant vapour from the evaporator. This exothermic absorption process releases heat that is removed by the cooling water, which flows through the absorber before continuing to the condenser. The resulting weak solution, now enriched in water content, is pumped by the solution pump back through the SHX to the generator to complete the solution circuit (Salmi et al., 2017).

Solution Pump. The solution pump is the sole mechanical component in the chiller and the only consumer of electrical power. It lifts the weak solution from the low-pressure absorber to the high-pressure generator side. The volumetric flow rate of the pump is proportional to its rotational frequency, which is controlled by a variable-frequency drive with a nominal operating frequency of 30.8 Hz in this simulation (Wen et al., 2019).

Throttling Valves. Two adiabatic throttling valves regulate the flow between the high- and low-pressure sides of the cycle. The refrigerant expansion valve connects the condenser to the evaporator, while the solution throttle valve reduces the pressure of the strong solution returning from the generator to the absorber. Mass flow through each valve is driven by the pressure difference and gravity head, computed via an empirical orifice-flow formula (Wen et al., 2019).

Solution Heat Exchanger (SHX). The SHX is positioned in the solution circuit between the generator and the absorber, arranged as a double-pipe counter-flow heat exchanger. The hot, concentrated strong solution leaving the generator flows on one side, while the cooler, dilute weak solution being pumped toward the generator flows on the other. By recovering sensible heat internally — pre-heating the weak solution before it enters the generator and pre-cooling the strong solution before it enters the absorber — the SHX directly reduces the external heat input required at the generator, thereby increasing the system COP (Florides et al., 2003; Wen et al., 2019). The modelling approach applied to the SHX is a central subject of this thesis and is discussed in detail in Chapter 4.

3.3 Working Fluid Pair

The LiBr/H_2O working pair uses water (H_2O) as the refrigerant and lithium bromide (LiBr) as the absorbent — an inorganic salt with an exceptionally strong chemical affinity for water vapour (Florides et al., 2003). This affinity is the thermodynamic engine of the absorption cycle: it allows LiBr to absorb refrigerant vapour at low pressure in the absorber without mechanical compression, and the absorbed refrigerant is subsequently driven off by heat in the generator. Water is an excellent refrigerant owing to its very high latent heat of vaporisation, which minimises the mass flow rate required for a given cooling capacity (Florides et al., 2003). A defining practical advantage of this pair is its suitability for single-effect operation at moderate generator temperatures of 75–120 °C, which are achievable using flat-plate solar collectors, evacuated-tube collectors, or engine jacket-water heat recovery (Florides et al.,

2003; Wen et al., 2019). Because water is the refrigerant, the entire system operates under sub-atmospheric (vacuum) pressures — approximately 1,000–9,000 Pa in the present simulation — which eliminates the need for heavy-walled pressure component but requires strict hermeticity to prevent air ingress (Wen et al., 2019). The pair is also environmentally benign: neither component has ozone depletion potential or global warming potential, distinguishing it from many synthetic refrigerants used in vapour-compression systems (Florides et al., 2003).

The principal limitation of the LiBr/H_2O pair is the risk of crystallisation: if the LiBr concentration becomes too high, or the solution temperature falls too low, solid LiBr crystals precipitate and can block the solution heat exchanger, halting operation (Florides et al., 2003). This constraint bounds the maximum allowable strong solution concentration — approximately 65 wt.% in practice — and makes precise dynamic tracking of the solution concentration a critical modelling requirement. Additionally, because water freezes at 0 °C, this pair cannot produce sub-zero refrigeration, restricting its application to above-zero chilling duties such as air-conditioning (Wen et al., 2019).

All thermophysical properties of the LiBr solution in this model — vapour pressure, enthalpy, entropy, specific heat capacity, and density — are evaluated using the polynomial fitting equations developed by Kaita (2001), which are valid across concentration ranges of 40–65 wt.% and temperatures of 40–210 °C, fully encompassing the operating envelope of the simulated chiller. Thermodynamic properties of the pure-water refrigerant are retrieved from the NIST REFPROP ((National Institute of Standards and Technology - Reference fluid Properties) database (Lemmon *et al.*, 2018), which provides highly accurate saturated and superheated steam properties at the prevailing system pressures (Wen et al., 2019).

3.4 Design Operating Conditions

The nominal design conditions and on-design parameters used in this simulation are adopted directly from the validated laboratory chiller of Wen et al. (2019), which has a refrigerating capacity of approximately 6.5–7 kW. The external boundary inputs that drive the simulation are listed in Table 3.

Table 3 - Nominal external input conditions (Wen et al., 2019)

Parameter	Symbol	Value
Hot water mass flow rate	$\dot{m}_{hw}$	0.32 kg/s
Cooling water mass flow rate	$\dot{m}_{cw}$	0.65 kg/s
Chilled water mass flow rate	$\dot{m}_{clw}$	0.26 kg/s
Hot water inlet temperature	T_{hwi}	368 K (95 °C)
Cooling water inlet temperature	T_{cwi}	305 K (32 °C)
Chilled water inlet temperature	T_{clwi}	288 K (15 °C)
Solution pump frequency	f_p	30.8 Hz

The on-design physical parameters characterising the chiller hardware, also sourced from Wen et al. (2019), are provided in Table 4. These parameters define the thermal conductance of each heat exchanger and the total fluid inventories sealed within the system.

Table 4 - On-design chiller parameters (Wen et al., 2019)

Parameter	Symbol	Value
Overall mass of LiBr absorbent	M_{LiBr}	67.5 kg
Overall mass of LiBr solution (LiBr + H_2O)	M_{total}	32.5 kg
Generator heat transfer coefficient	$(UA)_{gen}$	1370 W/K
Condenser heat transfer coefficient	$(UA)_{con}$	3200 W/K
Evaporator heat transfer coefficient	$(UA)_{eva}$	2030 W/K
Absorber heat transfer coefficient	$(UA)_{abs}$	1820 W/K
Height difference (throttle valves)	Δz	0.2 m

Under these nominal conditions, the model converges to a steady-state cooling capacity of approximately 7,031 W and a thermal COP of 0.718, with a generator temperature of 356.6 K, a condenser temperature of 312.4 K, an evaporator temperature of 280.3 K, and an absorber temperature of 312.2 K (Wen et al., 2019). The strong solution concentration at steady state is 59.61 wt.% and the weak solution concentration is 56.13 wt.%, both comfortably within the crystallisation-safe operating band (Wen et al., 2019).

3.5 Key Modelling Assumptions

The dynamic model is built upon a set of physically motivated simplifying assumptions that reduce mathematical complexity while preserving the essential transient behaviour of the system. These assumptions are adopted from the baseline formulation of Wen et al. (2019) and are consistent with the lumped-parameter modelling tradition in absorption chiller literature. The following assumptions are applied throughout the model:

- **Spatial homogeneity (lumped parameters):** Temperature, pressure, and LiBr concentration are assumed spatially uniform within each main component (generator,

condenser, evaporator, and absorber). Each component is therefore described by a single representative state rather than a spatially distributed field (Wen et al., 2019).

- **Two pressure levels only:** The chiller is divided into exactly two pressure levels — a high-pressure side (generator and condenser) and a low-pressure side (absorber and evaporator). No pressure gradient exists within each side except across the throttling valves (Wen et al., 2019).
- **Exit-state fluid assumption:** Fluid leaving each component is in the same thermodynamic state as the contents of that component, i.e., the outlet enthalpy equals the internal enthalpy (Wen et al., 2019).
- **Negligible thermal mass of heat exchanger walls:** The thermal storage capacity of the shell and tube material of each main heat exchanger is neglected. Thermal inertia is attributed entirely to the fluid contents of each component (Wen et al., 2019).
- **Isenthalpic throttling:** Both throttling valves operate adiabatically; the enthalpy of the fluid is conserved across each valve (Wen et al., 2019).
- **Negligible heat losses to surroundings:** All components are treated as perfectly insulated from the ambient environment, so no heat is exchanged with the surroundings other than through the designated external water circuits (Wen et al., 2019).
- **Negligible pump work:** The mechanical power input from the solution pump is small relative to the thermal energy flows and is therefore neglected in the energy balances (Wen et al., 2019).
- **Refrigerant vapour mass is negligible in solution components:** The density of the vapour phase is orders of magnitude lower than that of the LiBr solution. Accordingly, the accumulated mass in the generator and absorber is treated as representing only the liquid solution mass (Wen et al., 2019).
- **Pure-refrigerant assumption:** The refrigerant circulating in the condenser and evaporator is treated as pure water, with no dissolved LiBr (Florides et al., 2003; Wen et al., 2019).
- **Constant total fluid inventory:** The total mass of LiBr absorbent and the total mass of solution sealed within the chiller are constants, set at manufacture; no fluid is added or removed during operation (Wen et al., 2019).

Two important **departures from the baseline Wen et al. (2019) model** are introduced in this thesis and constitute original contributions:

1. The SHX is not modelled using a quasi-steady effectiveness parameter ε_{SHX} as assumed by Wen et al. (2019), but instead as a discretised, 8-stage counter-flow heat exchanger with finite thermal mass in each plate, capturing transport delays and thermal inertia in the solution circuit.
2. Condenser pressure is not derived from a purely algebraic function of temperature and concentration but is regulated through a dynamic proportional mass-scaling mechanism, which is necessary to achieve numerical stability during transients such as cold starts.

Both modifications are described in full in Chapter 4.

4 Mathematical Modelling

4.1 Overview of the Modelling Approach

The dynamic model of the single-effect LiBr/H_2O absorption chiller developed in this thesis is built upon the lumped-parameter, state-space framework originally proposed by Wen et al. (2019). The fundamental philosophy of the approach is to treat each of the four main heat exchangers — the generator, absorber, condenser, and evaporator — as a spatially homogeneous volume whose thermodynamic state evolves in continuous time according to the laws of conservation of mass, conservation of species (LiBr), and conservation of energy. This leads naturally to a system of first-order ordinary differential equations (ODEs) that can be integrated forward in time by a numerical solver, making real-time dynamic simulation computationally feasible (Wen et al., 2019).

Two categories of dynamic behaviour are coupled within the chiller:

- **Mass accumulation:** The fluid mass stored in each component changes over time as the net difference between the mass flow rates entering and leaving that component.
- **Energy accumulation:** The internal energy stored in each component changes over time due to the combined effect of enthalpy carried in and out by fluid streams, and heat exchanged with the external water circuits.

These two forms of accumulation are the essence of the transient response. At steady state, all time derivatives vanish and the model collapses to a conventional steady-state energy balance; the dynamic model therefore generalises the steady-state case rather than replacing it (Wen et al., 2019).

The full equation set is implemented in MATLAB/Simulink and subsequently reduced to a compact state-space form, as detailed in Section 4.8. Two modifications are introduced to the baseline formulation of Wen et al. (2019): a dynamic condenser pressure scaling mechanism linked to the accumulated refrigerant mass in the condenser, which stabilises the solver during transients; and an 8-node discretised counter-flow SHX model with finite thermal mass, which replaces the quasi-steady fixed-effectiveness approximation to capture transport delays and transient heat recovery dynamics. The individual component models are presented in Sections 4.2 through 4.7.

4.2 Generator Model

The generator is the thermally driven desorber of the absorption cycle. Hot water flowing through the tube side supplies heat $\dot{Q}_{gen}$ to the LiBr/H_2O solution on the shell side, raising the solution temperature until refrigerant water boils off as superheated vapour. The departing vapour leaves behind a solution of progressively higher LiBr concentration — the strong solution — which is subsequently routed through the SHX to the absorber. Three streams therefore cross the generator boundary: the weak solution entering from the SHX, the strong solution leaving toward the absorber throttle valve, and the refrigerant vapour leaving toward the condenser (Wen et al., 2019).

4.2.1 Mass Balance

The overall mass accumulation rate in the generator shell equals the net mass flux of all streams crossing its boundary. Three streams are involved: the weak solution entering at mass flow rate $\dot{m}_{weak}$, the strong solution leaving at $\dot{m}_{strong}$, and the refrigerant vapour leaving at $\dot{m}_{v,gen}$ (Wen et al., 2019)

$$\frac{dM_{gen}}{dt} = \dot{m}_{weak} - \dot{m}_{strong} - \dot{m}_{v,gen} \qquad (4.1)$$

where M_{gen} (kg) is the total accumulated mass in the generator at time t. Since the density of the liquid LiBr solution is several orders of magnitude greater than that of the refrigerant vapour co-existing in the shell space, the mass and thermal energy contributions of the vapour phase within the generator are negligible compared to those of the solution (Wen et al., 2019). Consequently, M_{gen} is taken to represent the mass of the LiBr solution alone, which simplifies subsequent derivations without meaningful loss of accuracy (Wen et al., 2019).

4.2.2 Species Balance

A continuity equation for the LiBr absorbent alone is written for the generator control volume. Since LiBr is non-volatile and cannot leave with the refrigerant vapour, it is only transported in and out by the liquid solution streams. The general form of the LiBr species balance is (Wen et al., 2019)

$$\frac{d(M_{gen}\, X_{strong})}{dt} = \dot{m}_{weak}\, X_{weak} - \dot{m}_{strong}\, X_{strong} \qquad (4.2)$$

Expanding the left-hand side using the product rule

$$M_{gen}\frac{dX_{strong}}{dt} + X_{strong}\frac{dM_{gen}}{dt} = \dot{m}_{weak}\,X_{weak} - \dot{m}_{strong}\,X_{strong}$$

Substituting Eq. (4.1) for $\frac{dM_{gen}}{dt}$ and rearranging

$$M_{gen}\frac{dX_{strong}}{dt} + X_{strong}\left(\dot{m}_{weak} - \dot{m}_{strong} - \dot{m}_{v,gen}\right) = \dot{m}_{weak}\,X_{weak} - \dot{m}_{strong}\,X_{strong}$$

Cancelling the $\dot{m}_{strong}\,X_{strong}$ terms from both sides yields the state equation for concentration (Wen et al., 2019)

$$M_{gen}\frac{dX_{strong}}{dt} = \dot{m}_{v,gen}\,X_{strong} - \dot{m}_{weak}\left(X_{strong} - X_{weak}\right) \qquad (4.3)$$

Equation (4.3) has a clear physical interpretation: the concentration X_{strong} rises when refrigerant vapour is driven off (the first term is positive, since vapour carries no LiBr yet its departure concentrates the remaining solution) and falls when the dilute incoming weak solution reduces the average LiBr fraction (second term).

.

4.2.3 Energy Balance

The general energy balance for the generator control volume, accounting for the enthalpy carried by all incoming and outgoing streams and the external heat input, is written as (Wen et al., 2019)

$$\frac{d(M_{gen}\,h_{strong})}{dt} = \dot{m}_{weak}\,h_{weak,gen} - \dot{m}_{strong}\,h_{strong} - \dot{m}_{v,gen}\,h_{v,gen} + \dot{Q}_{gen} \qquad (4.4)$$

where h_{strong} is the specific enthalpy of the strong solution at the prevailing generator state $\left(T_{gen}, X_{strong}\right)$; $h_{weak,gen}$ is the specific enthalpy of the weak solution entering from the SHX at temperature $T_{weak,gen}$ and concentration X_{weak}; and $h_{v,gen}$ is the specific enthalpy of the superheated refrigerant vapour departing at $\left(T_{gen}, P_{gen}\right)$. The outlet-state assumption — that all streams leave the component at its internal thermodynamic state — means the strong solution outflow enthalpy equals h_{strong}, the enthalpy of the solution inside the component.

Expanding the left-hand side using the product rule

$$M_{gen}\frac{dh_{strong}}{dt} + h_{strong}\frac{dM_{gen}}{dt} = \dot{m}_{weak}\,h_{weak,gen} - \dot{m}_{strong}\,h_{strong} - \dot{m}_{v,gen}\,h_{v,gen} + \dot{Q}_{gen}$$

Substituting Eq. (4.1) for $\frac{dM_{gen}}{dt}$

$$M_{gen}\frac{dh_{strong}}{dt} + h_{strong}\left(\dot{m}_{weak} - \dot{m}_{strong} - \dot{m}_{v,gen}\right) = \dot{m}_{weak}\,h_{weak,gen} - \dot{m}_{strong}\,h_{strong} - \dot{m}_{v,gen}\,h_{v,gen} + \dot{Q}_{gen}$$

Cancelling $\dot{m}_{strong}\,h_{strong}$ from both sides and rearranging

$$M_{gen}\frac{dh_{strong}}{dt} = \dot{m}_{weak}\left(h_{weak,gen} - h_{strong}\right) - \dot{m}_{v,gen}\left(h_{v,gen} - h_{strong}\right) + \dot{Q}_{gen} \tag{4.5}$$

Since the solution enthalpy depends on both temperature and concentration, $h_{strong} = h(T_{gen}, X_{strong})$, its total time derivative is

$$\frac{dh_{strong}}{dt} = c_{p,strong}\frac{dT_{gen}}{dt} + \frac{\partial h}{\partial X}\Big|_T \frac{dX_{strong}}{dt}$$

In the lumped-parameter framework the concentration-dependent enthalpy correction term $\partial h/\,\partial X$ is small relative to the temperature-driven sensible heat term over typical operating transients, and is therefore absorbed into the $c_{p,strong}$ approximation, consistent with Wen et al. (2019). Substituting $dh_{strong}/dt \approx c_{p,strong}\,dT_{gen}/dt$ into Eq. (4.5) gives the temperature state equation

$$M_{gen}\,c_{p,strong}\frac{dT_{gen}}{dt} = \dot{m}_{weak}\left(h_{weak,gen} - h_{strong}\right) - \dot{m}_{v,gen}\left(h_{v,gen} - h_{strong}\right) + \dot{Q}_{gen} \tag{4.6}$$

Equations (4.1), (4.3), and (4.6) together constitute the three differential equations of the generator sub-model, with M_{gen}, X_{strong}, and T_{gen} as the state variables (Wen et al., 2019).

4.2.4 Heat Transfer Rate

The heat input $\dot{Q}_{gen}$ and the hot water outlet temperature $T_{hw,o}$ are determined by simultaneously solving the external energy balance and the Log Mean Temperature Difference

(LMTD) heat exchanger equation for the generator, as formalised in Eq. (4.8) (Wen *et al.*, 2019).

The external energy balance on the hot water stream gives

$$\dot{Q}_{gen} = \dot{m}_{hw}\, c_{p,w}\left(T_{hw,i} - T_{hw,o}\right) \qquad (4.7)$$

Because the internal solution is at the uniform temperature T_{gen} under the lumped-parameter assumption, the temperature difference between the hot water and the solution varies continuously from $\left(T_{hw,i} - T_{gen}\right)$ at the inlet to $\left(T_{hw,o} - T_{gen}\right)$ at the outlet. The LMTD formulation for this counter-flow arrangement gives (Wen et al., 2019)

$$\dot{Q}_{gen} = UA_{gen} \cdot \frac{\left(T_{hw,i} - T_{gen}\right) - \left(T_{hw,o} - T_{gen}\right)}{\ln\left(\dfrac{T_{hw,i} - T_{gen}}{T_{hw,o} - T_{gen}}\right)} \qquad (4.8)$$

Equating Eqs. (4.7) and (4.8) and solving for $T_{hw,o}$ by letting $\theta = (T_{hw,o} - T_{gen})/(T_{hw,i} - T_{gen})$, one obtains $\ln\,\theta = -UA_{gen}/(\dot{m}_{hw} c_{p,w})$, from which $\theta = e^{-UA_{gen}/(\dot{m}_{hw} c_{p,w})}$. Back-substituting yields the closed-form expressions (Wen et al., 2019)

$$\dot{Q}_{gen} = \dot{m}_{hw}\, c_{p,w}\left(1 - e^{-UA_{gen}/(\dot{m}_{hw}\, c_{p,w})}\right)\left(T_{hw,i} - T_{gen}\right) \qquad (4.9)$$

$$T_{hw,o} = T_{hw,i} - \left(1 - e^{-UA_{gen}/(\dot{m}_{hw}\, c_{p,w})}\right)\left(T_{hw,i} - T_{gen}\right) \qquad (4.10)$$

In the Simulink implementation, $T_{hw,o}$ is computed by a further simplification. Since $\dot{Q}_{gen}$ has already been evaluated from Eq. (4.9), it is more direct to rearrange the external energy balance (Eq. 4.7) explicitly for the outlet temperature, avoiding a redundant exponential evaluation

$$T_{hw,o} = T_{hw,i} - \frac{\dot{Q}_{gen}}{\dot{m}_{hw}\, c_{p,w}} \qquad (4.11)$$

This is algebraically equivalent to Eq. (4.10) but is the form implemented in the model, with $\dot{Q}_{gen}$ taken directly from Eq. (4.9).

4.2.5 Thermophysical Properties of the Generator

All solution properties required by the generator sub-model are evaluated at the current state $\left(T_{gen},\, X_{strong}\right)$ using the correlations of Kaita (2001), which are valid for 40–65 wt.% and 40–210 °C.

Specific heat capacity: Using Rockenfeller's empirical equation as recommended by Kaita (2001)

$$c_{p,strong} = \left(A_0 + A_1\, X_{strong}\right) + \left(B_0 + B_1\, X_{strong}\right) T_{gen,^\circ} \qquad (4.12)$$

where $T_{gen,^\circ}$ is T_{gen} expressed in °C, and the coefficients are $A_0 = 3.462023$, $A_1 = -2.679895 \times 10^{-2}$, $B_0 = 1.3499 \times 10^{-3}$, $B_1 = -6.55 \times 10^{-6}$ (kJ kg⁻¹ °C⁻¹) (Kaita, 2001).

Specific enthalpy of the strong solution: Integrating c_p over temperature from the 25 °C reference state and accounting for the concentration-dependent baseline, Kaita (2001) derives

$$h_{strong} = \left(A_0 + A_1\, X_{strong}\right) T_{gen,^\circ} + \frac{1}{2}\left(B_0 + B_1\, X_{strong}\right) T_{gen,^\circ}^2 + D_0 + D_1\, X_{strong} + D_2\, X_{strong}^2 + D_3\, X_{strong}^3 \qquad (4.13)$$

with $D_0 = 162.81$, $D_1 = -6.0418$, $D_2 = 4.5348 \times 10^{-3}$, $D_3 = 1.2053 \times 10^{-3}$ (kJ kg⁻¹); the coefficients A_i and B_i are identical to those in Eq. (4.11) (Kaita, 2001).

Specific enthalpy of the incoming weak solution: The weak solution arrives from the SHX at temperature $T_{weak,gen}$ and concentration X_{weak}. Its enthalpy is evaluated using the same correlation (Eq. 4.12) at the appropriate state

$$h_{weak,gen} = H\left(T_{weak,gen,^\circ},\ X_{weak}\right) \qquad (4.14)$$

Generator (high-side) pressure: The generator pressure P_{gen} equals the equilibrium surface vapour pressure of the strong solution. Kaita (2001) computes this via a dew-point intermediate T_D (°C)

$$T_D = \sum_{i=0}^{2} \sum_{j=0}^{3} A_{ij} (x - 40)^j T^i \qquad (4.15)$$

where the matrix of coefficients A_{ij} is given in Kaita (2001). The vapour pressure is then recovered from the dew-point temperature using (Kaita, 2001)

$$P_{gen} = k_0 + \frac{k_1}{T_D + 273.15} + \frac{k_2}{(T_D + 273.15)^2} \qquad (4.16)$$

with $k_0 = 7.05$, $k_1 = -1603.54$, $k_2 = -104095.5$ (Pa). This pressure simultaneously defines the high-pressure side of the system, so P_{gen} is also passed to the condenser sub-model.

Specific enthalpy of the superheated refrigerant vapour: The refrigerant vapour leaves the generator superheated at temperature T_{gen} and pressure P_{gen}. Its specific enthalpy $h_{v,gen}$ is retrieved from the NIST REFPROP database as a function of (T_{gen}, P_{gen}) (Wen et al., 2019)

4.2.6 Refrigerant Vapour Mass Flow Rate

The refrigerant vapour mass flow rate $\dot{m}_{v,gen}$ is a key coupling variable that appears in all three generator state equations. Because the latent heat of vaporisation of water is much larger than the sensible heat contribution, the energy balance in the condenser can be reduced to a pure phase-change process (Wen et al., 2019). The mass flow rate of vapour condensed in the condenser equals the mass flow rate generated in the generator under the two-pressure, closed-loop assumption. Applying this simplification to the condenser energy balance gives (Wen et al., 2019)

$$\dot{m}_{v,gen} = \frac{\dot{Q}_{con}}{h_{v,gen} - h_{lc}} \qquad (4.17)$$

where $\dot{Q}_{con}$ is the heat rejected in the condenser (derived in Section 4.3) and h_{lc} is the specific enthalpy of saturated liquid refrigerant at the condenser pressure P_{con}, retrieved from NIST REFPROP (Lemmon *et al.*, 2018). Equation (4.17) closes the generator sub-model by supplying the vapour outflow term required in Eqs. (4.1) and (4.3), and the enthalpy departure term in Eq. (4.6)

4.3 Absorber Model

The absorber performs the thermodynamic inverse of the generator. The strong solution arriving from the generator throttle valve absorbs the low-pressure refrigerant vapour evaporated in the evaporator, releasing the heat of absorption to the cooling water circuit. This absorption process regenerates the weak solution, which is then pumped back to the generator via the SHX. Three streams cross the absorber boundary: the strong solution entering from the throttle valve, the refrigerant vapour entering from the evaporator, and the weak solution leaving toward the solution pump (Wen et al., 2019).

4.3.1 Mass Balance

The overall mass accumulation rate in the absorber equals the net mass flux of all streams crossing its boundary (Wen et al., 2019)

$$\frac{dM_{abs}}{dt} = \dot{m}_{strong} - \dot{m}_{weak} + \dot{m}_{v,abs} \qquad (4.18)$$

where M_{abs} (kg) is the total accumulated solution mass in the absorber, $\dot{m}_{strong}$ is the strong solution entering from the throttle valve, $\dot{m}_{weak}$ is the weak solution leaving toward the pump, and $\dot{m}_{v,abs}$ is the refrigerant vapour absorbed from the evaporator. As in the generator, the vapour mass within the absorber shell is negligible compared to the liquid solution mass, so M_{abs} represents the LiBr solution mass alone (Wen et al., 2019).

However, as discussed later in Section 4.8, M_{abs} is not an independent state variable. It is instead eliminated via the global LiBr conservation constraint and computed algebraically at each time step as (Wen et al., 2019)

$$M_{abs} = \frac{M_{LiBr} - M_{gen}\, X_{strong}}{X_{weak}} \qquad (4.19)$$

4.3.2 Species Balance

The LiBr species balance for the absorber control volume is written in the same manner as for the generator. Since LiBr is non-volatile, it is transported only by the liquid solution streams. The general form is (Wen et al., 2019)

$$\frac{d(M_{abs}\, X_{weak})}{dt} = \dot{m}_{strong}\, X_{strong} - \dot{m}_{weak}\, X_{weak} \qquad (4.20)$$

Expanding the left-hand side using the product rule and substituting Eq. (4.18) for dM_{abs}/dt

$$M_{abs}\frac{dX_{weak}}{dt} + X_{weak}\left(\dot{m}_{strong} - \dot{m}_{weak} + \dot{m}_{v,abs}\right) = \dot{m}_{strong}\, X_{strong} - \dot{m}_{weak}\, X_{weak}$$

Cancelling the $\dot{m}_{weak}\, X_{weak}$ terms and rearranging yields the state equation for the weak solution concentration (Wen et al., 2019)

$$M_{abs}\frac{dX_{weak}}{dt} = \dot{m}_{strong}\left(X_{strong} - X_{weak}\right) - \dot{m}_{v,abs}\, X_{weak} \qquad (4.21)$$

The physical interpretation mirrors that of the generator: X_{weak} falls as the strong solution dilutes the absorber inventory (first term) and rises when vapour absorption increases the water content, reducing the LiBr fraction (second term, noting X_{weak} is positive so absorbing pure water vapour reduces concentration).

4.3.3 Energy Balance

The general energy balance for the absorber control volume is (Wen et al., 2019)

$$\frac{d(M_{abs}\, h_{weak})}{dt} = \dot{m}_{strong}\, h_{strong,abs} - \dot{m}_{weak}\, h_{weak} + \dot{m}_{v,abs}\, h_{v,abs} - \dot{Q}_{abs} \tag{4.22}$$

where h_{weak} is the specific enthalpy of the weak solution at the absorber state (T_{abs}, X_{weak}); $h_{strong,abs}$ is the specific enthalpy of the strong solution entering from the throttle valve; $h_{v,abs}$ is the specific enthalpy of the refrigerant vapour entering from the evaporator; and $\dot{Q}_{abs}$ is the heat rejected to the cooling water, which carries a negative sign consistent with heat leaving the system. Expanding the left-hand side and substituting Eq. (4.18) for dM_{abs}/dt

$$M_{abs}\frac{dh_{weak}}{dt} + h_{weak}\left(\dot{m}_{strong} - \dot{m}_{weak} + \dot{m}_{v,abs}\right) = \dot{m}_{strong}\, h_{strong,abs} - \dot{m}_{weak}\, h_{weak} + \dot{m}_{v,abs}\, h_{v,abs} - \dot{Q}_{abs}$$

Cancelling $\dot{m}_{weak}\, h_{weak}$ from both sides and rearranging

$$M_{abs}\frac{dh_{weak}}{dt} = \dot{m}_{strong}\left(h_{strong,abs} - h_{weak}\right) + \dot{m}_{v,abs}\left(h_{v,abs} - h_{weak}\right) - \dot{Q}_{abs} \tag{4.23}$$

Applying the same approximation as in Section 4.2.3 — that $dh_{weak}/dt \approx c_{p,weak}\, dT_{abs}/dt$ — gives the temperature state equation for the absorber (Wen et al., 2019)

$$M_{abs}\, c_{p,weak}\frac{dT_{abs}}{dt} = \dot{m}_{strong}\left(h_{strong,abs} - h_{weak}\right)\dot{m}_{v,abs}\left(h_{v,abs} - h_{weak}\right) - \dot{Q}_{abs} \tag{4.24}$$

Equations (4.18), (4.21), and (4.24) constitute the three differential equations of the absorber sub-model. As noted above, since M_{abs} is not a free state variable but is recovered from Eq. (4.19), the only true absorber state variable integrated forward in time is X_{weak} and T_{abs} (Wen et al., 2019).

4.3.4 Heat Transfer Rate and Cooling Water Outlet Temperature

The derivation of $\dot{Q}_{abs}$ and the cooling water outlet temperature $T_{clw,o,abs}$ follows the same LMTD procedure as established for the generator in Section 4.2.4. The internal solution is at the uniform temperature T_{abs}, and the cooling water enters at $T_{clw,i}$ and exits at $T_{clw,o,abs}$. The closed-form expressions are (Wen et al., 2019)

$$\dot{Q}_{abs} = \dot{m}_{clw}\, c_{p,w}\left(1-e^{-UA_{abs}/(\dot{m}_{clw}\, c_{p,w})}\right)\left(T_{abs}-T_{clw,i}\right) \qquad (4.25)$$

One important distinction from the generator is the **series cooling water arrangement**: the cooling water flows first through the absorber and then through the condenser (Wen et al., 2019). Consequently, the cooling water inlet temperature to the condenser is not the external supply temperature but the absorber cooling water outlet temperature

$$T_{clw,o,abs} = T_{clw,i} + \frac{\dot{Q}_{abs}}{\dot{m}_{clw}\, c_{p,w}} \qquad (4.26)$$

This outlet temperature $T_{clw,o,abs}$ is passed directly as the inlet condition $T_{clw,i,con}$ to the condenser sub-model (Section 4.4), coupling the two heat rejection components in series.

4.3.5 Thermophysical Properties of the Absorber

All solution properties in the absorber are evaluated at the current state (T_{abs}, X_{weak}) using the Kaita (2001) correlations, following the same procedure as Section 4.2.5. The property equations are identical in form; only the arguments change.

Specific heat capacity of the weak solution

$$c_{p,weak} = (A_0+A_1\, X_{weak}) + (B_0+B_1\, X_{weak})T_{abs,^\circ} \qquad (4.27)$$

with coefficients as given in Eq. (4.12) (Kaita, 2001).

Specific enthalpy of the weak solution at the absorber state

$$h_{weak} = H\left(T_{abs,^\circ},\ X_{weak}\right) \qquad (4.28)$$

evaluated using Eq. (4.13) at $\left(T_{abs,^\circ},\ X_{weak}\right)$ (Kaita, 2001).

Specific enthalpy of the strong solution entering the absorber. The strong solution arrives from the generator throttle valve. The throttling process is isenthalpic, so the enthalpy at the absorber inlet equals the enthalpy of the strong solution at the generator exit state (T_{gen}, X_{strong})

$$h_{strong,abs} = h_{strong} = H(T_{gen,\circ}, X_{strong}) \qquad (4.29)$$

Absorber (low-side) pressure. The absorber pressure P_{abs} equals the equilibrium surface vapour pressure of the weak solution at its current temperature and concentration, computed using Eqs. (4.15) and (4.16) evaluated at (T_{abs}, X_{weak}) (Kaita, 2001). This pressure defines the low-pressure side of the system and is shared with the evaporator: $P_{abs} = P_{eva}$

4.3.6 Refrigerant Vapour Mass Flow Rate at the Absorber

The refrigerant vapour mass flow rate entering the absorber, $\dot{m}_{v,abs}$, equals the rate at which refrigerant evaporates in the evaporator under steady closed-loop operation. By analogy with Eq. (4.16), it is derived from the evaporator energy balance by treating the evaporation process as a pure phase change (Wen et al., 2019)

$$\dot{m}_{v,abs} = \frac{\dot{Q}_{eva}}{h_{v,abs} - h_{lc}} \qquad (4.30)$$

where $\dot{Q}_{eva}$ is the heat absorbed in the evaporator (derived in Section 4.4), $h_{v,abs}$ is the specific enthalpy of the saturated refrigerant vapour at the low-side pressure P_{abs}, and h_{lc} is the specific enthalpy of the saturated liquid refrigerant entering the evaporator from the condenser throttle valve — both retrieved from NIST REFPROP at P_{abs} (Wen et al., 2019).

4.4 Condenser Model

4.4.1 Mass Balance

The mass accumulation rate of liquid refrigerant in the condenser equals the incoming vapour mass flow rate minus the outgoing liquid mass flow rate (Wen et al., 2019)

$$\frac{dM_{con}}{dt} = \dot{m}_{v,gen} - \dot{m}_{lc} \qquad (4.31)$$

where M_{con} (kg) is the accumulated mass of liquid refrigerant in the condenser and $\dot{m}_{lc}$ is the mass flow rate of liquid refrigerant leaving toward the evaporator throttle valve. Unlike the generator and absorber, the condenser contains only cooling water and condensed water — no LiBr — so no species balance equation is required. M_{con} is therefore the sole mass state variable of the condenser and is one of the six system state variables integrated forward in time (Wen et al., 2019).

4.4.2 Energy Balance

The general energy balance for the condenser control volume accounts for the enthalpy carried in by the incoming vapour, the enthalpy carried out by the outgoing liquid, and the heat rejected to the cooling water (Wen et al., 2019)

$$\frac{d(M_{con}\, h_{lc})}{dt} = \dot{m}_{v,gen}\, h_{v,gen} - \dot{m}_{lc}\, h_{lc} - \dot{Q}_{con} \qquad (4.32)$$

where h_{lc} is the specific enthalpy of the saturated liquid refrigerant at condenser temperature T_{con}, and $h_{v,gen}$ is the specific enthalpy of the refrigerant vapour arriving from the generator at T_{gen}. Expanding the left-hand side using the product rule and substituting Eq. (4.31) for dM_{con}/dt

$$M_{con}\frac{dh_{lc}}{dt} + h_{lc}\left(\dot{m}_{v,gen} - \dot{m}_{lc}\right) = \dot{m}_{v,gen}\, h_{v,gen} - \dot{m}_{lc}\, h_{lc} - \dot{Q}_{con}$$

Cancelling $\dot{m}_{lc}\, h_{lc}$ from both sides

$$M_{con}\frac{dh_{lc}}{dt} = \dot{m}_{v,gen}\left(h_{v,gen} - h_{lc}\right) - \dot{Q}_{con} \qquad (4.33)$$

Since the condenser operates as a phase-change heat exchanger, the latent heat of condensation greatly dominates over sensible heat accumulation. The term $M_{con}\, dh_{lc}/dt$ is therefore negligible relative to the latent heat terms and is dropped (Wen et al., 2019). Equation (4.33) then reduces to the quasi-steady energy balance

$$\dot{m}_{v,gen} = \frac{\dot{Q}_{con}}{h_{v,gen} - h_{lc}} \qquad (4.34)$$

In the Simulink implementation, the sensible accumulation term $M_{con}\, dh_{lc}/dt$ is not implemented as an explicit differential equation. Instead, $\dot{m}_{v,gen}$ is evaluated algebraically from Eq. (4.33) at each time step, with $\dot{Q}_{con}$ and h_{lc} supplied by the heat transfer and property sub-blocks respectively. The sole integrated state variable of the condenser sub-model remains M_{con}, governed by Eq. (4.31).

4.4.3 Heat Transfer Rate and Cooling Water Outlet Temperature

The derivation of $\dot{Q}_{con}$ and the cooling water outlet temperature $T_{clw,o,con}$ follows the same LMTD procedure established in Section 4.2.4. The internal refrigerant is at the uniform condensing temperature T_{con}, and the cooling water enters the condenser at $T_{clw,i,con}$ — which, due to the series cooling water arrangement described in Section 4.3.4, equals the absorber cooling water outlet temperature: $T_{clw,i,con} = T_{clw,o,abs}$. The closed-form heat transfer rate is (Wen et al., 2019)

$$\dot{Q}_{con} = \dot{m}_{clw}\, c_{p,w}\left(1-e^{-UA_{con}/(\dot{m}_{clw}\, c_{p,w})}\right)\left(T_{con}-T_{clw,i,con}\right) \qquad (4.35)$$

Since $\dot{Q}_{con}$ has already been evaluated from Eq. (4.34), the cooling water outlet temperature is recovered directly by rearranging the external energy balance, following the same simplification as Eq. (4.11)

$$T_{clw,o,con} = T_{clw,i,con} + \frac{\dot{Q}_{con}}{\dot{m}_{clw}\, c_{p,w}} \qquad (4.36)$$

4.4.4 Thermophysical Properties and Condenser Pressure

Condenser pressure. The condenser operates on the high-pressure side of the system. In the baseline formulation, its pressure equals the equilibrium surface vapour pressure of the strong solution in the generator, evaluated at $\left(T_{gen}, X_{strong}\right)$ using Eqs. (4.15) and (4.16)

$$P_{con} = P_{gen} = P_{sat,LiBr}\left(T_{gen}, X_{strong}\right) \qquad (4.37)$$

As introduced in Section 4.1, the present model modifies this with a dynamic mass-scaling mechanism during transients

$$P_{con} = P_{gen} \cdot \frac{M_{con}}{M_{con,target}} \qquad (4.38)$$

When $M_{con} \to M_{con,target}$, Eq. (4.38) recovers Eq. (4.37) identically at steady state, so no accuracy is lost at design-point operation.

Condenser temperature. Under the lumped-parameter assumption, the condensing temperature $T_{con} = T_{sat}(P_{con})$ is the saturation temperature of the refrigerant at the prevailing condenser pressure P_{con}, retrieved from NIST REFPROP (Wen et al., 2019).

It is computed using the Antoine equation (Florides et al., 2003). The pressure is first converted from Pascals to mmHg

$$P_{con,mmHg} = \frac{P_{con}}{133.322} \qquad (4.39)$$

The saturation temperature is

$$T_{con,^\circ C} = \frac{B}{A - \log_{10}(P_{con,mmHg})} - C \qquad (4.40)$$

with Antoine constants $A = 8.07131$, $B = 1730.63$, $C = 233.426$, valid over the range 1°C–100°C (Florides et al., 2003). Converting to Kelvin

$$T_{con} = T_{con,^\circ C} + 273.15 \qquad (4.41)$$

Saturated liquid enthalpy h_{lc}. The specific enthalpy of the saturated liquid refrigerant leaving the condenser is evaluated at T_{con} using the Florides et al. (2003) polynomial correlations for pure water.

The saturated vapour enthalpy

$$h_{g,con} = -0.00125397\, T_{con,^\circ C}^2 + 1.88060937\, T_{con,^\circ C} + 2500.559 \text{(kJ/kg)} \qquad (4.42)$$

and latent heat of condensation

$$h_{fg,con} = -0.00132635\, T_{con,^\circ C}^2 - 2.29983657\, T_{con,^\circ C} + 2500.43063 \text{(kJ/kg)} \qquad (4.43)$$

The saturated liquid enthalpy

$$h_{lc} = \left(h_{g,con} - h_{fg,con}\right) \times 1000 \text{(J/kg)} \qquad (4.44)$$

Refrigerant vapour enthalpy $h_{v,gen}$. The specific enthalpy of the refrigerant vapour arriving from the generator is evaluated at T_{gen} using the same saturated vapour polynomial of Eq. (4.42), consistent with treating the generator exit vapour as saturated at the high-side temperature (Florides et al., 2003)

$$h_{v,gen} = \left(-0.00125397\, T_{gen,^\circ C}^2 + 1.88060937\, T_{gen,^\circ C} + 2500.559\right) \times 1000 \text{(J/kg)} \qquad (4.45)$$

4.4.5 Liquid Refrigerant Mass Flow Rate

The liquid refrigerant mass flow rate $\dot{m}_{lc}$ leaving the condenser is driven by the pressure differential ($P_{con} - P_{eva}$) and the hydrostatic head of the accumulated liquid refrigerant in the condenser. Its full derivation, together with the strong solution throttle valve formulation, is presented in Section 4.7.

4.5 Evaporator Model

The evaporator absorbs heat from the chilled water circuit by evaporating the low-pressure liquid refrigerant arriving from the condenser throttle valve. This endothermic phase change produces the useful cooling effect of the chiller. The evaporated refrigerant vapour then flows to the absorber, completing the refrigerant loop. Two streams cross the evaporator boundary: liquid refrigerant entering from the condenser throttle valve and refrigerant vapour leaving toward the absorber (Wen et al., 2019).

4.5.1 Mass Balance

The mass accumulation rate of liquid refrigerant in the evaporator equals the incoming liquid flow minus the outgoing vapour flow (Wen et al., 2019)

$$\frac{dM_{eva}}{dt} = \dot{m}_{lc} - \dot{m}_{v,abs} \qquad (4.46)$$

where M_{eva} (kg) is the accumulated mass of liquid refrigerant in the evaporator, $\dot{m}_{lc}$ is the liquid refrigerant entering from the condenser throttle valve, and $\dot{m}_{v,abs}$ is the refrigerant vapour leaving toward the absorber. Like the condenser, the evaporator contains only pure refrigerant water, so no species balance is required. M_{eva} is therefore the sole mass state variable of the evaporator and is one of the six system state variables integrated forward in time

(Wen et al., 2019). The outgoing liquid mass flow rate $\dot{m}_{lc}$ is governed by the refrigerant throttle valve, derived in Section 4.7.

4.5.2 Energy Balance

The general energy balance for the evaporator control volume accounts for the enthalpy carried in by the incoming liquid, the enthalpy carried out by the outgoing vapour, and the heat absorbed from the chilled water (Wen et al., 2019)

$$\frac{d(M_{eva}\, h_{leva})}{dt} = \dot{m}_{lc}\, h_{lc} - \dot{m}_{v,abs}\, h_{v,abs} + \dot{Q}_{eva} \qquad (4.47)$$

where h_{leva} is the specific enthalpy of the saturated liquid refrigerant at evaporator temperature T_{eva}, h_{lc} is the specific enthalpy of the liquid refrigerant entering from the condenser throttle valve evaluated at T_{con}, and $h_{v,abs}$ is the specific enthalpy of the saturated vapour leaving toward the absorber evaluated at T_{eva}. Note that $\dot{Q}_{eva}$ carries a positive sign since heat flows into the evaporator from the chilled water. Expanding the left-hand side using the product rule and substituting Eq. (4.46) for dM_{eva}/dt

$$M_{eva}\frac{dh_{leva}}{dt} + h_{leva}\left(\dot{m}_{lc} - \dot{m}_{v,abs}\right) = \dot{m}_{lc}\, h_{lc} - \dot{m}_{v,abs}\, h_{v,abs} + \dot{Q}_{eva}$$

Rearranging:

$$M_{eva}\frac{dh_{leva}}{dt} = \dot{m}_{lc}(h_{lc} - h_{leva}) - \dot{m}_{v,abs}\left(h_{v,abs} - h_{leva}\right) + \dot{Q}_{eva} \qquad (4.48)$$

As in the condenser, the evaporator operates predominantly as a phase-change heat exchanger. The latent heat of vaporisation dominates over sensible enthalpy accumulation, so the term $M_{eva}\, dh_{leva}/dt$ is negligible and is dropped (Wen et al., 2019). Equation (4.48) then reduces to the quasi-steady energy balance used to evaluate the vapour mass flow rate:

$$\dot{m}_{v,abs} = \frac{\dot{m}_{lc}(h_{lc} - h_{leva}) + \dot{Q}_{eva}}{h_{v,abs} - h_{leva}} \qquad (4.49)$$

In the Simulink implementation, $\dot{m}_{v,abs}$ is evaluated algebraically from Eq. (4.48) at each time step, with $\dot{Q}_{eva}$, h_{lc}, h_{leva}, and $h_{v,abs}$ supplied by the heat transfer and property sub-blocks

respectively. The sole integrated state variable of the evaporator sub-model remains M_{eva}, governed by Eq. (4.46).

4.5.3 Heat Transfer Rate and Chilled Water Outlet Temperature

The derivation of $\dot{Q}_{eva}$ and the chilled water outlet temperature $T_{chw,o}$ follows the same LMTD procedure established in Section 4.2.4. The internal refrigerant is at the uniform evaporating temperature T_{eva}, and the chilled water enters at $T_{chw,i}$ and exits at $T_{chw,o}$. Since heat flows from the chilled water into the refrigerant, the driving temperature difference is $(T_{chw,i} - T_{eva})$, and the closed-form heat transfer rate is (Wen et al., 2019)

$$\dot{Q}_{eva} = \dot{m}_{chw}\, c_{p,w}\left(1 - e^{-UA_{eva}/(\dot{m}_{chw}\, c_{p,w})}\right)\left(T_{chw,i} - T_{eva}\right) \qquad (4.50)$$

Since $\dot{Q}_{eva}$ has already been evaluated from Eq. (4.49), the chilled water outlet temperature is recovered directly by rearranging the external energy balance, following the same simplification as Eq. (4.11)

$$T_{chw,o} = T_{chw,i} - \frac{\dot{Q}_{eva}}{\dot{m}_{chw}\, c_{p,w}} \qquad (4.51)$$

$T_{chw,o}$ is the primary performance output of the chiller and is used directly for validation against design-point data.

4.5.4 Thermophysical Properties and Evaporator Temperature

Evaporator pressure. The evaporator operates on the low-pressure side of the system. Its pressure equals the equilibrium surface vapour pressure of the weak solution in the absorber, evaluated at the current absorber state $(T_{abs},\ X_{weak})$ using Eqs. (4.15) and (4.16)

$$P_{eva} = P_{abs} = P_{sat,LiBr}(T_{abs},\ X_{weak}) \qquad (4.52)$$

This coupling enforces the physical requirement that the absorber and evaporator share the same low-side pressure level.

Evaporator temperature. T_{eva} is the saturation temperature of pure refrigerant water at the prevailing P_{eva}. It is computed using the same Antoine equation procedure as established for the condenser in Eqs. (4.39)–(4.41), with P_{eva} substituted in place of P_{con} (Florides et al., 2003):

$$P_{eva,mmHg} = \frac{P_{eva}}{133.322} \qquad (4.53)$$

$$T_{eva,^\circ C} = \frac{B}{A - \log_{10}(P_{eva,mmHg})} - C \qquad (4.54)$$

$$T_{eva} = T_{eva,^\circ C} + 273.15 \qquad (4.55)$$

with the same Antoine constants $A = 8.07131$, $B = 1730.63$, $C = 233.426$ (Florides et al., 2003).

Saturated vapour enthalpy $h_{v,abs}$. The specific enthalpy of the refrigerant vapour leaving the evaporator is evaluated at T_{eva} using the Florides et al. (2003) saturated vapour polynomial, following the same form as Eq. (4.42)

$$h_{v,abs} = \left(-0.00125397\, T_{eva,^\circ C}^2 + 1.88060937\, T_{eva,^\circ C} + 2500.559\right) \times 1000 \text{(J/kg)} \qquad (4.56)$$

Saturated liquid enthalpy h_{leva}. The specific enthalpy of the saturated liquid refrigerant at evaporator conditions is evaluated at T_{eva} using Eqs. (4.42)–(4.44) with $T_{eva,^\circ C}$ substituted in place of $T_{con,^\circ C}$ (Florides et al., 2003)

$$h_{leva} = \left(h_{g,eva} - h_{fg,eva}\right) \times 1000 \text{(J/kg)} \qquad (4.57)$$

Liquid refrigerant enthalpy h_{lc}. The liquid refrigerant entering the evaporator from the condenser throttle valve undergoes isenthalpic throttling. Its specific enthalpy therefore equals the saturated liquid enthalpy at the condenser exit state, evaluated at T_{con} from Eq. (4.44), and is passed directly into the evaporator energy balance without further modification.

4.6 Solution Heat Exchanger (SHX) Model

The solution heat exchanger is a recuperative heat exchanger that transfers heat from the hot strong solution leaving the generator to the cold weak solution leaving the solution pump, before the latter enters the generator. This internal heat recovery reduces the thermal load on the generator and improves the overall COP of the cycle. To accurately capture thermal transport delays and the evolution of the temperature profile during transients, the SHX is modelled using a dynamic spatial discretisation approach rather than a conventional quasi-steady effectiveness approximation.

4.6.1 Model Architecture: Discretised Counter-Flow Arrangement

The SHX is divided into $N = 8$ equal stages using a lumped-parameter approximation, applied to the SHX only. The strong solution (hot side) flows from stage 8 to stage 1, while the weak solution (cold side) flows from stage 1 to stage 8, enforcing the counter-flow configuration. Each stage i contains two lumped nodes — one for the hot-side strong solution at temperature $T_{h,i}$ and one for the cold-side weak solution at temperature $T_{c,i}$ — each carrying an equal share of the total fluid mass m. No separate wall node is used; instead, the inter-stream heat exchange is modelled directly between the two fluid nodes at each stage. The full SHX sub-model therefore consists of $2 \times 8 = 16$ coupled first-order ordinary differential equations, making it the most detailed sub-model in the system.

4.6.2 Energy Balance for Each Stage

For each stage i, two energy balance equations govern the evolution of the hot-side and cold-side temperatures.

Hot-side node (strong solution, flowing from stage $i + 1$ toward stage i)

$$\frac{dT_{h,i}}{dt} = \frac{\dot{m}_{strong}}{m}\left(T_{h,in,i} - T_{h,i}\right) - \frac{\dot{Q}_i}{m\, c_{p,st}} \qquad (4.58)$$

Cold-side node (weak solution, flowing from stage $i - 1$ toward stage i)

$$\frac{dT_{c,i}}{dt} = \frac{\dot{m}_{weak}}{m}\left(T_{c,in,i} - T_{c,i}\right) + \frac{\dot{Q}_i}{m\, c_{p,wk}} \qquad (4.59)$$

where $m = 2$ kg is the lumped fluid mass assigned to each stage, shared equally between the two streams; $c_{p,st}$ and $c_{p,wk}$ are the specific heat capacities of the strong and weak solutions respectively, evaluated using the Kaita (2001) correlations; and $T_{h,in,i}$ and $T_{c,in,i}$ are the inlet temperatures to stage i from the upstream stage on each respective side.

The inter-stage heat transfer rate $\dot{Q}_i$ at each stage is (Wen et al., 2019)

$$\dot{Q}_i = \frac{K}{\dot{m}\, c_p}\left(T_{h,i} - T_{c,i}\right) \qquad (4.60)$$

with heat transfer constant $K = 50$ W/K. This formulation captures the finite thermal resistance between the two streams at each stage and, combined with the finite fluid mass m,

introduces the thermal inertia responsible for the transient transport delay behaviour that a quasi-steady model cannot reproduce.

4.7 Throttling Devices and Solution Pump

The chiller contains two throttling devices and one solution pump. The refrigerant throttle valve expands the saturated liquid refrigerant from the condenser to the evaporator, and the strong solution throttle valve expands the strong solution from the generator to the absorber. Both are modelled as quasi-steady adiabatic devices driven by gravity and the pressure difference between the connected components. The solution pump raises the weak solution from absorber pressure to generator pressure. None of these devices contain a significant fluid inventory, and therefore they contribute no differential state equations to the system (Wen et al., 2019).

4.7.1 Throttle Valve Model

Both throttling devices share the same empirical formulation. The liquid mass flow rate through a throttle valve is (Wen et al., 2019)

$$\dot{m}_l = A_{vl}\, C_{vl}\sqrt{\rho_l(\Delta P + \rho_l\, g\, (Z + z))} \qquad (4.61)$$

where A_{vl} and C_{vl} are the minimum cross-sectional area and flow coefficient of the valve; ρ_l is the density of the liquid flowing through the valve; ΔP is the pressure difference between the connected components; g is gravitational acceleration; z is the fixed height difference between the upper component outlet and the lower component inlet; and Z is the level height of the liquid in the upper component, which is proportional to the accumulated liquid mass (Wen et al., 2019)

$$Z = \frac{M}{\rho_l\, A} \qquad (4.62)$$

where M is the accumulated liquid mass in the upper component and A is its base cross-sectional area.

Equation (4.61) is applied to each throttle valve with the appropriate substitutions summarised below:

Dr	**Refrigerant Valve**	**Strong Solution Valve**
$\boldsymbol{\Delta P}$	$P_{con} - P_{eva}$	$P_{gen} - P_{abs}$
$\boldsymbol{\rho_l}$	$\rho_{lc}(T_{con})$	$\rho_{strong}(T_{gen}, X_{strong})$
$\boldsymbol{M}$	M_{con}	M_{gen}
$\boldsymbol{\dot{m}_l}$	$\dot{m}_{lc}$	$\dot{m}_{strong}$

The liquid density ρ_{lc} is evaluated at T_{con} using the Florides et al. (2003) correlations for pure water, and ρ_{strong} is evaluated at (T_{gen}, X_{strong}) using the Kaita (2001) density correlation. Since both throttling processes are isenthalpic, the fluid enthalpy is conserved across each valve. The refrigerant enters the evaporator at $h_{lc}(T_{con})$ from Eq. (4.45), and the strong solution enters the absorber at $H(T_{gen,°C}, X_{strong})$ from Eq. (4.13).

4.7.2 Solution Pump

The mass flow rate of the weak solution from the absorber is determined by the solution pump. The volume flow rate of the pump is assumed to be proportional to the pump rotary speed, adjusted by the frequency converter. The weak solution mass flow rate is therefore expressed as (Wen et al., 2019)

$$\dot{m}_{weak} = k\,\rho_{weak}\,f_p\,V_p \qquad (4.63)$$

where k is a proportional coefficient determined by the properties of the pump; ρ_{weak} is the density of the weak solution at absorber conditions (T_{abs}, X_{weak}), evaluated using the Kaita (2001) density correlation; f_p is the solution pump frequency; and V_p is the inner volume of the pump.

Since the pump work is negligibly small relative to the cycle enthalpy differences — typically less than 1% of the generator heat input — the temperature rise across the pump is negligible, and the pump outlet temperature is approximated as (Florides et al., 2003)

$$T_{pump,out} \approx T_{abs} \qquad (4.64)$$

This value serves directly as the cold-side inlet boundary condition $T_{c,in,1}$ to the SHX, as defined in Eq. (4.59).

4.8 State-Space Reduction

The sub-models derived in Sections 4.2 through 4.7 yield a set of coupled differential equations whose state variables are not all independent. Two global conservation constraints — one for the LiBr mass and one for the total system mass — allow two variables to be eliminated algebraically, reducing the system to a minimal set of six independent state variables (Wen et al., 2019).

4.8.1 Mass Conservation Constraints

The overall mass of LiBr salt and the overall mass of all fluid within the chiller are both fixed quantities determined during manufacture. Neglecting the mass in the connecting pipes — treating them as part of the main components — the two global conservation equations are (Wen et al., 2019)

$$M_{gen}\, X_{strong} + M_{abs}\, X_{weak} = M_{LiBr} \qquad (4.65)$$

$$M_{gen} + M_{con} + M_{eva} + M_{abs} = M_{total} \qquad (4.66)$$

From Eq. (4.65) and (4.66), while any four of the six variables on the left-hand sides are determined, the remaining two can be calculated as intermediate variables. In the present model, M_{abs} and M_{eva} are chosen as the intermediate variables and are eliminated from the state vector (Wen et al., 2019)

$$M_{abs} = \frac{M_{LiBr} - M_{gen}\, X_{strong}}{X_{weak}} \qquad (4.67)$$

$$M_{eva} = M_{total} - M_{gen} - M_{con} - \frac{M_{LiBr} - M_{gen}\, X_{strong}}{X_{weak}} \qquad (4.68)$$

Both quantities are recomputed algebraically at every time step from the current values of the remaining state variables.

4.8.2 Phase-Change Simplification

Since the latent heat of the refrigerant water is much larger than the sensible heat, the heat transfer in both the condenser and evaporator can be treated as a pure phase-change process. Under this assumption, the sensible accumulation terms $M_{con}\, dh_{lc}/dt$ and $M_{eva}\, dh_{leva}/$

dt are negligible and are dropped, as established in Sections 4.4.2 and 4.5.2. The energy balances of the condenser and evaporator then simplify directly to expressions for the refrigerant mass flow rates (Wen et al., 2019)

$$\dot{m}_{v,gen} = \frac{\dot{Q}_{con}}{h_{v,gen} - h_{lc}} \qquad (4.69)$$

$$\dot{m}_{v,abs} = \frac{\dot{Q}_{eva}}{h_{v,abs} - h_{lc}} \qquad (4.70)$$

4.8.3 The Reduced State Vector and Input Vector

Applying the constraints above, the system is fully described by six independent differential state variables (Wen et al., 2019)

$$\mathbf{x} = [M_{gen} \quad T_{gen} \quad X_{strong} \quad M_{con} \quad T_{abs} \quad X_{weak}]^T \qquad (4.71)$$

The external input vector to the model is (Wen et al., 2019)

$$\mathbf{u} = [\dot{m}_{hw} \quad \dot{m}_{clw} \quad \dot{m}_{chw} \quad T_{hw,i} \quad T_{clw,i} \quad T_{chw,i} \quad f_p]^T \qquad (4.72)$$

where $\dot{m}_{hw}, \dot{m}_{clw}, \dot{m}_{chw}$ are the mass flow rates and $T_{hw,i}, T_{clw,i}, T_{chw,i}$ are the inlet temperatures of the hot water, cooling water, and chilled water circuits respectively, and f_p is the solution pump frequency. All remaining system quantities are recovered as algebraic outputs from $\mathbf{x}$ and $\mathbf{u}$ at each time step.

4.9 Performance Metrics

The performance of the absorption chiller is evaluated from the simulation outputs using the following standard metrics.

4.9.1 Coefficient of Performance

The thermal COP is the primary performance indicator of the absorption chiller, defined as the ratio of the useful cooling effect produced in the evaporator to the heat input supplied at the generator (Wen et al., 2019)

$$\text{COP} = \frac{\dot{Q}_{eva}}{\dot{Q}_{gen}} \qquad (4.73)$$

Since the solution pump work $\dot{W}_{pump}$ is negligibly small compared to $\dot{Q}_{gen}$, it is omitted from the denominator without meaningful loss of accuracy (Wen et al., 2019).

4.9.2 Energy Balance Verification

At steady state, the first law of thermodynamics requires that the total heat input equals the total heat rejection. This provides an internal consistency check on the simulation (Wen et al., 2019)

$$\dot{Q}_{gen} + \dot{Q}_{eva} = \dot{Q}_{con} + \dot{Q}_{abs} \qquad (4.74)$$

Deviation from Eq. (4.74) at steady state quantifies the numerical energy imbalance of the model and is used as a convergence diagnostic.

5 Simulation and Implementation in Simulink

5.1 Simulink Model Architecture

Chapter 4 established the complete mathematical formulation of the single-effect LiBr/H_2O absorption chiller, comprising the governing differential equations, thermophysical property correlations, and the reduced six-variable state-space representation. This chapter describes the translation of that mathematical framework into a fully operational dynamic simulation environment. The model is implemented in MATLAB/Simulink, which provides a graphical, block-diagram-based platform well suited to the hierarchical, multi-domain structure of the chiller model. Each subsection addresses a distinct aspect of the implementation: the overall model architecture and inter-subsystem signal flow, the key architectural modifications introduced for numerical stability, the solver configuration, and finally the definition of the initial conditions and simulation scenarios used to generate the results presented in Chapter 6.

The top-level Simulink model, shown in Figure 2, presents the absorption chiller system as seven interconnected colour-coded subsystem blocks:

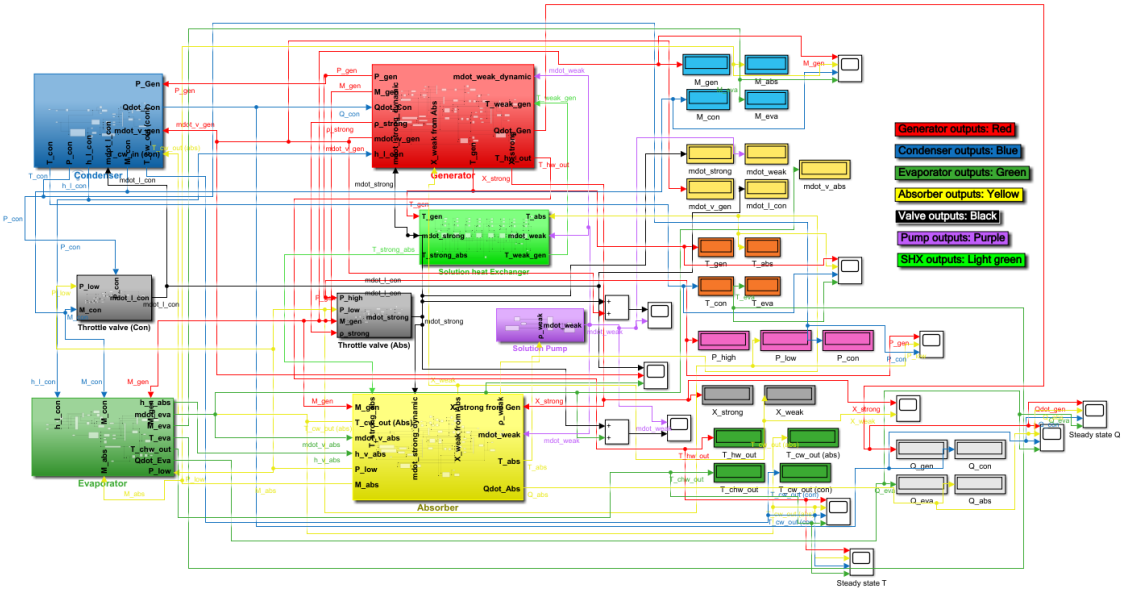

Figure 2: Top-level Simulink model of the single-effect LiBr/H_2O absorption chiller showing the seven interconnected subsystems and inter-subsystem signal flow.

The Generator (red), Condenser (blue), Evaporator (green), Absorber (yellow), Solution Heat Exchanger (light green), Throttle valve (Con) (dark grey), Throttle valve (Abs) (dark grey), and Solution Pump (purple). A dedicated output layer of labelled display and scope blocks on the right-hand side of the diagram logs all key simulation signals continuously, organised by

subsystem colour for traceability. The following describes the principal external boundary inputs and the key internal signals generated and exchanged between subsystems.

Generator

The sole external boundary input to the Generator is the hot water supply: inlet temperature $T_{hw,i}$ and mass flow rate $\dot{m}_{hw}$. Internally, the Generator integrates the state equations for T_{gen}, X_{strong}, and M_{gen}. It is the origin of the high-side pressure P_{gen}, which propagates to the Condenser and both throttle valves. The strong solution mass flow rate $\dot{m}_{strong}$ is passed to the Throttle valve (Abs), and the refrigerant vapour mass flow rate $\dot{m}_{v,gen}$ is passed to the Condenser. The preheated weak solution temperature $T_{weak,gen}$ arriving from the SHX enters the Generator as the solution inlet condition.

Condenser

The Condenser receives P_{gen}, $\dot{m}_{v,gen}$, and $h_{l,gen}$ internally from the Generator, and M_{con} as state feedback from its own integrator. The external boundary input is the cooling water inlet temperature $T_{clw,i,con}$, which is not the external supply temperature but the absorber cooling water outlet $T_{cw,out(Abs)}$, enforcing the series cooling water arrangement. The Condenser produces P_{con}, T_{con}, $h_{l,con}$, and $\dot{Q}_{con}$ as internal outputs distributed to the Throttle valve (Con), Evaporator, and the output logging layer.

Throttle Valve (Con)

The refrigerant throttle valve receives P_{con} from the Condenser, the low-side pressure P_{low} from the Absorber, and the accumulated mass M_{con} from the Condenser integrator. It computes $\dot{m}_{l,con}$, which is passed to both the Condenser mass balance and the Evaporator inlet.

Evaporator

The Evaporator receives $h_{l,con}$, M_{con}, and $\dot{m}_{l,con}$ from the Condenser and its throttle valve, and P_{low} from the Absorber. The external boundary input is the chilled water inlet temperature $T_{chw,i}$ and mass flow rate $\dot{m}_{chw}$. The Evaporator integrates the state equation for M_{eva} and produces $\dot{Q}_{eva}$, T_{eva}, $\dot{m}_{v,abs}$, and $h_{v,abs}$, all of which are passed to the Absorber.

Absorber

The Absorber receives $\dot{m}_{strong}$ and $T_{strong,abs}$ from the Throttle valve (Abs) and SHX respectively, and $\dot{m}_{v,abs}$ and $h_{v,abs}$ from the Evaporator. It also receives M_{gen} and X_{strong} from the Generator to compute M_{abs} algebraically via the LiBr conservation constraint. The external boundary input is the cooling water inlet temperature $T_{clw,i}$ and mass flow rate $\dot{m}_{clw}$. The Absorber integrates the state equations for T_{abs} and X_{weak}, and produces the low-side pressure P_{low}, $\dot{Q}_{abs}$, ρ_{weak}, and the cooling water outlet temperature $T_{cw,out(Abs)}$, which feeds forward as the cooling water inlet to the Condenser.

Throttle Valve (Abs) and Solution Pump

The Throttle valve (Abs) receives P_{gen}, P_{low}, M_{gen}, and ρ_{strong} and computes $\dot{m}_{strong}$, closing the solution loop back to the Absorber. The Solution Pump receives ρ_{weak} from the Absorber and the external input pump frequency f_p, and computes $\dot{m}_{weak}$, which is distributed to both the Absorber and the Generator to close the weak solution loop.

Solution Heat Exchanger

The SHX receives T_{gen} and $\dot{m}_{strong}$ as hot-side boundary conditions from the Generator, and T_{abs} and $\dot{m}_{weak}$ as cold-side boundary conditions from the Absorber and Solution Pump respectively. It integrates the 16 node temperature state equations and returns the preheated weak solution temperature $T_{weak,gen}$ to the Generator inlet and the cooled strong solution temperature $T_{strong,abs}$ to the Throttle valve (Abs).

5.2 Subsystem Implementation

This section describes the internal Simulink implementation of each subsystem in turn, explaining how the governing equations are realised using integrator blocks, MATLAB Function blocks, and feedback signal routing.

5.2.1 Generator Subsystem

The internal structure of the Generator subsystem is shown in Figure 3. The subsystem implements three parallel signal paths corresponding to the three governing equations of Section 4.2: the mass balance, the species balance, and the energy balance, each culminating

in a dedicated Simulink integrator block that advances the respective state variable forward in time.

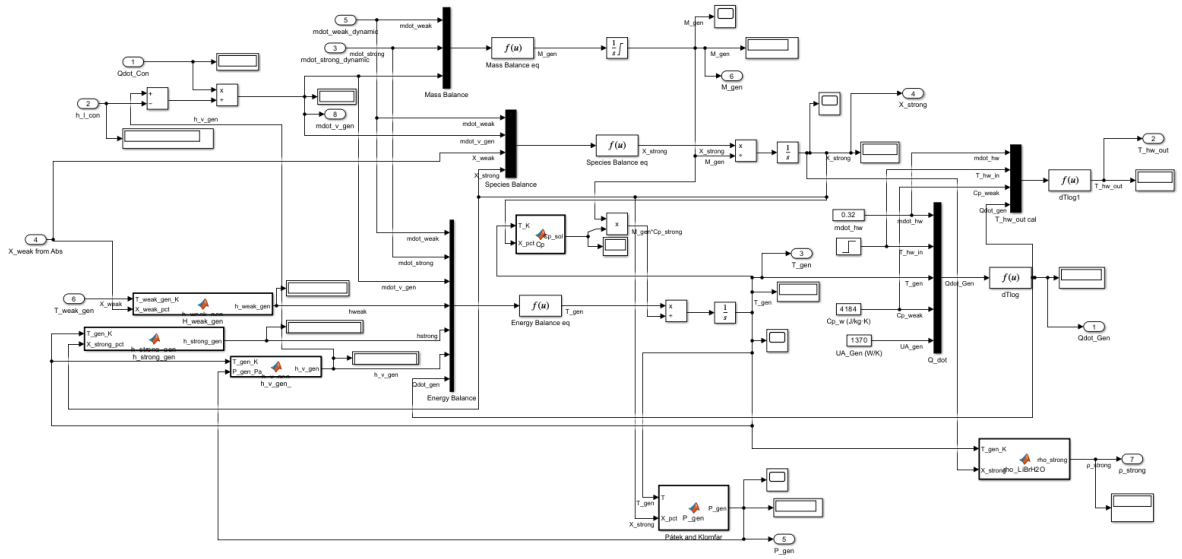

Figure 3: Internal Simulink implementation of the Generator subsystem.

Mass Balance: The mass balance path assembles the net mass flux $(\dot{m}_{weak} - \dot{m}_{strong} - \dot{m}_{v,gen})$ from the incoming and outgoing stream signals and passes it through a MATLAB Function block labelled *Mass Balance eq*. The output is fed into a $1/s$ integrator whose state is M_{gen}, displayed and routed to the output port.

Species Balance: The species balance path receives $\dot{m}_{weak}$, $\dot{m}_{v,gen}$, and the current concentration X_{weak} from the Absorber. A MATLAB Function block labelled *Species Balance eq* evaluates the right-hand side of Eq. (4.5), and the result is divided by M_{gen} before entering the $1/s$ integrator for X_{strong}. This division implements the $1/M_{gen}$ coefficient on the left-hand side of the species balance state equation.

Energy Balance. The energy balance path is the most involved. It first evaluates all required enthalpies and the solution specific heat capacity through dedicated property function blocks: the block labelled H_weak_gen computes $h_{weak,gen}$ at $(T_{weak,gen}, X_{weak})$ using the Kaita correlations; h_strong_gen computes h_{strong} at (T_{gen}, X_{strong}); and h_v_gen computes the refrigerant vapour enthalpy $h_{v,gen}$ at (T_{gen}, P_{gen}) using the Florides polynomial of Eq. (4.45). The specific heat capacity $c_{p,sol}$ is evaluated by the block labelled $T\_K/X\_pct/Cp$ at the current generator state (T_{gen}, X_{strong}). These property values feed into the MATLAB Function block *Energy Balance eq*, which evaluates the right-hand side of Eq. (4.6). The result is divided by the product $M_{gen} \cdot c_{p,strong}$ before entering the $1/s$ integrator for T_{gen}.

Heat Transfer and Property Outputs. The heat transfer rate $\dot{Q}_{gen}$ is computed by the *Q_dot* block using the LMTD expression of Eq. (4.9), receiving T_{gen}, $T_{hw,i}$, $\dot{m}_{hw}$, $c_{p,w}$, and $UA_{gen} = 1370$ W/K as inputs. The hot water outlet temperature $T_{hw,out}$ is then computed by the *dTlog1* MATLAB Function block via Eq. (4.11). The high-side pressure P_{gen} is computed by the *Pátek and Klomfar* function block at (T_{gen}, X_{strong}) using the equilibrium pressure correlation of Eqs. (4.15)–(4.16), and the strong solution density ρ_{strong} is evaluated by the *rho_LiBrH2O* block at the same state, both routed to the output ports for use by the throttle valves and the condenser pressure scaling mechanism.

Refrigerant Vapour Mass Flow Rate. The vapour mass flow rate $\dot{m}_{v,gen}$ is evaluated algebraically within the Generator subsystem, consistent with the phase-change simplification of Eq. (4.76). The condenser heat transfer rate $\dot{Q}_{con}$ and the saturated liquid enthalpy $h_{l,con}$ are received as inputs from the Condenser subsystem, and the refrigerant vapour enthalpy $h_{v,gen}$ is computed internally at (T_{gen}, P_{gen}) using the Florides polynomial of Eq. (4.45). The three signals are combined algebraically as $\dot{m}_{v,gen} = \dot{Q}_{con}/(h_{v,gen} - h_{l,con})$ and routed to output port 8, from where it is distributed to the Condenser mass balance and the solution mass balances.

5.2.2 Condenser Subsystem

The internal structure of the Condenser subsystem is shown in Figure 4. Unlike the Generator and Absorber, the Condenser implements only a single integrator, reflecting the fact that it contributes one state variable to the reduced state vector: the accumulated liquid refrigerant mass M_{con}.

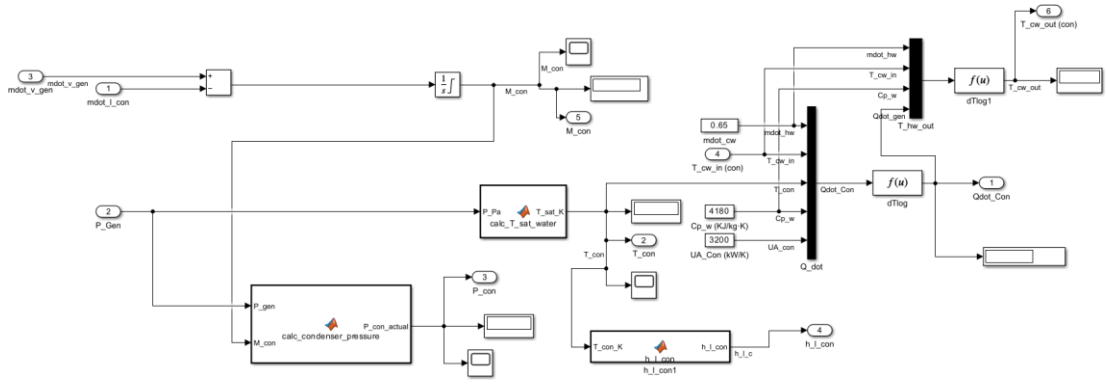

Figure 4: Internal Simulink implementation of the Condenser subsystem

Mass Balance. The mass balance path assembles the net refrigerant mass flux $(\dot{m}_{v,gen} - \dot{m}_{l,con})$ from the incoming vapour and outgoing liquid stream signals. This net flux is fed directly into a $1/s$ integrator whose state is M_{con}, which is routed to the output port and fed back internally to the condenser pressure scaling block and the Throttle valve (Con).

Condenser Pressure. The condenser pressure P_{con} is not taken directly as P_{gen} but is computed by the dedicated *calc_condenser_pressure* function block, which implements the dynamic pressure scaling mechanism of Eq. (4.38) using P_{gen} and the current M_{con} as inputs. The resulting P_{con} is routed to the output port and fed forward to the Throttle valve (Con). The full rationale for this mechanism is discussed separately in Section 5.3.

Condenser Temperature and Enthalpy. The condenser temperature T_{con} is computed by the *calc_T_sat_water* function block, which implements the Antoine equation of Eqs. (4.39) – (4.41) at the prevailing P_{con}. The saturated liquid enthalpy $h_{l,con}$ is then computed by the *h_l_con* function block using the Florides et al. (2003) polynomial correlations of Eqs. (4.42) – (4.44), evaluated at T_{con}. Both T_{con} and $h_{l,con}$ are routed to the output ports for use by the Evaporator and the heat transfer block.

Heat Transfer Rate and Cooling Water Outlet Temperature. The heat transfer rate $\dot{Q}_{con}$ is computed by the *Q_dot* block using the LMTD expression of Eq. (4.35), receiving T_{con}, $T_{clw,i,con}$, $\dot{m}_{clw}$, $c_{p,w}$, and UA_{con} as inputs. The cooling water outlet temperature $T_{cw,out(con)}$ is then recovered directly from Eq. (4.36) inside the *dTlog1* MATLAB Function block and is routed to the output logging layer.

5.2.3 Throttle Valve (Con) Subsystem

The internal structure of the Throttle Valve (Con) subsystem is shown in Figure 5. The subsystem contains no integrator blocks — it is a purely algebraic signal path that evaluates the refrigerant liquid mass flow rate $\dot{m}_{l,con}$ at each time step from Eq. (4.61). The liquid density ρ_l is approximated as the constant value $\rho_{water} = 1000$ kg/m³ for the saturated liquid refrigerant. The dynamic liquid head Z is computed from the accumulated condenser mass M_{con} and the fixed base area A using Eq. (4.62), and the fixed height offset $z = 0.2$ m is added to form the total head term $(Z+z)$.

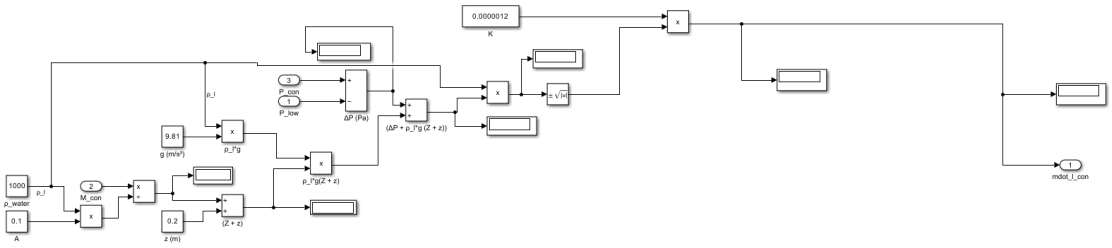

Figure 5: Internal Simulink implementation of the Throttle Valve (Con) subsystem showing the hydrostatic head computation, pressure differential assembly, and the empirical valve flow equation realisation producing $\dot{m}_{l,con}$.

The gravitational term $\rho_l \cdot g \cdot (Z + z)$ is then assembled and added to the pressure differential $\Delta P = P_{con} - P_{low}$ to form the total driving term $(\Delta P + \rho_l\, g\, (Z + z))$ inside the block labelled $(\Delta P + \rho\_l * g * (Z + z))$. This combined term is passed through a square root block $\sqrt{|\,u\,|}$ — the absolute value guardrail preventing negative square root arguments during transients — and multiplied by ρ_l and the valve constant $K = 1.2 \times 10^{-6}$ m² (combining $A_{vl} \cdot C_{vl}$) to produce $\dot{m}_{l,con}$ at the single output port, which is routed to both the Condenser mass balance and the Evaporator inlet.

5.2.4 Evaporator Subsystem

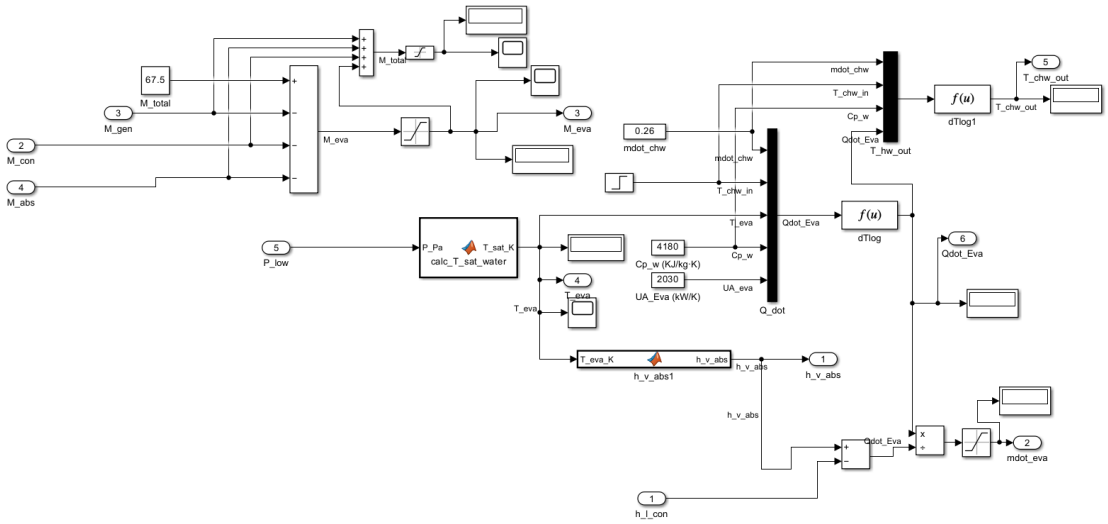

Figure 6: Internal Simulink implementation of the Evaporator subsystem

The internal structure of the Evaporator subsystem is shown in Figure 6. Like the Condenser, the Evaporator contains no integrator for its own mass state — M_{eva} is instead recovered

algebraically via the global mass conservation constraint of Eq. (4.68) and contributes no differential equation of its own.

Evaporator Mass Recovery. The accumulated evaporator mass M_{eva} is computed at the top of the subsystem by subtracting M_{gen}, M_{con}, and M_{abs} from the fixed total system mass $M_{total} = 67.5$ kg, implementing Eq. (4.68) directly. A saturation block clamps M_{eva} to a physically meaningful non-negative range, preventing solver instability during cold-start transients when the mass distribution has not yet settled. The resulting M_{eva} is routed to the output port and to the display blocks.

Evaporator Temperature. The low-side pressure P_{low} is received from the Absorber at input port 5 and passed into the *calc_T_sat_water* function block, which evaluates the evaporating temperature T_{eva} via the Antoine equation of Eqs. (4.52)–(4.54). The resulting T_{eva} is displayed and routed to the heat transfer block and to the output port.

Refrigerant Vapour Enthalpy. The saturated vapour enthalpy $h_{v,abs}$ is computed by the *h_v_abs* function block, which evaluates the Florides et al. (2003) polynomial of Eq. (4.56) at T_{eva}. This value is routed to output port 1 for use by the Absorber energy balance.

Heat Transfer Rate and Chilled Water Outlet Temperature. The heat transfer rate $\dot{Q}_{eva}$ is computed by the *Q_dot* block using the LMTD expression of Eq. (4.50), receiving T_{eva}, $T_{chw,i}$, $\dot{m}_{chw} = 0.26$ kg/s, $c_{p,w} = 4180$ J/(kg·K), and $UA_{eva} = 2030$ W/K as inputs. The chilled water outlet temperature $T_{chw,out}$ is then recovered from Eq. (4.51) inside the *dTlog1* MATLAB Function block and routed to output port 5 as the primary cooling performance output.

Refrigerant Vapour Mass Flow Rate. The vapour mass flow rate leaving the evaporator $\dot{m}_{v,abs}$ is evaluated algebraically from the quasi-steady energy balance of Eq. (4.49). The numerator $\dot{Q}_{eva} + \dot{m}_{l,con}(h_{l,con} - h_{leva})$ is assembled from $\dot{Q}_{eva}$, the incoming liquid enthalpy $h_{l,con}$ received at input port 1, and $h_{v,abs}$, and divided by $(h_{v,abs} - h_{leva})$ to produce $\dot{m}_{v,abs}$ at output port 2. A saturation block is applied to prevent negative flow rates during transients. This value is passed to the Absorber energy balance to close the refrigerant loop.

5.2.5 Absorber Subsystem

The internal structure of the Absorber subsystem is shown in Figure 7. The Absorber mirrors the Generator in structural complexity, implementing two state variable integrators — one for X_{weak} and one for T_{abs} — alongside algebraic paths for mass recovery, property evaluation, pressure computation, and heat transfer

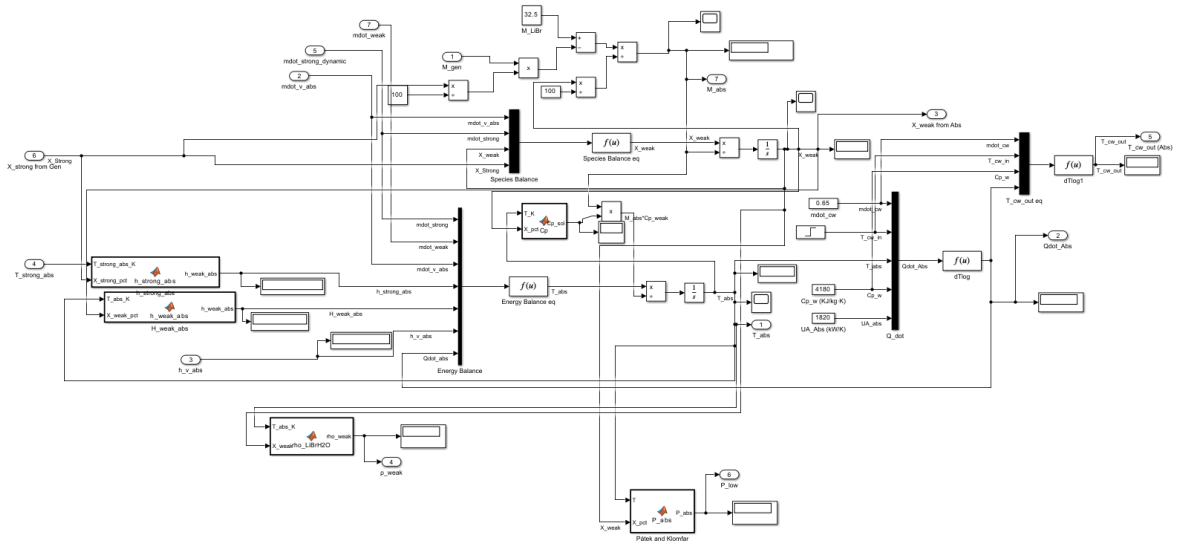

Figure 7: Internal Simulink implementation of the Absorber subsystem

Absorber Mass Recovery. The absorber solution mass M_{abs} is not integrated directly but recovered algebraically at each time step from the LiBr conservation constraint of Eq. (4.67). The fixed total LiBr mass $M_{LiBr} = 32.5$ kg is stored as a constant, and M_{abs} is computed from M_{gen}, X_{strong}, and X_{weak} using two multiply blocks and a subtraction, with the result scaled by the factor 100 to handle the percentage-based concentration convention used internally. The recovered M_{abs} is routed to output port 7 and fed back into the species and energy balance paths.

Species Balance. The species balance path receives $\dot{m}_{v,abs}$, $\dot{m}_{strong}$, $\dot{m}_{weak\_dynamic}$, X_{strong}, and the current X_{weak} as inputs. The MATLAB Function block labelled *Species Balance eq* evaluates the right-hand side of Eq. (4.21), and the result is divided by M_{abs} before entering the $1/s$ integrator for X_{weak}. The integrated X_{weak} is routed to output port 3 and fed back to the species balance, the energy balance, the pressure block, and the density block.

Energy Balance. The energy balance path evaluates all required enthalpies through dedicated property function blocks: h_strong_abs computes the enthalpy of the strong solution entering from the throttle valve at $(T_{strong,abs}, X_{strong})$ using the Kaita

correlations; H_weak_abs computes the enthalpy of the weak solution at the current absorber state (T_{abs}, X_{weak}); and $h_{v,abs}$ is received directly at input port 3 from the Evaporator. The solution specific heat capacity $c_{p,sol}$ is evaluated by the $T\_K/X\_pct/Cp$ block at (T_{abs}, X_{weak}). These values feed into the MATLAB Function block *Energy Balance eq*, which evaluates the right-hand side of Eq. (4.24). The result is divided by $M_{abs} \cdot c_{p,weak}$ before entering the $1/s$ integrator for T_{abs}, which is routed to output port 1 and fed back throughout the subsystem.

Heat Transfer Rate and Cooling Water Outlet Temperature. The heat transfer rate $\dot{Q}_{abs}$ is computed by the *Q_dot* block using the LMTD expression of Eq. (4.25), receiving T_{abs}, $T_{clw,i}$, $\dot{m}_{clw} = 0.65$ kg/s, $c_{p,w} = 4180$ J/(kg·K), and $UA_{abs} = 1820$ W/K as inputs. The cooling water outlet temperature $T_{cw,out(Abs)}$ is then recovered inside the *dTlog1* MATLAB Function block via Eq. (4.25) and routed to output port 5, from where it feeds forward as the cooling water inlet to the Condenser subsystem, enforcing the series cooling water arrangement.

Low-Side Pressure and Solution Density. The low-side pressure $P_{low} = P_{abs}$ is computed by the *Pátek and Klomfar* function block at the current absorber state (T_{abs}, X_{weak}) using the equilibrium pressure correlations of Eqs. (4.15)–(4.16) and is routed to output port 6 for distribution to the Evaporator and both throttle valves. The weak solution density ρ_{weak} is evaluated by the *rho_LiBrH2O* function block at (T_{abs}, X_{weak}) and routed to output port 4 for use by the Solution Pump.

5.2.6 Throttle Valve (Abs) Subsystem

The internal structure of the Throttle Valve (Abs) subsystem is shown in Figure 8. The implementation follows the same signal path as Section 5.2.3, with two substitutions: the liquid density ρ_l is the dynamic strong solution density ρ_{strong} received from the Generator at input port 4 — rather than the fixed water density used in the refrigerant valve — and the liquid head Z is computed from the accumulated generator mass M_{gen} rather than M_{con}. The pressure differential $\Delta P = P_{high} - P_{low}$ drives the flow, and the valve constant is $K = 0.0000085 \times 1.38$. The single output $\dot{m}_{strong}$ is routed to the Absorber and the SHX to close the solution loop.

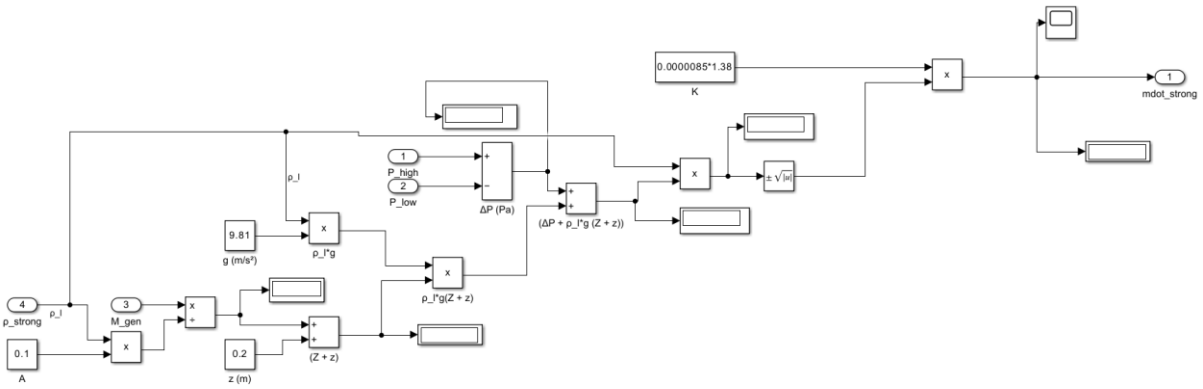

Figure 8: Internal Simulink implementation of the Throttle Valve (Abs) subsystem showing the strong solution hydrostatic head computation, pressure differential assembly, and the empirical valve flow equation producing $\dot{m}_{strong}$.

5.2.7 Solution Pump Subsystem

The internal structure of the Solution Pump subsystem is shown in Figure 9. The subsystem is purely algebraic and implements Eq. (4.63) directly. The weak solution mass flow rate $\dot{m}_{weak}$ is computed as the product of the pump frequency $f_p = 30.8$ Hz, the weak solution density ρ_{weak} received from the Absorber, and the pump displacement constant $K = 1.096 \times 10^{-6}$ m³, following the formulation of Wen et al. (2019). The resulting $\dot{m}_{weak}$ is routed to the Generator and Absorber to close the weak solution loop.

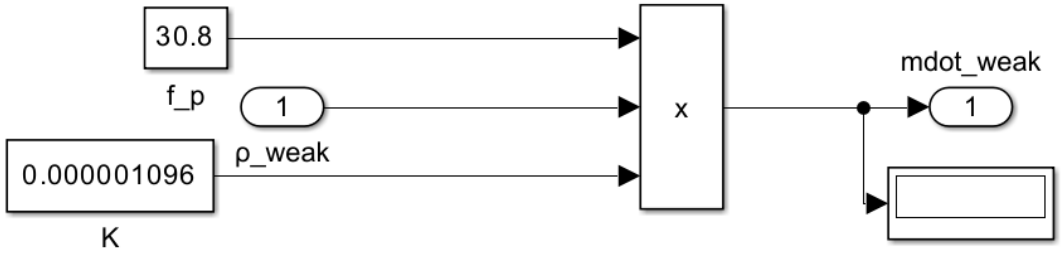

Figure 9: Internal Simulink implementation of the Solution Pump subsystem showing the algebraic computation of $\dot{m}_{weak}$ from pump frequency, weak solution density, and pump displacement constant

5.2.8 Solution Heat Exchanger Subsystem

The internal structure of the Solution Heat Exchanger subsystem is shown in Figures 10 and 11. The SHX is the most structurally distinctive subsystem in the model, implementing the 8-stage discretised counter-flow heat exchanger described in Section 4.6. Rather than a single

lumped energy balance, the subsystem consists of eight identical subsystem blocks chained in series, each contributing two integrators — one for the hot-side node temperature $T_{h,i}$ and one for the cold-side node temperature $T_{c,i}$ — yielding 16 state variables in total.

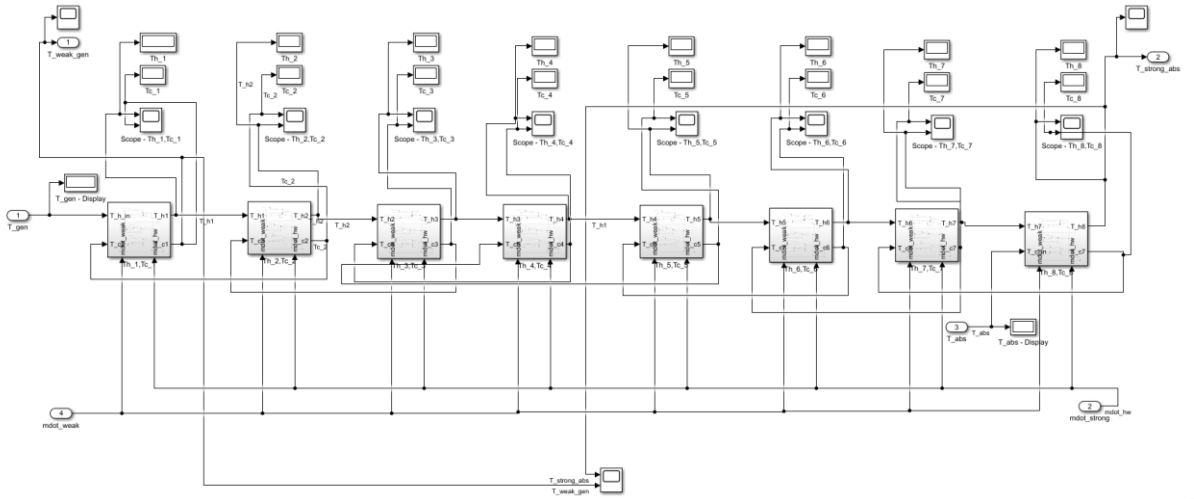

Figure 10: Full Simulink implementation of the Solution Heat Exchanger subsystem showing the eight chained node blocks in counter-flow arrangement, with T_{gen} and T_{abs} as boundary inlets and $T_{strong,abs}$ and $T_{weak,gen}$ as outlet outputs.

Stage Chaining and Counter-Flow Arrangement. As shown in Figure 10, the eight node blocks are connected in a counter-flow arrangement: the hot-side inlet T_{gen} enters at node 1 (left) and the hot-side outlet $T_{h,8}$ exits at node 8 (right) as $T_{strong,abs}$; conversely, the cold-side inlet T_{abs} enters at node 8 (right) and the cold-side outlet $T_{c,1}$ exits at node 1 (left) as $T_{weak,gen}$. The mass flow rates $\dot{m}_{strong}$ and $\dot{m}_{weak}$ are assumed to be same in all eight nodes. The hot-side outlet of node i feeds directly into the hot-side inlet of node $i+1$, and the cold-side outlet of node $i+1$ feeds into the cold-side inlet of node i, forming the counter-flow cascade.

Individual Node Implementation. The internal structure of a single node block is shown in Figure 11. Each node implements Eqs. (4.58) and (4.59) through two parallel integrator paths. The hot-side path assembles the terms $\dot{m}_{strong}/m \cdot (T_{h,in} - T_{h,i})$ and $K_1/(m \cdot c_{p,1}) \cdot (T_{h,i} - T_{c,i})$ — where m is the nodal fluid mass, $c_{p,1} = 4186$ J/(kg·K), and $K_1 = 50$ W/K is the inter-node heat transfer conductance — subtracts the inter-node heat exchange term and feeds the result into integrator1 for $T_{h,i}$. The cold-side path similarly assembles $\dot{m}_{weak}/m \cdot (T_{c,2} - T_{c,i})$ and adds the heat exchange term $K_1/(m \cdot c_p) \cdot (T_{h,i} - T_{c,i})$ before feeding into the integrator for $T_{c,i}$. Both integrated temperatures are routed to the output ports and fed back internally to close the node energy balance.

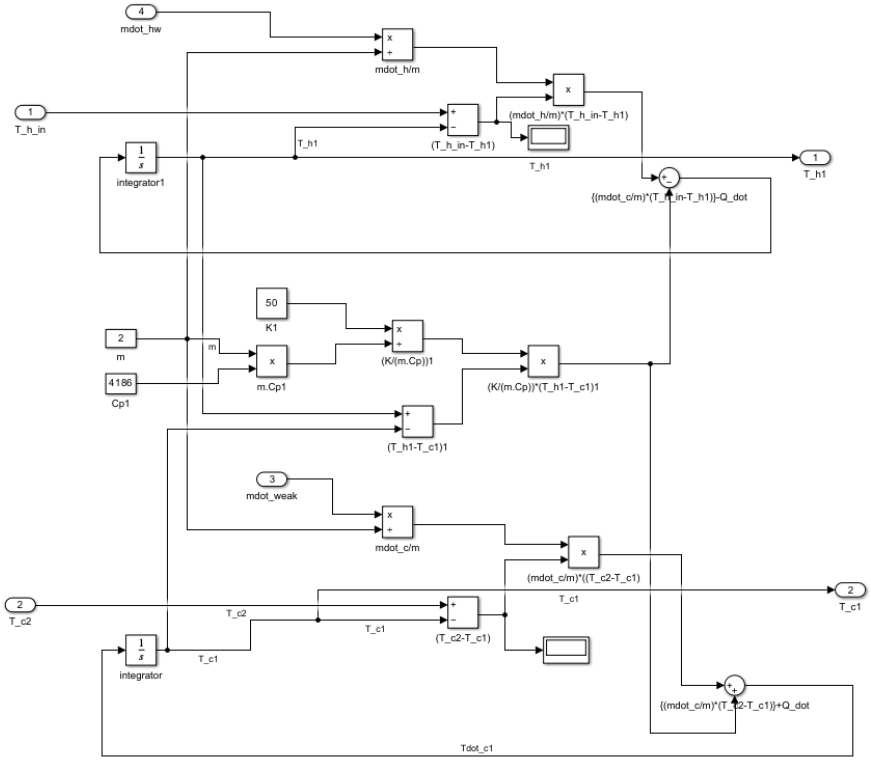

Figure 11: Internal Simulink implementation of a single SHX node block showing the parallel hot-side and cold-side integrator paths, the inter-node heat transfer term, and the advective transport terms for $T_{h,i}$ and $T_{c,i}$.

5.3 Solver Configuration

The Simulink model is integrated using the ode23tb solver (stiff/TR-BDF2) with a variable time step. The solver settings are configured as follows: relative tolerance of 1×10^{-3}, absolute tolerance set to auto with automatic scaling enabled, maximum step size of 100 s, and minimum step size and initial step size both set to auto. Zero-crossing detection is disabled for all signals, and the solver Jacobian method is set to auto. The solver reset method is set to Fast. The ode23tb solver is an implicit, variable-step solver designed for stiff systems, making it well suited to the present model where the 16 SHX node equations, the mass balance integrators, and the nonlinear property function evaluations collectively produce a wide separation of time scales — the hallmark of a stiff ODE system. The non-stiff explicit solver ode45 (Dormand-Prince) was also tested during development but produced erratic transient behaviour and solver failures during cold-start conditions, where rapid changes in pressure and mass flow rates generate large fast-varying derivatives that violate the step-size stability requirements of explicit methods. The implicit ode23tb solver handles these stiff phases robustly, allowing larger steps during slow dynamics while automatically reducing the step size during fast transients.

5.4 Initial Conditions and Simulation Scenarios

Initial Conditions

All temperatures in the Simulink model are expressed in Kelvin throughout. The input temperatures listed in Table 5 are therefore specified in Kelvin, and the initial state vector is converted accordingly. The state vector is ordered as:

$$\mathbf{x} = [M_{gen},\ T_{gen},\ X_{strong},\ M_{con},\ T_{abs},\ X_{weak}]^T$$

Following Wen et al. (2019), the initial state variables are set at physically reasonable but arbitrary values within the expected operating range rather than at a pre-computed equilibrium, allowing the solver to find the steady state dynamically from a cold-start condition. The initial state vector is:

$$\mathbf{x}_0 = [20,\ 323,\ 55,\ 5,\ 328,\ 39]^T$$

where M_{gen} and M_{con} are in kg, temperatures in K, and concentrations in wt%. The 16 SHX node temperatures — the $T_{h,i}$ and $T_{c,i}$ integrator states for $i = 1,\ldots,8$ — are all initialised uniformly at 293 K, representing an ambient-temperature cold-start condition.

Input Parameters

The fixed nominal input parameters applied as the baseline across all simulation scenarios are listed in Table 5.

Table 5 - Input parameters under on-design condition according to (Wen et al.*, 2019)*

Symbol	Description	Value
$\dot{m}_{hw}$	Hot water mass flow rate	0.32 kg/s
$\dot{m}_{clw}$	Cooling water mass flow rate	0.65 kg/s
$\dot{m}_{chw}$	Chilled water mass flow rate	0.26 kg/s
f_p	Solution pump frequency	30.8 Hz
$T_{hw,i}$	Inlet hot water temperature	368 K
$T_{cw,i}$	Inlet cooling water temperature	305 K
$T_{chw,i}$	Inlet chilled water temperature	288 K

Simulation Scenarios

Each simulation begins from $\mathbf{x}_0$ under nominal conditions. The system reaches steady state well before $t = 20000$ s, at which point a single step change is applied to one input while all others remain at their nominal values. This approach isolates the dynamic response to each

individual perturbation. Six step-change scenarios are defined across three input variables, giving a total of seven runs including the nominal baseline, as summarised in Table 6.

Table 6 - Simulation scenarios

Scenario	Description	Step Change at $\boldsymbol{t = 20000}$s
0	Nominal baseline	None — full cold-start to steady state
1	Lower inlet hot water temperature	$T_{hw,i}: 368 \rightarrow 363$K
2	Higher inlet hot water temperature	$T_{hw,i}: 368 \rightarrow 373$K
3	Higher inlet cooling water temperature	$T_{cw,i}: 305 \rightarrow 309$K
4	Lower inlet cooling water temperature	$T_{cw,i}: 305 \rightarrow 301$K
5	Higher inlet chilled water temperature	$T_{chw,i}: 288 \rightarrow 291$K
6	Lower inlet chilled water temperature	$T_{chw,i}: 288 \rightarrow 285$K

6 Results and Discussion

This chapter presents and analyses the simulation results obtained from the dynamic Simulink model developed in Chapter 5. Section 6.1 validates the model by demonstrating convergence to a physically consistent steady state under nominal operating conditions, discussing the cold-start transient behaviour and the final steady-state operating point. Sections 6.2 through 6.4 then present the dynamic step-change responses of the chiller to perturbations in the three external input temperatures — hot water, cooling water, and chilled water — examining the transient trajectories and the physical mechanisms governing each response.

6.1 Steady-State Validation (Nominal Baseline — Scenario 0)

The nominal baseline simulation is run from the arbitrary cold-start initial state $\mathbf{x}_0$ with all inputs held constant at their nominal values as defined in Section 5.4 for 35000 seconds. No step change is applied. The objective is to demonstrate that the model self-organises from an arbitrary initial condition and converges to a physically consistent, thermodynamically stable operating point under on-design conditions.

6.1.1 Mass Distribution Convergence

Figure 12 presents the time evolution of the solution and refrigerant mass stored in each of the four main components throughout the 35000 s simulation.

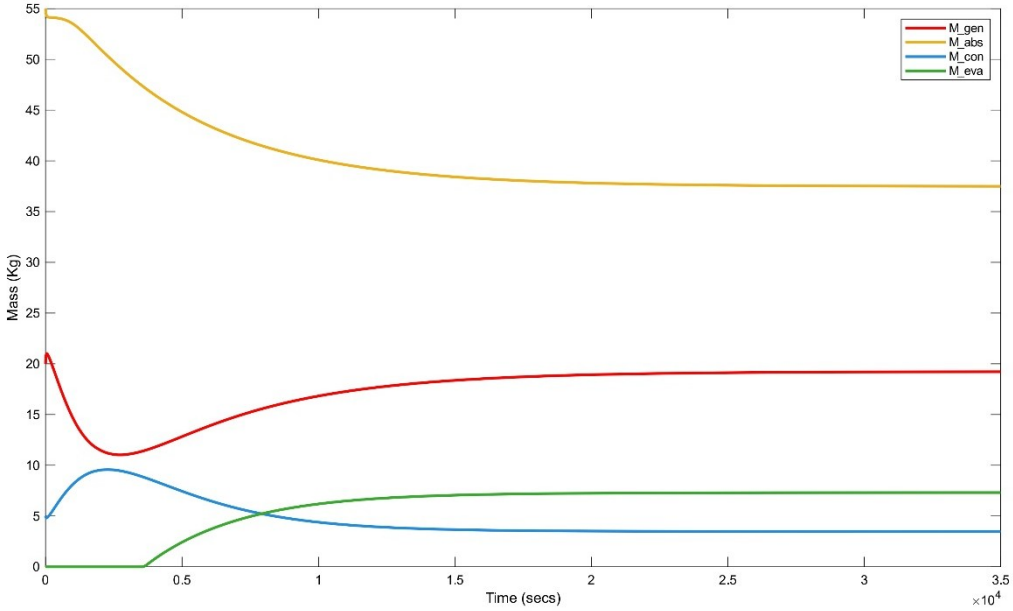

Figure 12: Time evolution of component fluid masses M_{gen}, M_{abs}, M_{con}, and M_{eva} during the nominal 35000 s simulation

Starting from $M_{gen,0} = 20$ kg and $M_{abs,0} = 55$ kg, the system undergoes a pronounced redistribution of mass during the cold-start transient. The absorber mass M_{abs} decreases monotonically from 55 kg as weak solution is continuously pumped to the generator, eventually settling at 37.49 kg. The generator mass M_{gen} exhibits a non-monotonic response: it initially drops sharply from 20 kg to approximately 11 kg before recovering and converging to 19.22 kg. This dip occurs because, in the early transient, the outflow of strong solution to the absorber via the SHX temporarily exceeds the inflow of weak solution from the pump before the generator temperature has risen sufficiently to establish a balanced desorption regime.

The condenser mass M_{con} rises from its initial value of 5 kg to a peak of approximately 10 kg before settling at 3.48 kg. This overshoot reflects the early excess of refrigerant vapour produced by the generator before the condenser reaches its operating temperature and the throttling flow to the evaporator becomes fully established. The evaporator mass M_{eva}, which starts at zero, builds up gradually as liquid refrigerant accumulates through the throttling device, converging to 7.31 kg. By approximately $t \approx 25000$ s, all four masses have stabilised. As a direct verification of global mass conservation, the steady-state sum $M_{gen} + M_{abs} + M_{con} + M_{eva} = 19.22 + 37.49 + 3.48 + 7.31 = 67.50$ kg exactly satisfies the design constraint $M_{total} = 67.5$ kg, confirming that the closed-loop mass balances in the model are correctly enforced throughout the simulation.

6.1.2 Solution Concentration Convergence

Figure 13 presents the time evolution of the strong and weak solution concentrations X_{weak} over the 35000 s simulation.

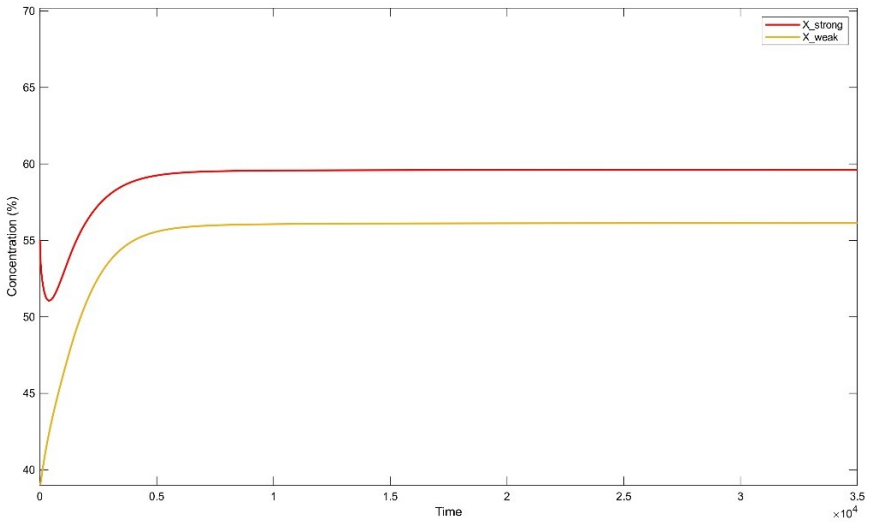

Figure 13: Time evolution of LiBr solution concentrations

Both concentrations begin at their initial values of 55 wt% and 39 wt% respectively. The strong solution concentration X_{strong} falls and then rises steeply in the first 3000 s as the generator rapidly heats up and drives desorption, temporarily increasing the LiBr fraction in the remaining generator solution. It reaches a peak of approximately 59.7 wt% before stabilising at 59.61 wt% at steady state. The weak solution concentration X_{weak} rises more gradually from 39 wt%, reflecting the slower accumulation of refrigerant-rich solution in the absorber as the refrigerant cycle becomes established, converging to 56.13 wt% by approximately $t = 15000$ s. The resulting steady-state concentration difference $\Delta X = X_{strong} - X_{weak} = 3.48$ wt% represents the effective absorption driving force of the cycle. A larger ΔX would indicate a higher desorption rate and potentially greater cooling capacity; the moderate value obtained here is consistent with the nominal operating conditions and the relatively low hot water inlet temperature of 368 K. Both concentrations converge smoothly without oscillation, confirming the numerical stability of the species conservation integrators throughout the simulation.

6.1.3 Outlet Temperature Convergence

Figure 14 presents the time evolution of the four external circuit outlet temperatures — $T_{hw,out}$, $T_{cw,out(con)}$, $T_{cw,out(abs)}$, and $T_{chw,out}$ — displayed as a 2×2 subplot grid.

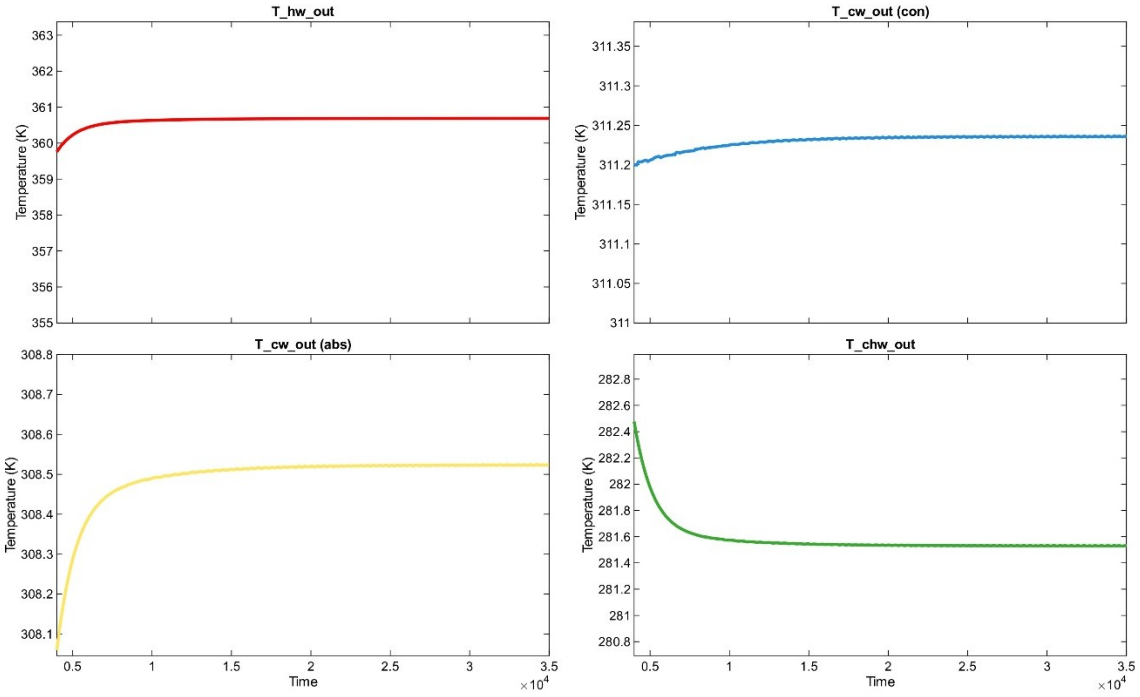

Figure 14: Time evolution of external circuit outlet temperatures $T_{hw,out}$, $T_{cw,out(con)}$, $T_{cw,out(abs)}$, and $T_{chw,out}$ during the nominal 35000 s simulation.

The hot water outlet temperature $T_{hw,out}$ rises smoothly from approximately 360 K and converges to 360.7 K. The relatively small temperature drop across the generator ($T_{hw,in} - T_{hw,out} = 368 - 360.7 = 7.3$ K) reflects the moderate heat transfer rate $\dot{Q}_{gen} = 9788$ W under the nominal hot water flow rate of 0.32 kg/s, and is consistent with the UA_{gen} value of 1370 W/K. The cooling water outlet at the condenser $T_{cw,out(con)}$ is notably stable throughout the entire simulation, converging to 311.2 K from the very beginning of the transient. This rapid stabilisation is attributable to the condenser's small fluid thermal mass — M_{con} is the smallest of all component masses — and the high $UA_{con} = 3200$ W/K, which enables efficient and almost instantaneous heat rejection to the cooling water circuit. The cooling water outlet at the absorber $T_{cw,out(abs)}$ rises sharply from 308.1 K and settles at 308.5 K within the first 5000 s, reflecting the early establishment of heat rejection in the absorber as strong solution begins flowing in from the generator. The narrow convergence range of only 0.4 K for $T_{cw,out(abs)}$ indicates that the absorber operating condition is relatively insensitive to the mass redistribution occurring elsewhere in the system during the cold start.

The chilled water outlet temperature $T_{chw,out}$ is the most operationally significant output of the chiller. It decreases from 282.5 K and converges to a steady-state value of 281.5 K (8.35 °C), representing a chilled water temperature lift of $T_{chw,in} - T_{chw,out} = 288 - 281.5 = 6.5$ K under the nominal flow rate of 0.26 kg/s. This corresponds to a steady-state evaporator cooling capacity of $\dot{Q}_{eva} = \dot{m}_{chw} \cdot c_{p,w} \cdot \Delta T_{chw} = 0.26 \times 4186 \times 6.5 \approx 7079$ W, in close agreement with the directly simulated value of 7031 W. The converging trajectory of $T_{chw,out}$ is smooth and well-damped, with no overshoot, demonstrating that the evaporator model responds stably to the gradual build-up of refrigerant mass and the associated increase in evaporating pressure during the warm-up phase.

6.1.4 Steady-State Operating Point

The complete set of steady-state values obtained at $t = 35000$ s is summarised in Table 7. The overall energy balance at steady state gives $\dot{Q}_{gen} + \dot{Q}_{eva} = 9788 + 7031 = 16819$ W on the heat input side and $\dot{Q}_{con} + \dot{Q}_{abs} = 7370 + 9574 = 16944$ W on the heat rejection side, a closure error of 0.74%. This discrepancy is within the expected numerical integration tolerance of the variable-step ode23tb solver and confirms the thermodynamic self-consistency of the model.

Table 7 - Nominal baseline steady-state simulation results at t=35000 s

Symbol	Description	Value
$T_{hw,out}$	Hot water outlet temperature	360.7 K
$T_{cw,out(abs)}$	Cooling water outlet — absorber	308.5 K
$T_{cw,out(con)}$	Cooling water outlet — condenser	311.2 K
$T_{chw,out}$	Chilled water outlet temperature	281.5 K (8.35 °C)
M_{gen}	Generator solution mass	19.22 kg
M_{con}	Condenser refrigerant mass	3.48 kg
M_{eva}	Evaporator refrigerant mass	7.31 kg
M_{abs}	Absorber solution mass	37.49 kg
X_{strong}	Strong solution concentration	59.61 wt%
X_{weak}	Weak solution concentration	56.13 wt%
P_{gen}	High-side pressure	7086 Pa
P_{low}	Low-side pressure	1009 Pa
T_{gen}(K)	Temperature in the generator.	356.6 K
T_{con}(K)	Temperature in the condenser.	312.4 K
T_{eva}(K)	Temperature in the evaporator.	280.3 K
T_{abs}(K)	Temperature in the absorber.	312.2 K
$\dot{Q}_{gen}$	Generator heat input	9788 W
$\dot{Q}_{con}$	Condenser heat rejection	7370 W
$\dot{Q}_{eva}$	Evaporator cooling capacity	7031 W
$\dot{Q}_{abs}$	Absorber heat rejection	9574 W
COP	Coefficient of performance	0.718

6.2 Step-Change Response: $T_{hw,i}$ — Scenarios 1 & 2

The hot water inlet temperature $T_{hw,i}$ is the primary driver of the absorption cycle — it governs the rate of refrigerant desorption in the generator and therefore directly controls the cooling capacity and COP of the chiller. Two scenarios are examined: Scenario 1, in which $T_{hw,i}$ is stepped down from 368 K to 363 K at $t = 20000$ s, and Scenario 2, in which $T_{hw,i}$ is stepped up from 368 K to 373 K at the same instant. All other inputs remain at their nominal values throughout. Both simulations are run for 50000 s, with the step change applied at $t = 20000$ s.

6.2.1 Scenario 1 — Step-Down to 363 K

6.2.1.1 Outlet Temperature Response

At $t = 20000$ s, $T_{hw,out}$ drops immediately and sharply from its nominal steady-state value of 360.7 K to approximately 356.7 K, before settling at 356.5 K. This instantaneous response reflects the purely algebraic nature of the outlet temperature expression — as $T_{hw,i}$ drops, the

log-mean temperature difference driving $\dot{Q}_{gen}$ reduces immediately with no thermal inertia in the hot water stream itself. The cooling water outlet at the condenser $T_{cw,out(con)}$ drops sharply from 311.2 K to approximately 310.3 K at the step, exhibiting a brief undershoot before settling at 310.6 K. This transient dip is caused by the sudden reduction in refrigerant vapour generation rate, which temporarily lowers the condenser heat load.

Figure 15 presents the outlet temperature responses following the step-down to $T_{hw,i} =$ 363 K.

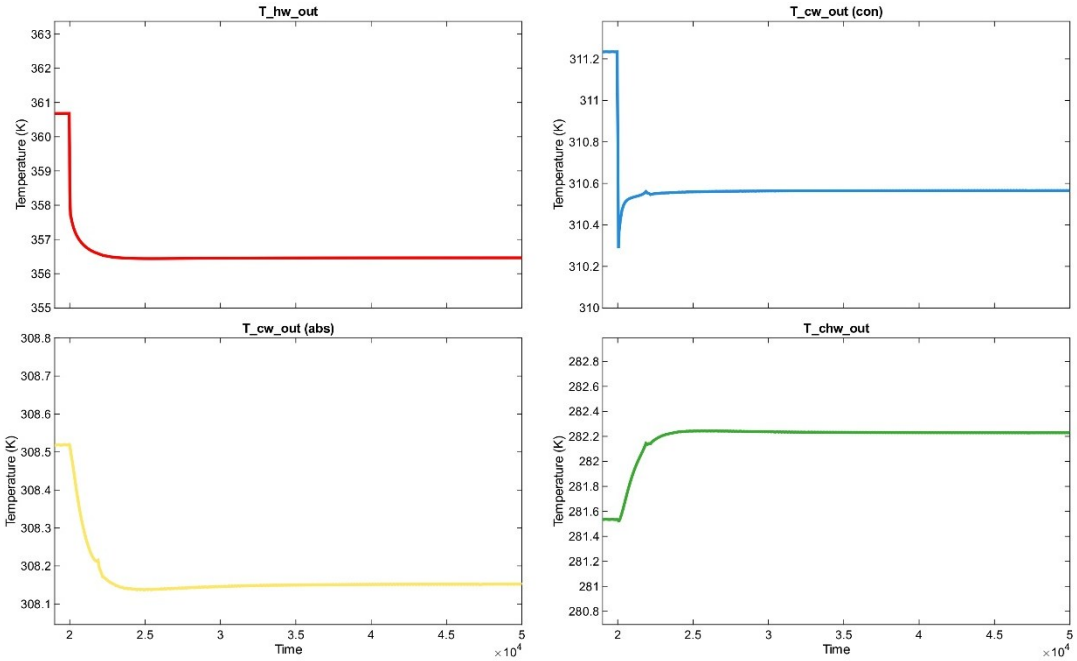

Figure 15: Outlet temperature responses $T_{hw,out}$, $T_{cw,out(con)}$, $T_{cw,out(abs)}$, and $T_{chw,out}$ following a step-down in $T_{hw,i}$ from 368 K to 363 K at $t = 20000$ s.

The cooling water outlet at the absorber $T_{cw,out(abs)}$ decreases smoothly from 308.5 K and settles at 308.2 K, a modest change consistent with the reduced strong solution flow returning from the generator carrying less thermal energy. The chilled water outlet temperature $T_{chw,out}$ rises from its nominal 281.5 K to 282.2 K following the step, indicating a reduction in evaporator cooling capacity as less refrigerant is available for evaporation. The rise in $T_{chw,out}$ is the most operationally significant consequence of the step-down, as it directly represents degraded chilling performance.

6.2.1.2 Concentration Response

As seen from figure 16, both concentrations decrease following the step change. The strong solution concentration X_{strong} drops from 59.61 wt% and converges to 58.3 wt%, while the weak solution concentration X_{weak} falls from 56.13 wt% to 55.25 wt%. The physical explanation is straightforward: with lower hot water temperature, the generator produces less refrigerant vapour per unit time, meaning less water is removed from the solution.

Figure 16 presents the evolution of X_{strong} and X_{weak} following the step-down.

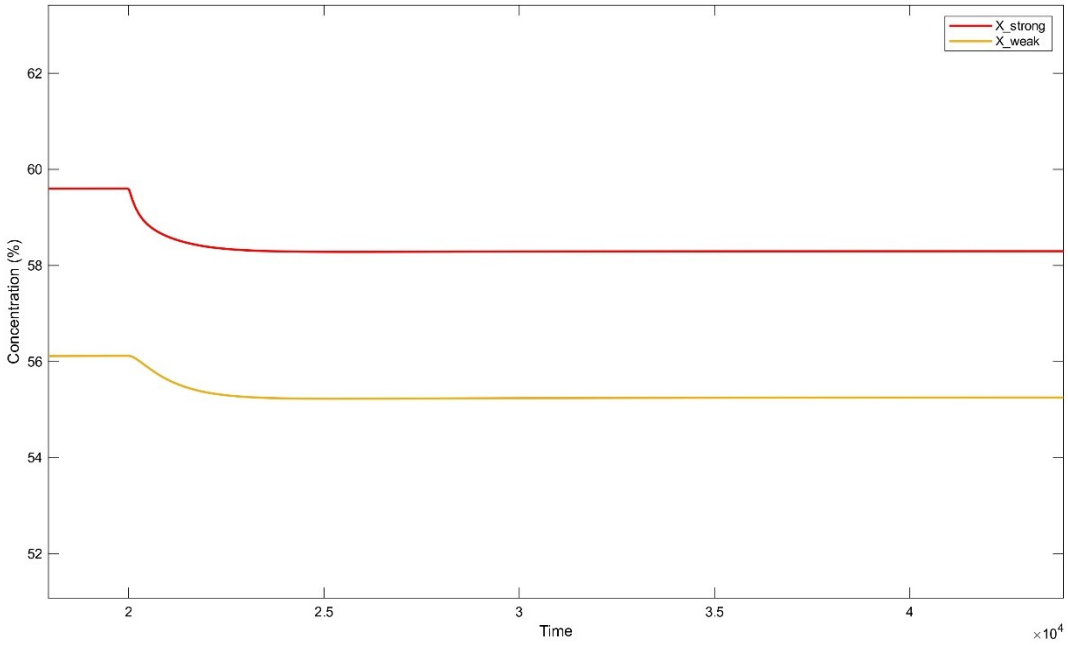

Figure 16: Solution concentration responses X_{strong} and X_{weak} following a step-down in $T_{hw,i}$ from 368 K to 363 K at $t = 20000\ s$

As a result, the LiBr solution leaving the generator is less concentrated — X_{strong} decreases — and correspondingly the absorber receives a weaker strong solution, reducing its absorption driving force and lowering X_{weak}. The concentration difference narrows marginally from $\Delta X = 3.48$ wt% to $\Delta X = 3.05$ wt%, consistent with the observed reduction in $\dot{Q}_{eva}$. Both concentrations converge smoothly within approximately 15000 s of the step change, demonstrating the stability of the species conservation equations under this perturbation.

6.2.1.3 Mass Distribution Response

As seen from figure 17, following the step change, M_{gen} increases from 19.22 kg and converges to 24.17 kg. This accumulation occurs because the reduced desorption rate lowers the outflow of strong solution from the generator — less vapour is generated to drive solution

circulation — allowing solution mass to build up in the generator sump. Correspondingly, M_{abs} decreases from 37.49 kg to 33.32 kg as less weak solution returns from the absorber to the generator.

Figure 17 presents the mass redistribution following the step-down.

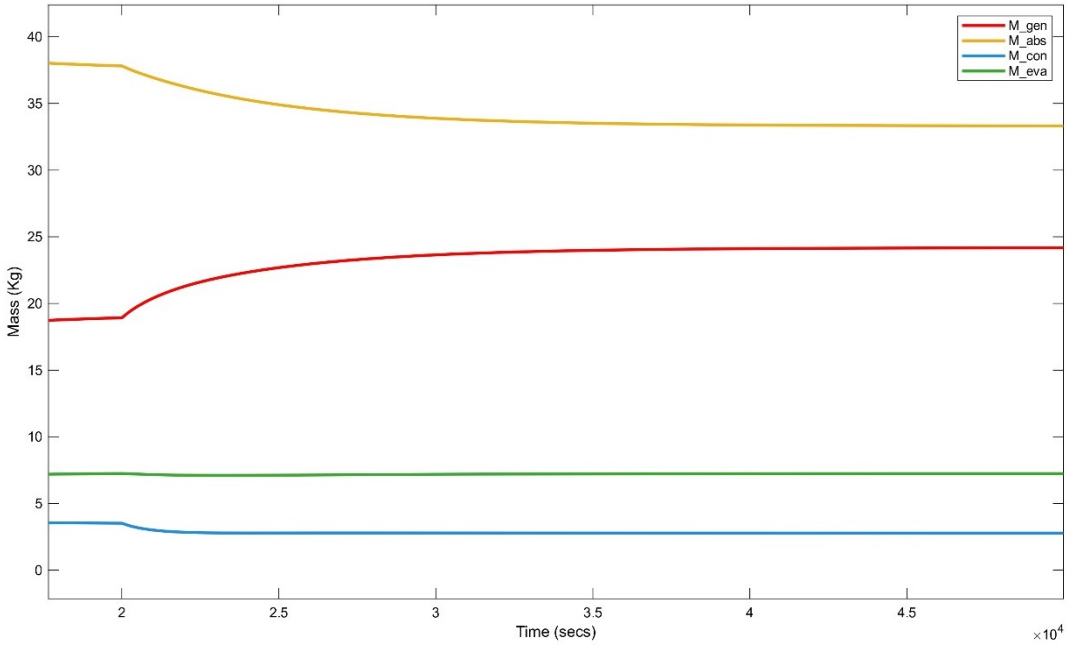

Figure 17: Component mass responses M_{gen}, M_{abs}, M_{con}, and M_{eva} following a step-down in $T_{hw,i}$ from 368 K to 363 K at $t = 20000$ s.

The condenser mass M_{con} decreases from 3.48 kg to 2.77 kg, consistent with the reduced refrigerant vapour production rate. The evaporator mass M_{eva} remains relatively stable at approximately 7.24 kg, indicating that the refrigerant inventory in the evaporator is largely insensitive to this level of hot-side perturbation. The total mass $M_{gen} + M_{abs} + M_{con} + M_{eva} = 24.17 + 33.32 + 2.77 + 7.24 = 67.50$ kg confirms that mass conservation is maintained at the new steady state.

6.2.2 Scenario 2 — Step-Up to 373 K

6.2.2.1 Outlet Temperature Response

The response to the step-up is directionally opposite and of comparable magnitude to Scenario 1, but exhibits subtly asymmetric dynamics due to the nonlinearity of the system. The hot water outlet $T_{hw,out}$ rises sharply from 360.7 K to approximately 364.7 K at the step moment, before settling at 364.9 K. The condenser cooling water outlet $T_{cw,out(con)}$ shows a brief spike upward

to approximately 312.1 K immediately after the step — caused by the sudden surge in refrigerant vapour generation and the corresponding increase in condenser heat load — before settling at 311.9 K. This transient overshoot in $T_{cw,out(con)}$ is the mirror image of the undershoot observed in Scenario 1 and confirms the nonlinear coupling between the generator desorption rate and the condenser heat rejection. The absorber cooling water outlet $T_{cw,out(abs)}$ rises from 308.5 K and settles at 308.9 K, consistent with the increased heat of absorption driven by the higher refrigerant vapour flux returning to the absorber. Most importantly, $T_{chw,out}$ decreases from 281.5 K to 280.8 K following the step, representing an improvement in chilling performance as the enhanced refrigerant production increases the evaporator heat load.

Figure 18 presents the outlet temperature responses following the step-up to $T_{hw,i} = 373$ K.

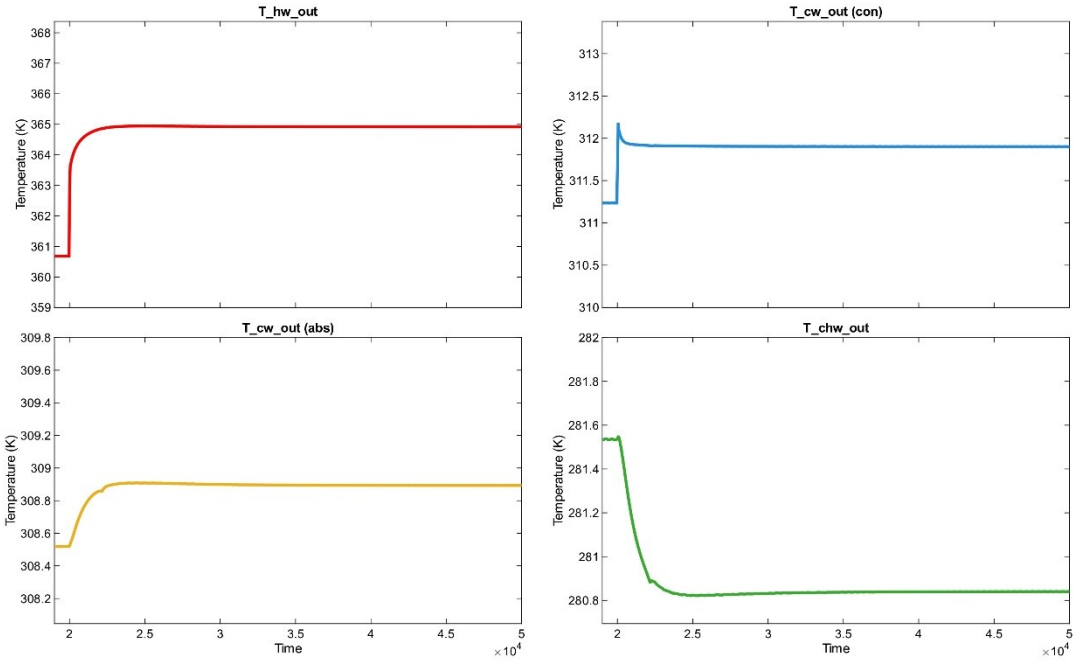

Figure 18: Outlet temperature responses $T_{hw,out}$, $T_{cw,out(con)}$, $T_{cw,out(abs)}$, and $T_{chw,out}$ following a step-up in $T_{hw,i}$ from 368 K to 373 K at $t = 20000$ s

6.2.2.2 Concentration Response

Both concentrations increase following the step-up, as expected from the inverse trend relative to Scenario 1. The strong solution concentration X_{strong} rises from 59.61 wt% to 60.9 wt%, and the weak solution concentration X_{weak} rises from 56.13 wt% to 56.98 wt%. The higher generator temperature drives more intense desorption, removing more water from the solution and producing a more concentrated strong solution leaving the generator. The concentration difference widens to $\Delta X = 3.92$ wt%, reflecting an enhanced absorption driving force in the

absorber and a correspondingly greater refrigerant circulation rate. The transient following the step-up settles within approximately 10000–12000 s, slightly faster than the 15000 s settling observed in Scenario 1, which is consistent with the general tendency of thermally driven systems to respond more quickly to energy additions than to energy reductions.

Figure 19 presents the concentration evolution following the step-up.

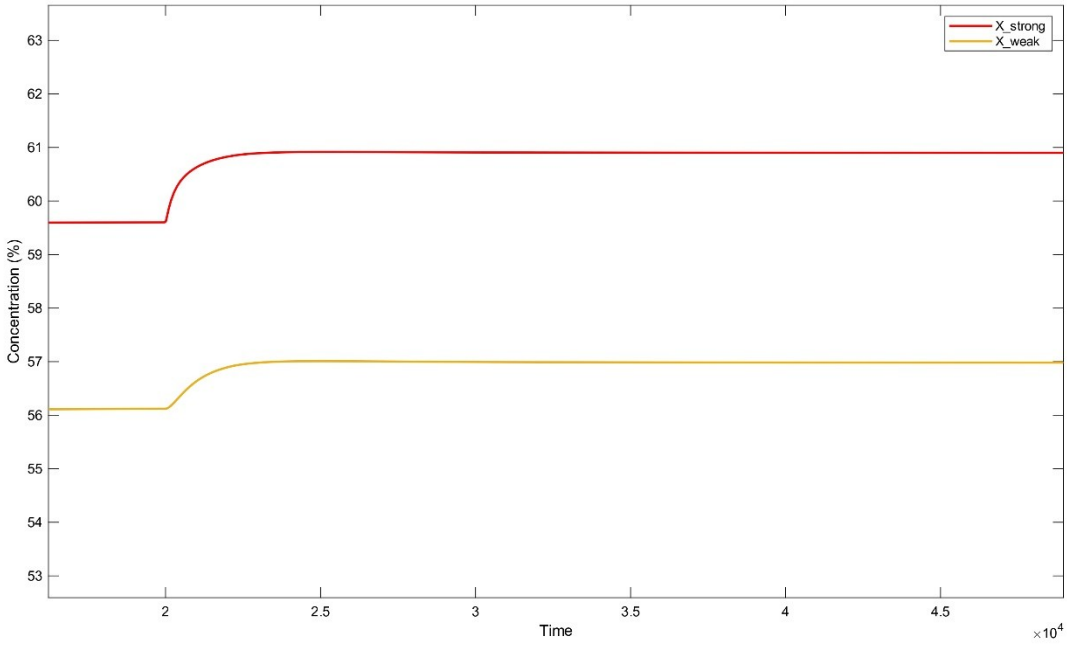

Figure 19: Solution concentration responses X_{strong} and X_{weak} following a step-up in $T_{hw,i}$ from 368 K to 373 K at $t = 20000$ s.

6.2.2.3 Mass Distribution Response

The generator mass M_{gen} decreases from 19.22 kg to 14.26 kg following the step-up, as the enhanced desorption rate drives more solution out of the generator and into the absorber via the SHX. The absorber mass M_{abs} correspondingly increases from 37.49 kg to 41.79 kg, absorbing the additional solution flow. The condenser mass M_{con} increases from 3.48 kg to 4.21 kg, consistent with the higher refrigerant condensation rate sustained by the increased vapour production. The evaporator mass M_{eva} remains nearly constant at 7.24 kg, again confirming that the evaporator refrigerant inventory responds only weakly to hot-side perturbations of this magnitude. The total mass is conserved: $14.26 + 41.79 + 4.21 + 7.24 = 67.50$ kg.

Figure 20 presents the mass redistribution following the step-up.

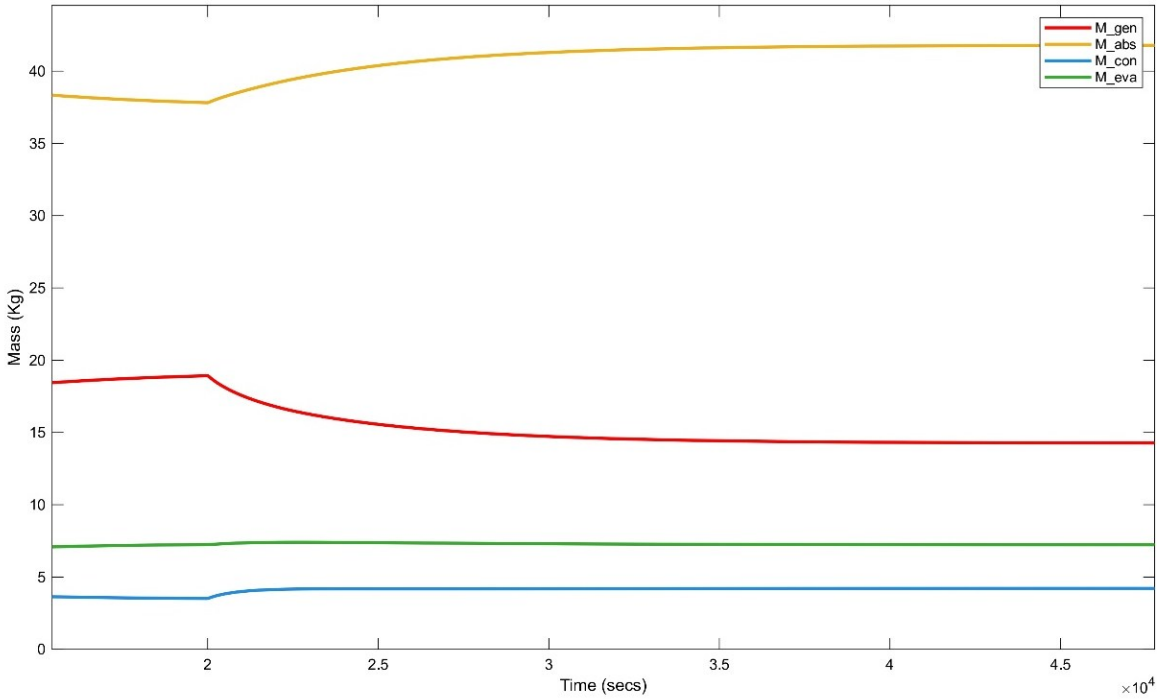

Figure 20: Component mass responses M_{gen}, M_{abs}, M_{con}, and M_{eva} following a step-up in $T_{hw,i}$ from 368 K to 373 K at $t =$ 20000 s.

6.2.3 Comparative Analysis

The results reveal a strong and consistent sensitivity of the chiller to hot water inlet temperature. A ±5 K step change in $T_{hw,i}$ produces a change in $\dot{Q}_{eva}$ of approximately ±750 W (roughly ±11%), while the COP remains remarkably stable at 0.716–0.719 across all three operating points.

This near-invariance of COP with $T_{hw,i}$ is characteristic of single-effect LiBr/H₂O chillers operating within their design range: both $\dot{Q}_{eva}$ and $\dot{Q}_{gen}$ scale proportionally with the driving temperature difference, so their ratio changes only marginally. The most pronounced mass shift occurs in M_{gen}, which changes by +26% (363 K) and −26% (373 K) relative to nominal — a direct consequence of the inverse relationship between generator temperature and solution residence time. The evaporator mass M_{eva} is the least sensitive variable across both scenarios, confirming that the refrigerant side of the low-pressure circuit is largely decoupled from hot-side perturbations of this magnitude.

Table 8 presents a side-by-side comparison of the new steady-state values for both scenarios against the nominal baseline.

Table 8 - Steady-state comparison — hot water inlet temperature step changes

Parameter	Nominal (368 K)	Scenario 1 (363 K)	Scenario 2 (373 K)
$T_{hw,out}$(K)	360.7	356.5	364.9
$T_{cw,out(abs)}$(K)	308.5	308.2	308.9
$T_{cw,out(con)}$(K)	311.2	310.6	311.9
$T_{chw,out}$(K)	281.5	282.2	280.8
X_{strong}(wt%)	59.61	58.30	60.90
X_{weak}(wt%)	56.13	55.25	56.98
ΔX(wt%)	3.48	3.05	3.92
M_{gen}(kg)	19.22	24.17	14.26
M_{abs}(kg)	37.49	33.32	41.79
M_{con}(kg)	3.48	2.77	4.21
M_{eva}(kg)	7.31	7.24	7.24
$\dot{Q}_{gen}$(W)	9788	8753	10819
$\dot{Q}_{eva}$(W)	7031	6272	7781
$\dot{Q}_{con}$(W)	7370	6558	8173
$\dot{Q}_{abs}$(W)	9574	8563	10577
COP	0.718	0.716	0.719

6.3 Step-Change Response: $T_{clw,i}$ — Scenarios 3 & 4

The inlet cooling water temperature $T_{clw,i}$ is the primary heat sink driver of the absorption cycle — it governs the rate of heat rejection in both the condenser and absorber simultaneously and therefore exerts a strong influence on the high-pressure side equilibrium, refrigerant condensation, and the low-pressure side absorption driving force. Two scenarios are examined: Scenario 3, in which $T_{clw,i}$ is stepped up from 305 K to 309 K at $t = 20000$ s, and Scenario 4, in which $T_{clw,i}$ is stepped down from 305 K to 301 K at the same instant. All other inputs remain at their nominal values throughout. Both simulations are run for 50000 s, with the step change applied at $t = 20000$ s.

6.3.1 Scenario 3 — Step-Up to 309 K

6.3.1.1 Outlet Temperature Response

At $t = 20000$ s, $T_{cw,out(con)}$ exhibits a sharp and distinctive transient: it first drops briefly to approximately 311.1 K — below its nominal 311.2 K — before rising steeply and settling at 314 K. This momentary undershoot is caused by the sudden increase in cooling water inlet

temperature reducing the effective condensation driving force instantaneously, before the system re-equilibrates at a higher condenser operating pressure that elevates $T_{cw,out(con)}$ well above its previous steady state.

Figure 21 presents the outlet temperature responses following the step-up to $T_{clw,i} = 309$ K.

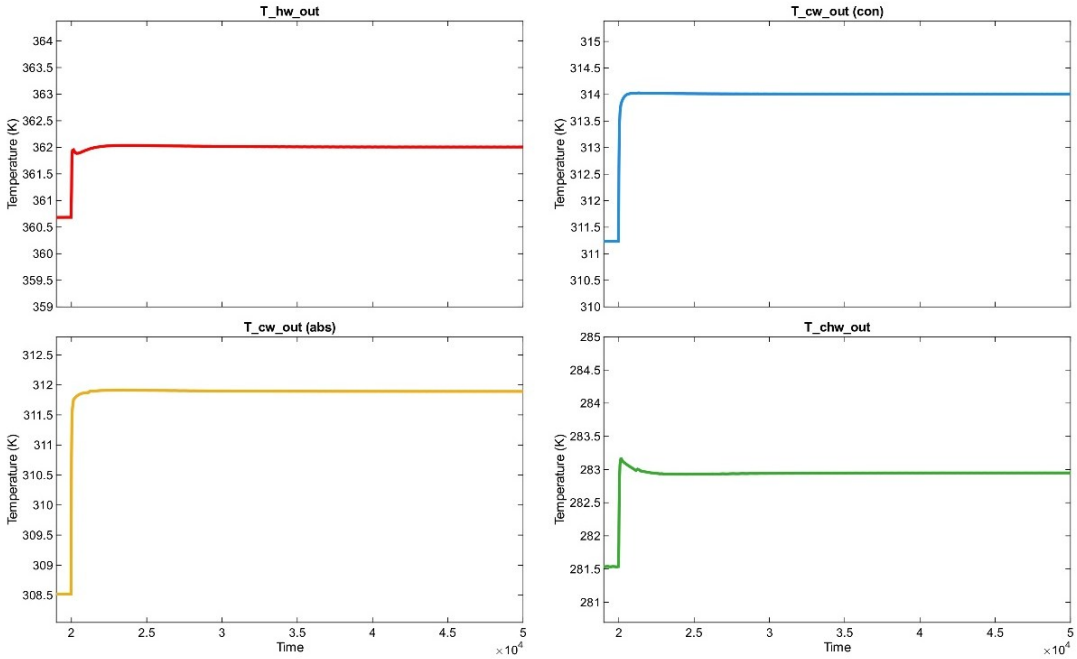

Figure 21: Outlet temperature responses $T_{hw,out}$, $T_{cw,out(con)}$, $T_{cw,out(abs)}$, and $T_{chw,out}$ following a step-up in $T_{clw,i}$ from 305 K to 309 K at $t = 20000$ s

The absorber cooling water outlet $T_{cw,out(abs)}$ rises sharply from 308.5 K and settles at 311.9 K, a change of +3.4 K that reflects the substantially elevated heat of absorption load as the warmer heat sink reduces absorption efficiency and forces the absorber to operate at a higher temperature equilibrium. The hot water outlet $T_{hw,out}$ rises from 360.7 K to 362 K, a physically consistent result explained by the elevated condenser back-pressure: as the high-pressure side equilibrium shifts upward, the generator must operate at a higher temperature, which reduces the log-mean temperature difference available to the hot water stream and causes $T_{hw,out}$ to rise. Most critically, $T_{chw,out}$ exhibits a sharp overshoot spike to approximately 283 K immediately after the step before settling at 282.9 K, confirming the degradation in chilling performance as the evaporator equilibrates with a higher absorber pressure at reduced refrigerant throughput.

6.3.1.2 Concentration Response

Both concentrations respond rapidly and settle within approximately 2000–3000 s of the step change — notably faster than the 10000–15000 s settling times observed in Scenarios 1 and 2.

Figure 22 presents the evolution of X_{strong} and X_{weak} following the step-up.

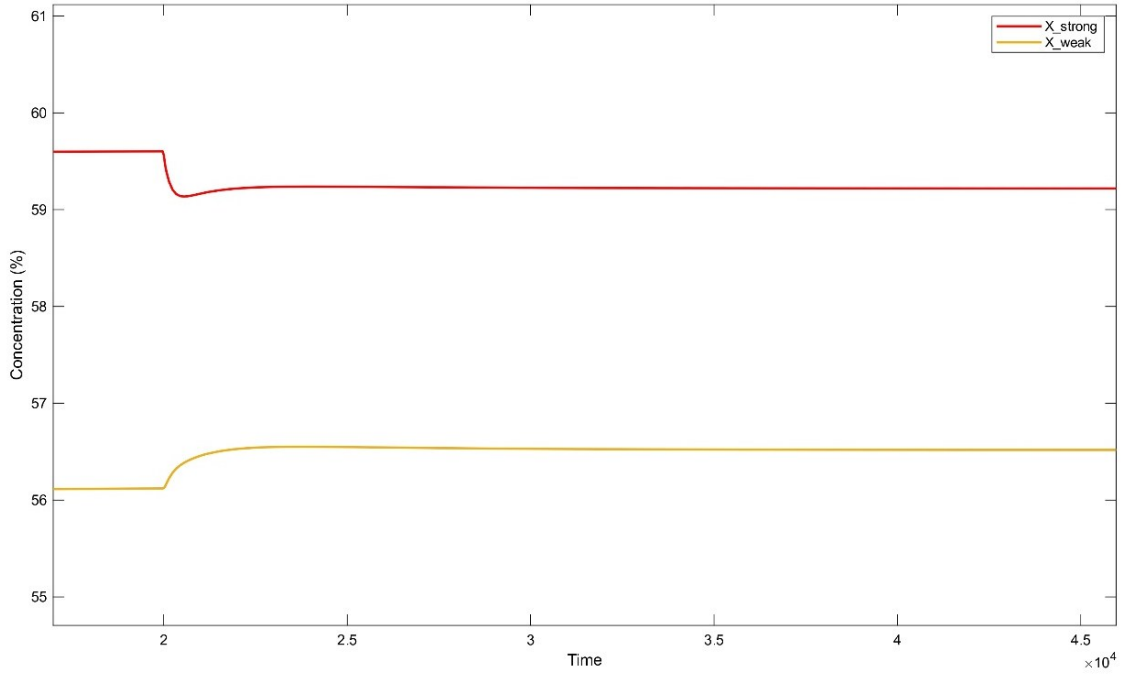

Figure 22: Solution concentration responses X_{strong} and X_{weak} following a step-up in $T_{clw,i}$ from 305 K to 309 K at $t =$ 20000 s.

The strong solution concentration X_{strong} decreases from 59.61 wt% to 59.22 wt%, while the weak solution concentration X_{weak} rises from 56.13 wt% to 56.52 wt%. The physical mechanism is as follows: the warmer cooling water reduces the absorber's capacity to absorb refrigerant vapour — absorption is an exothermic process whose driving force diminishes as the heat sink temperature rises. As a result, the absorber solution retains more water (higher X_{weak}), and since the generator receives this weaker incoming solution, it produces a less concentrated strong solution leaving via the SHX (lower X_{strong}). The concentration difference narrows from $\Delta X = 3.48$ wt% to $\Delta X = 2.70$ wt%, indicating a reduced refrigerant circulation rate and directly explaining the observed rise in $T_{chw,out}$.

6.3.1.3 Mass Distribution Response

Figure 23 presents the component mass redistribution following the step-up.

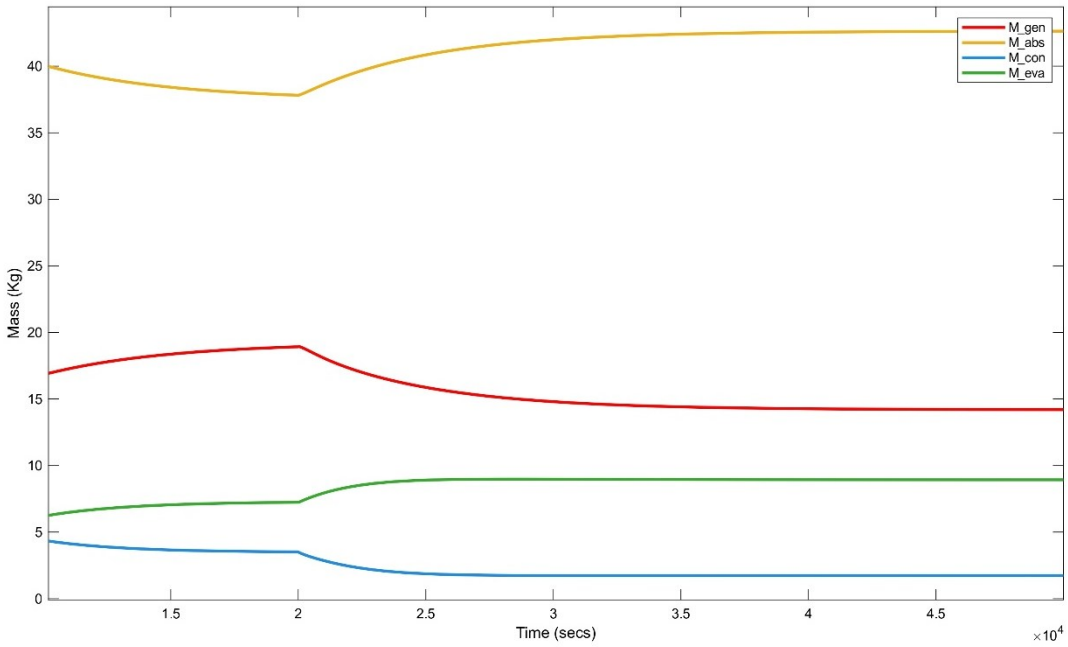

Figure 23: Component mass responses M_{gen}, M_{abs}, M_{con}, and M_{eva} following a step-up in $T_{clw,i}$ from 305 K to 309 K at $t = 20000$ s.

The generator mass M_{gen} decreases from 19.22 kg to 14.2 kg following the step. This depletion occurs because the elevated condenser back-pressure demands a sustained increase in desorption rate to maintain the high-pressure side equilibrium, driving solution out of the generator sump at a higher rate than it is replenished. The absorber mass M_{abs} rises correspondingly from 37.49 kg to 42.63 kg as solution accumulates in the absorber where the reduced absorption driving force slows solution uptake and increases residence time. The condenser mass M_{con} drops steeply and continuously from 3.48 kg to 1.739 kg — the most dramatic single-variable change in this scenario — because the elevated condensation temperature and pressure reduce condensate formation and slow the rate of liquid refrigerant draining into the condenser sump. The evaporator mass M_{eva} increases from 7.31 kg to 8.936 kg as the reduced absorption rate in the absorber draws refrigerant vapour from the evaporator more slowly, allowing refrigerant to accumulate on the low-pressure side. Mass conservation is confirmed: $14.2 + 42.63 + 1.739 + 8.936 = 67.51$ kg.

6.3.2 Scenario 4 — Step-Down to 301 K

6.3.2.1 Outlet Temperature Response

Figure 24 presents the outlet temperature responses following the step-down to $T_{clw,i} =$ 301 K.

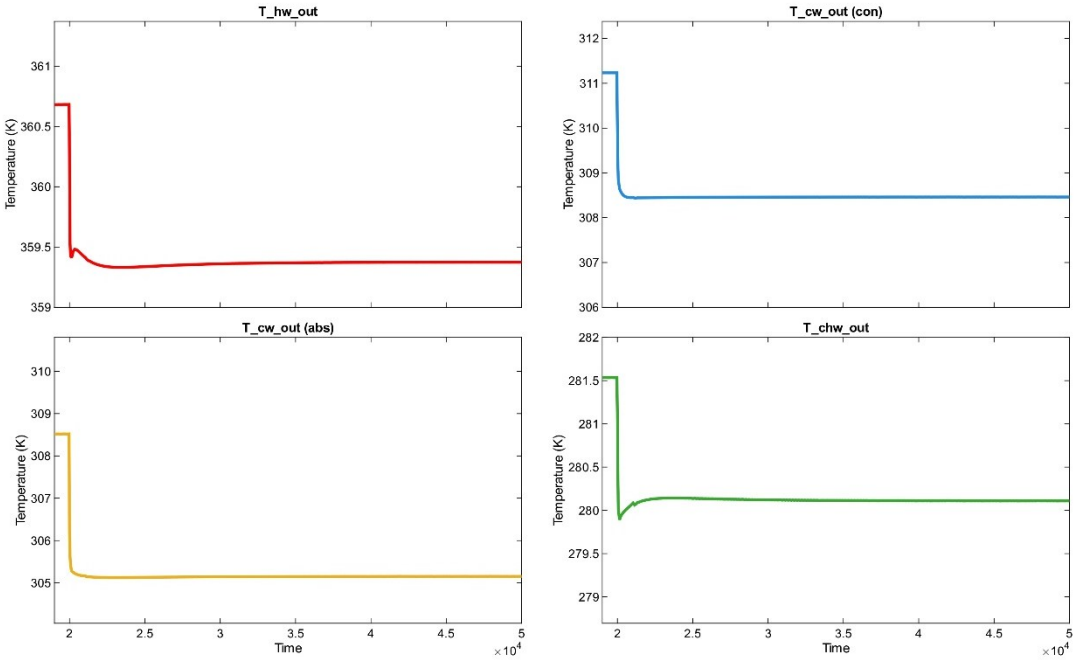

Figure 24: Outlet temperature responses $T_{hw,out}$, $T_{cw,out(con)}$, $T_{cw,out(abs)}$, and $T_{chw,out}$ following a step-down in $T_{clw,i}$ from 305 K to 301 K at $t = 20000$ s.

The step-down produces sharp, well-defined responses in all four outlet temperatures, with settling behaviour that mirrors Scenario 3 in direction but exhibits qualitatively different transient characteristics. The condenser cooling water outlet $T_{cw,out(con)}$ drops immediately from 311.2 K, passing through a brief overshoot above 311 K at the moment of the step before descending sharply to its new steady state of 308.5 K — a symmetric counterpart to the undershoot-then-rise observed in Scenario 3. The absorber cooling water outlet $T_{cw,out(abs)}$ falls sharply from 308.5 K and settles at 305.2 K, a decrease of −3.3 K consistent with the enhanced heat rejection capacity of the colder cooling stream at both heat exchangers simultaneously. The hot water outlet $T_{hw,out}$ falls from 360.7 K and shows a brief undershoot to approximately 359.5 K before settling at 359.4 K — the undershoot being caused by the momentary over-enhancement of the log-mean temperature difference as the high-pressure equilibrium rapidly adjusts to lower condenser pressure. Most importantly, $T_{chw,out}$ drops sharply to approximately 279.8 K immediately following the step, before recovering slightly and stabilising at 280.1 K, representing a significant improvement

of −1.4 K relative to the nominal steady state and confirming the enhanced evaporator performance driven by the deeper low-pressure equilibrium.

6.3.2.2 Concentration Response

Figure 25 presents the evolution of X_{strong} and X_{weak} following the step-down.

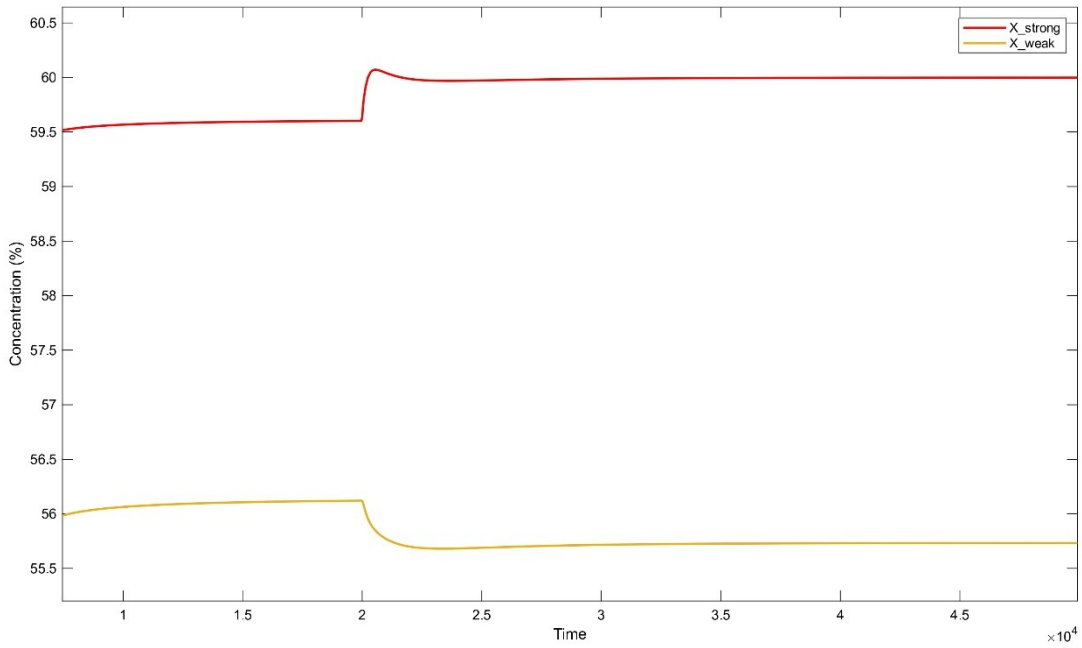

Figure 25: Solution concentration responses X_{strong} and X_{weak} following a step-down in $T_{clw,i}$ from 305 K to 301 K at $t =$ 20000 s.

Both concentrations shift in the direction opposite to Scenario 3. The strong solution concentration X_{strong} rises from 59.61 wt% and overshoots momentarily to approximately 60.05 wt% immediately after the step before settling at 60.0 wt%, while X_{weak} drops from 56.13 wt% and settles at 55.73 wt%. The colder cooling water at the absorber removes the heat of absorption more effectively, enabling the absorber to uptake more refrigerant vapour per unit time and producing a more dilute (water-rich) weak solution leaving the absorber — expressed as a lower X_{weak}. The generator consequently receives this weaker incoming solution and drives it to a higher final LiBr concentration, raising X_{strong}. Notably, the overshoot in X_{strong} visible at $t = 20000$ s reflects a brief intensification of the generator desorption rate as the pressure differential between high and low sides transiently widens before the new equilibrium is fully established. The concentration difference widens to $\Delta X =$ 4.27 wt%, the largest of all four scenarios, confirming that the cooling water temperature is a highly effective lever for enhancing the refrigerant circulation ratio.

6.3.2.3 Mass Distribution Response

Figure 26 presents the component mass redistribution following the step-down.

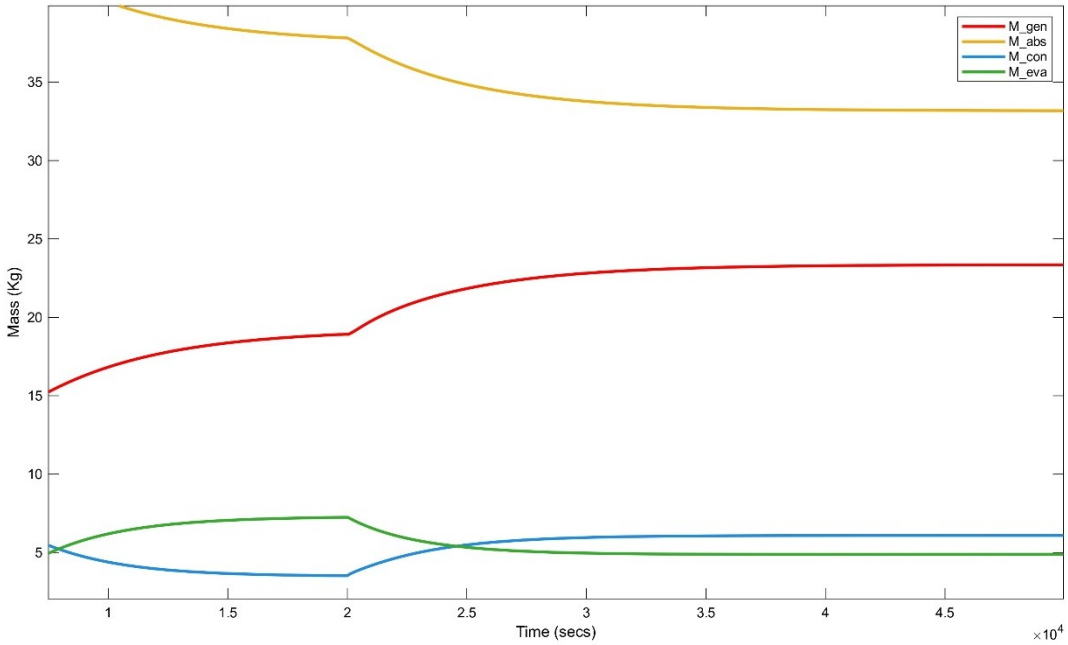

Figure 26: Component mass responses M_{gen}, M_{abs}, M_{con}, and M_{eva} following a step-down in $T_{clw,i}$ from 305 K to 301 K at $t = 20000$ s.

The mass redistribution in Scenario 4 is the most dynamically complex of all four scenarios, featuring a notable crossing behaviour between M_{con} and M_{eva} in the period immediately following the step change. Prior to $t = 20000$ s, M_{eva} (green) sits slightly above M_{con} (blue) at approximately 6.9 kg vs. 4.5 kg respectively. At the step, M_{con} rises rapidly as the colder cooling water drives intense condensation and rapid liquid refrigerant accumulation, while M_{eva} simultaneously drops as the enhanced absorption demand draws refrigerant vapour from the evaporator more aggressively. The two traces cross at approximately $t = 25000$ s, after which M_{con} stabilises at 6.087 kg and M_{eva} settles at 4.886 kg — a complete inversion of their pre-step relationship. The generator mass M_{gen} rises from 19.22 kg to 23.35 kg as the reduced condenser back-pressure slightly dampens the desorption driving force and allows modest solution accumulation in the generator. The absorber mass M_{abs} decreases from 37.49 kg to 33.18 kg as the enhanced absorption rate draws solution through the cycle more efficiently, reducing the absorber inventory. Mass conservation is confirmed: $23.35 + 33.18 + 6.087 + 4.886 = 67.50$ kg.

6.3.3 Comparative Analysis

Two findings of particular significance emerge from this comparison. First, unlike the $T_{hw,i}$ perturbations in Section 6.2 which left the COP nearly invariant at 0.716–0.719, changes in $T_{clw,i}$ produce a meaningful and asymmetric shift in COP — dropping to 0.684 (−4.7%) in Scenario 3 and rising to 0.742 (+3.3%) in Scenario 4.

Table 9 presents the steady-state values for both scenarios against the nominal baseline.

Table 9 - Steady-state comparison — cooling water inlet temperature step changes

Parameter	Nominal (305 K)	Scenario 3 (309 K)	Scenario 4 (301 K)
$T_{hw,out}$(K)	360.7	362.0	359.4
$T_{cw,out(abs)}$(K)	308.5	311.9	305.2
$T_{cw,out(con)}$(K)	311.2	314.0	308.5
$T_{chw,out}$(K)	281.5	282.9	280.1
X_{strong}(wt%)	59.61	59.22	60.00
X_{weak}(wt%)	56.13	56.52	55.73
ΔX(wt%)	3.48	2.70	4.27
M_{gen}(kg)	19.22	14.20	23.35
M_{abs}(kg)	37.49	42.63	33.18
M_{con}(kg)	3.48	1.739	6.087
M_{eva}(kg)	7.31	8.936	4.886
$\dot{Q}_{gen}$(W)	9788	8024	11549
$\dot{Q}_{eva}$(W)	7031	5491	8576
$\dot{Q}_{con}$(W)	7370	5755	8990
$\dot{Q}_{abs}$(W)	9574	7857	11284
COP	0.718	0.684	0.742

This asymmetry arises because a warmer heat sink simultaneously degrades absorption efficiency, raises condensation pressure, and reduces $\dot{Q}_{eva}$ relative to $\dot{Q}_{gen}$, whereas a cooler heat sink enhances all three effects in a compounding manner. Second, the condenser mass M_{con} is the most sensitive state variable to $T_{clw,i}$, varying by a factor of 3.5 between the two scenarios (from 1.739 kg to 6.087 kg), and exhibiting the distinctive crossing behaviour with M_{eva} in Scenario 4 that demonstrates the strong nonlinear coupling between refrigerant-side inventory redistribution and the heat sink temperature. These results collectively identify $T_{clw,i}$ as the dominant efficiency-controlling parameter among all inputs investigated and underscore the importance of maintaining low cooling water supply temperatures for optimal chiller operation.

6.4 Step-Change Response: $T_{chw,i}$ — Scenarios 5 & 6

The inlet chilled water temperature $T_{cw,i}$ sets the thermal load boundary condition at the evaporator — it defines the temperature of the building-side water returning to the chiller and therefore determines the temperature differential available for heat extraction in the evaporator. Two scenarios are examined: Scenario 5, in which $T_{cw,i}$ is stepped up from 288 K to 291 K at $t = 20000$ s, representing a warmer return from a higher building cooling load, and Scenario 6, in which $T_{cw,i}$ is stepped down from 288 K to 285 K at the same instant, representing a colder return from a reduced building load. All other inputs remain at their nominal values throughout. Both simulations are run for 50000 s, with the step change applied at $t = 20000$ s.

6.4.1 Scenario 5 — Step-Up to 291 K

6.4.1.1 Outlet Temperature Response

Figure 27 presents the outlet temperature responses following the step-up to $T_{cw,i} = 291$ K.

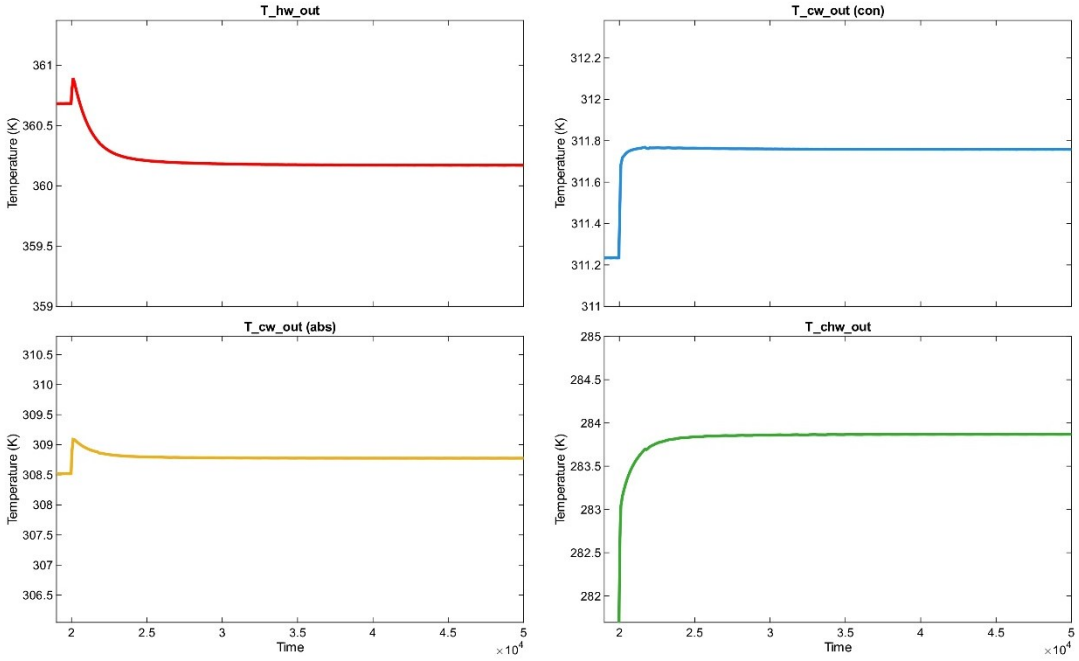

Figure 27: Outlet temperature responses $T_{hw,out}$, $T_{cw,out(con)}$, $T_{cw,out(abs)}$, and $T_{chw,out}$ following a step-up in $T_{cw,i}$ from 288 K to 291 K at $t = 20000$ s.

At $t = 20000$ s, $T_{hw,out}$ exhibits a sharp upward spike to approximately 361 K before dropping and settling at 360.2 K. This transient overshoot is caused by the sudden reduction in evaporator heat load as the chilled water inlet temperature rises — with a smaller temperature

differential available at the evaporator, less heat is extracted from the refrigerant, the low-pressure side equilibrium shifts upward, and a momentary reduction in desorption demand briefly reduces heat extraction from the hot water stream before the system re-equilibrates. The condenser cooling water outlet $T_{cw,out(con)}$ exhibits a brief undershoot to approximately 311.2 K at the step before rising and settling at 311.8 K, a transient fingerprint consistent with the momentary disruption to the refrigerant vapour generation rate before the new high-pressure equilibrium is established. The absorber cooling water outlet $T_{cw,out(abs)}$ shows a brief spike to 309 K immediately following the step before settling at 308.8 K, reflecting the transient surge in absorber heat load as the refrigerant circulation dynamics readjust. The chilled water outlet $T_{chw,out}$ rises sharply from 281.5 K, overshoots to approximately 284 K at the step instant, then settles at 283.9 K — a rise of +2.4 K relative to nominal, representing the most operationally significant consequence of the step-up as it directly indicates a degraded ability to meet the building cooling set-point.

6.4.1.2 Concentration Response

Figure 28 presents the evolution of X_{strong} and X_{weak} following the step-up.

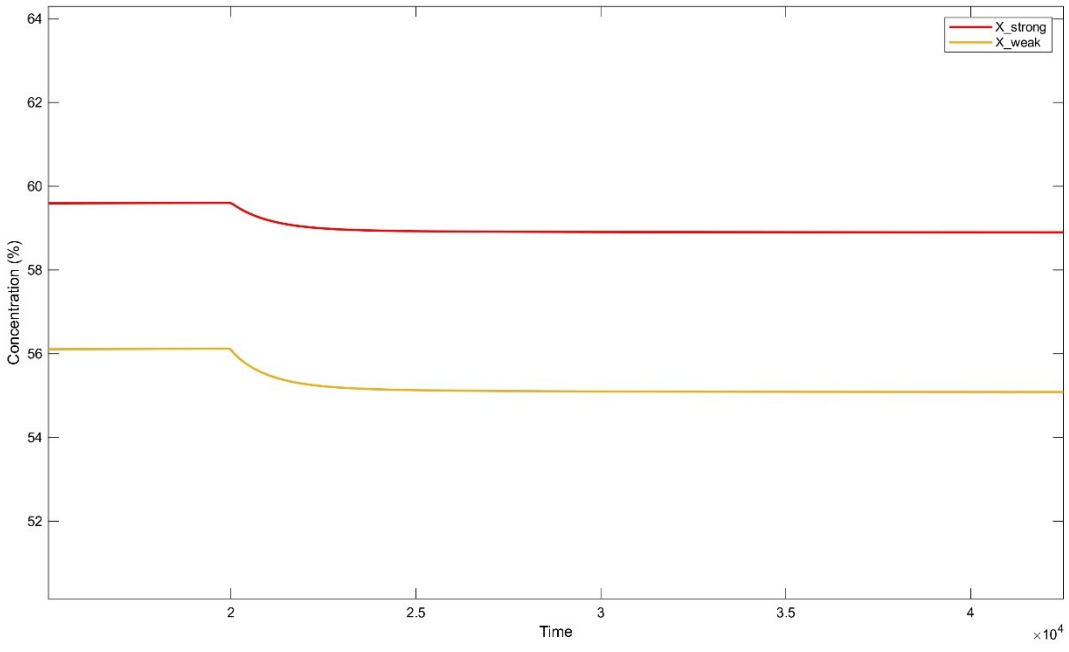

Figure 28: Solution concentration responses X_{strong} and X_{weak} following a step-up in $T_{cw,i}$ from 288 K to 291 K at $t = 20000$ s.

A notable and physically distinctive feature of this scenario is that both X_{strong} and X_{weak} decrease simultaneously following the step change, in contrast to the opposing directional responses observed in Scenarios 1–4. The strong solution

concentration X_{strong} falls from 59.61 wt% to 58.9 wt%, while the weak solution concentration X_{weak} also falls from 56.13 wt% to 55.09 wt%. The physical explanation is that the warmer chilled water return raises the evaporator saturation temperature and therefore the low-side pressure P_{low}, which reduces the vapour pressure driving force for absorption at the absorber. With the absorber receiving a lower-quality driving force, it absorbs refrigerant less efficiently and produces a weaker strong solution directed to the generator — lowering X_{strong}. Simultaneously, the higher low-side pressure reduces the tendency of the weak solution to release refrigerant in the generator, lowering the equilibrium LiBr concentration of the weak stream — reducing X_{weak}. The concentration difference narrows from $\Delta X = 3.48$ wt% to $\Delta X = 3.81$ wt%, indicating that despite both concentrations falling, the spread between strong and weak solutions widens slightly, which is consistent with the observed increase in all four heat transfer rates $\dot{Q}_{gen}$, $\dot{Q}_{eva}$, $\dot{Q}_{con}$, and $\dot{Q}_{abs}$ relative to the nominal condition.

6.4.1.3 Mass Distribution Response

Figure 29 presents the component mass redistribution following the step-up.

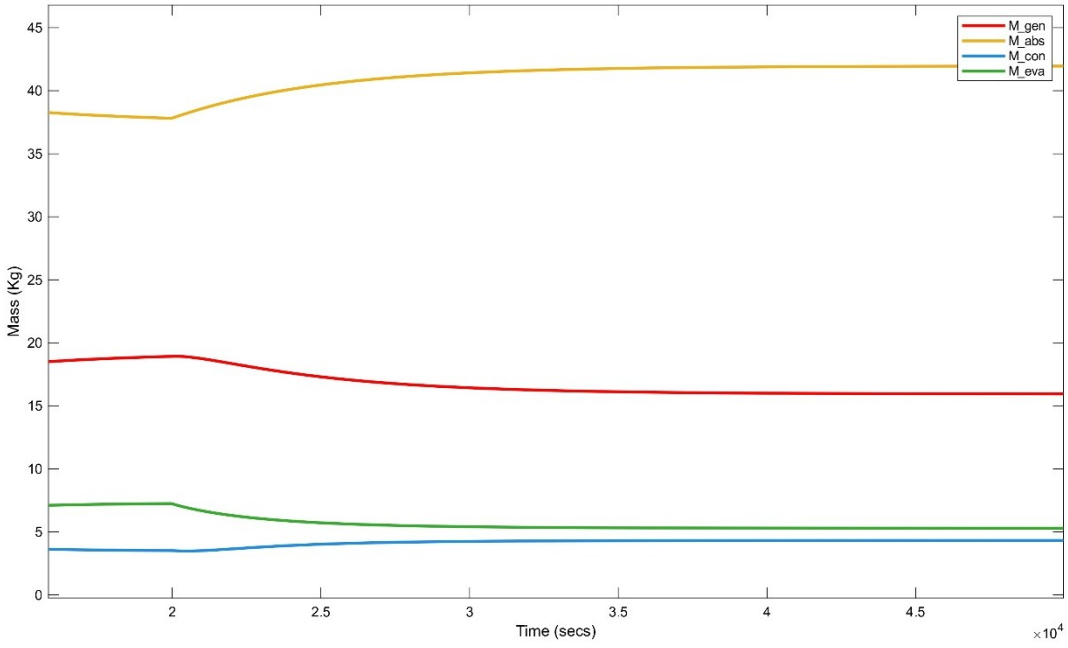

Figure 29: Component mass responses M_{gen}, M_{abs}, M_{con}, and M_{eva} following a step-up in $T_{cw,i}$ from 288 K to 291 K at $t = 20000$ s.

The generator mass M_{gen} decreases from 19.22 kg to 15.95 kg following the step, driven by the elevated low-side pressure which enhances the pressure differential across the expansion valve and accelerates solution circulation out of the generator. The absorber mass M_{abs} rises from 37.49 kg to 41.95 kg as the increased solution flow accumulates in the absorber, where

the reduced vapour pressure driving force slows absorption and increases the residence time of the incoming weak solution. The condenser mass M_{con} increases modestly from 3.48 kg to 4.318 kg, consistent with the slightly elevated refrigerant condensation rate as $\dot{Q}_{con}$ rises to 8102 W. The evaporator mass M_{eva} decreases from 7.31 kg to 5.287 kg, as the reduced temperature differential at the evaporator lowers the rate of refrigerant evaporation and the enhanced low-side pressure draws refrigerant more rapidly into the absorber, depleting the evaporator sump. Mass conservation is confirmed: $15.95 + 41.95 + 4.318 + 5.287 = 67.51$ kg.

6.4.2 Scenario 6 — Step-Down to 285 K

6.4.2.1 Outlet Temperature Response

Figure 30 presents the outlet temperature responses following the step-down to $T_{cw,i} = 285$ K.

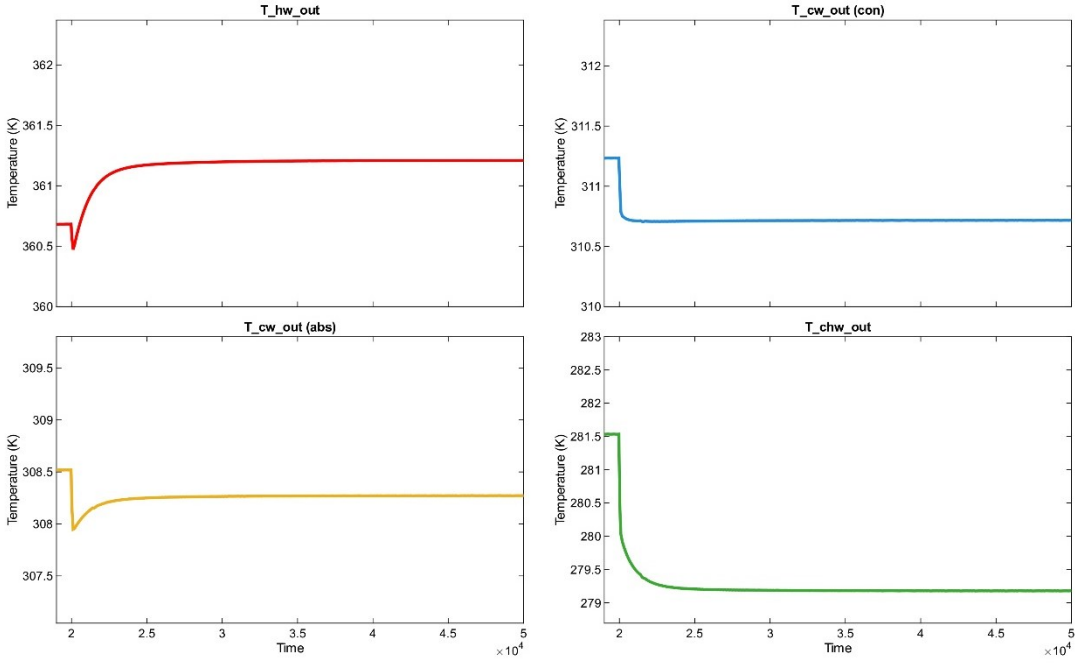

Figure 30: Outlet temperature responses $T_{hw,out}$, $T_{cw,out(con)}$, $T_{cw,out(abs)}$, and $T_{chw,out}$ following a step-down in $T_{cw,i}$ from 288 K to 285 K at $t = 20000$ s.

The step-down to $T_{cw,i} = 285$ K produces directionally opposite responses to Scenario 5 across all outlet temperatures. The hot water outlet $T_{hw,out}$ rises from 360.7 K and settles at 361.2 K — an increase of +0.5 K relative to nominal — as the deeper evaporator temperature differential increases the heat extraction demand on the generator side and slightly raises the equilibrium operating temperature of the high-pressure circuit. The condenser cooling water

outlet $T_{cw,out(con)}$ decreases from 311.2 K and settles at 310.7 K, and the absorber cooling water outlet $T_{cw,out(abs)}$ falls from 308.5 K to 308.3 K, both consistent with the reduced heat rejection load as the lower low-side pressure reduces refrigerant circulation intensity. Most importantly from an operational standpoint, $T_{chw,out}$ drops from 281.5 K to 279.2 K — a decrease of −2.3 K — representing a significant improvement in cooling depth as the evaporator operates at a lower saturation temperature driven by the enhanced temperature differential between the returning chilled water and the evaporating refrigerant.

6.4.2.2 Concentration Response

Figure 31 presents the evolution of X_{strong} and X_{weak} following the step-down.

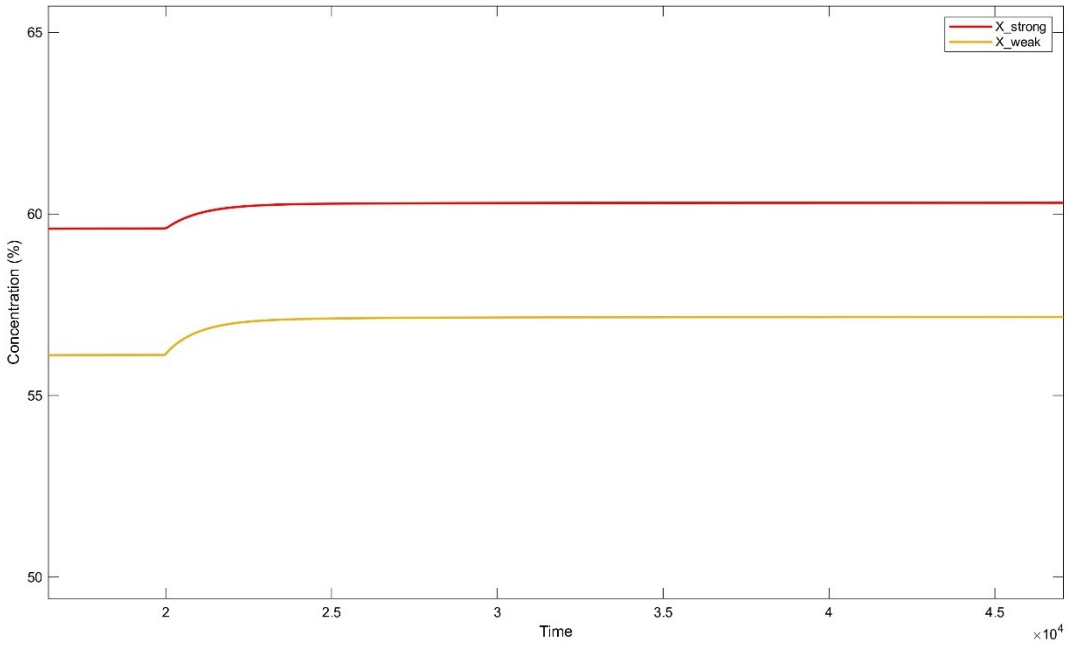

Figure 31: Solution concentration responses X_{strong} and X_{weak} following a step-down in $T_{cw,i}$ from 288 K to 285 K at $t = 20000\ s$

Mirroring the pattern of Scenario 5, both concentrations shift in the same direction following the step-down, with X_{strong} rising from 59.61 wt% to 60.31 wt% and X_{weak} rising from 56.13 wt% to 57.16 wt%. The physical basis is the inverse of Scenario 5: the lower chilled water inlet temperature reduces the evaporator saturation temperature and the low-side pressure P_{low}, which strengthens the vapour pressure driving force for absorption and enables the absorber to draw in refrigerant more effectively from the evaporator. The generator consequently receives a richer weak solution and drives it to a higher final LiBr concentration, raising both X_{strong} and X_{weak} simultaneously. The concentration difference narrows marginally

to $\Delta X = 3.15$ wt%, reflecting a slightly tighter operating band between strong and weak solution streams consistent with the reduced heat transfer rates $\dot{Q}_{gen} = 9091$ W, $\dot{Q}_{eva} = 6324$ W, and $\dot{Q}_{abs} = 8891$ W — all below the nominal values, confirming that the colder chilled water return actually reduces the total refrigerant throughput despite improving $T_{chw,out}$.

6.4.2.3 Mass Distribution Response

Figure 32 presents the component mass redistribution following the step-down.

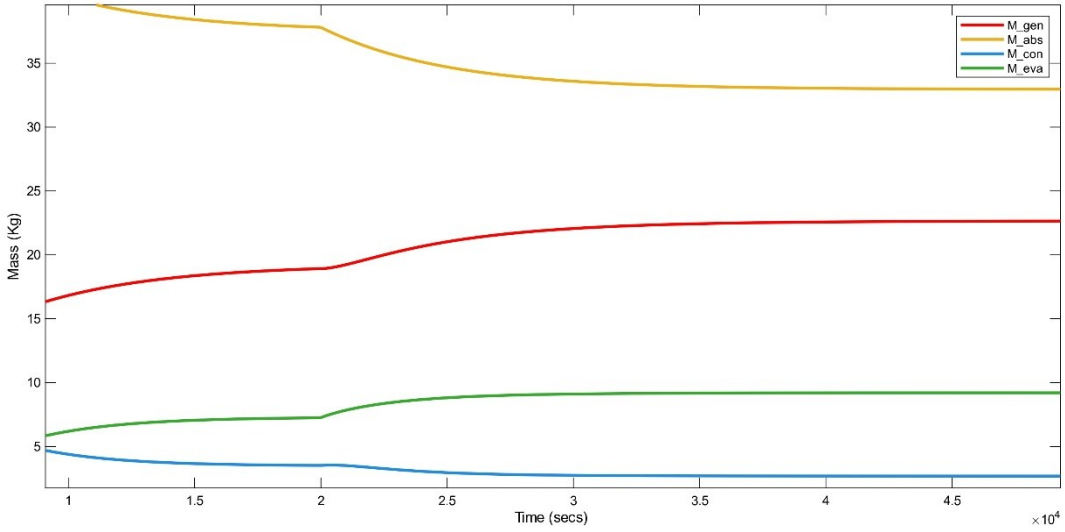

Figure 32: Component mass responses M_{gen}, M_{abs}, M_{con}, and M_{eva} following a step-down in $T_{cw,i}$ from 288 K to 285 K at $t = 20000$ s

The generator mass M_{gen} increases from 19.22 kg to 22.64 kg following the step, as the reduced low-side pressure dampens the circulation driving force and allows solution to accumulate in the generator sump at a higher steady-state level. The absorber mass M_{abs} decreases from 37.49 kg to 32.97 kg as the lower low-side pressure enhances the evaporator-to-absorber vapour flow, reducing the liquid inventory in the absorber. The condenser mass M_{con} decreases from 3.48 kg to 2.687 kg, reflecting the reduced refrigerant condensate production rate as $\dot{Q}_{con}$ falls to 6644 W. The evaporator mass M_{eva} increases substantially from 7.31 kg to 9.205 kg — the largest evaporator inventory of all six scenarios — as the colder chilled water inlet suppresses the evaporation rate at the lower saturation temperature, allowing refrigerant to pool in the evaporator sump before being drawn into the absorber. Mass conservation is confirmed: $22.64 + 32.97 + 2.687 + 9.205 = 67.50$ kg.

6.4.3 Comparative Analysis

The results reveal two physically counterintuitive findings that distinguish the chilled water inlet perturbation from the hot and cooling water scenarios examined previously. First, a warmer chilled water return (Scenario 5) actually improves the COP to 0.739 while simultaneously degrading $T_{chw,out}$ to 283.9 K — meaning the chiller becomes thermodynamically more efficient but operationally less useful from a cooling perspective.

Table 10 presents the steady-state values for both scenarios against the nominal baseline.

Table 10 - Steady-state comparison — chilled water inlet temperature step changes

Parameter	Nominal (288 K)	Scenario 5 (291 K)	Scenario 6 (285 K)
$T_{hw,out}$(K)	360.7	360.2	361.2
$T_{cw,out(abs)}$(K)	308.5	308.8	308.3
$T_{cw,out(con)}$(K)	311.2	311.8	310.7
$T_{chw,out}$(K)	281.5	283.9	279.2
X_{strong}(wt%)	59.61	58.90	60.31
X_{weak}(wt%)	56.13	55.09	57.16
ΔX(wt%)	3.48	3.81	3.15
M_{gen}(kg)	19.22	15.95	22.64
M_{abs}(kg)	37.49	41.95	32.97
M_{con}(kg)	3.48	4.318	2.687
M_{eva}(kg)	7.31	5.287	9.205
$\dot{Q}_{gen}$(W)	9788	10483	9091
$\dot{Q}_{eva}$(W)	7031	7748	6324
$\dot{Q}_{con}$(W)	7370	8102	6644
$\dot{Q}_{abs}$(W)	9574	10258	8891
COP	0.718	0.739	0.696

The elevated $T_{cw,i}$ raises P_{low}, which strengthens the absorption driving force sufficiently to increase all four heat transfer rates, lifting both $\dot{Q}_{eva}$ and $\dot{Q}_{gen}$ proportionally but with $\dot{Q}_{eva}$ rising slightly faster. Conversely, a colder chilled water return (Scenario 6) depresses the COP to 0.696 while producing a lower, more desirable $T_{chw,out}$ of 279.2 K. Second, the evaporator mass M_{eva} is the most sensitive state variable to $T_{cw,i}$ perturbations — ranging from 5.287 kg in Scenario 5 to 9.205 kg in Scenario 6, a variation of 74% — because the evaporator inventory is directly governed by the balance between the evaporation rate (set by $T_{cw,i}$) and the absorption draw rate, both of which are strongly modulated by the low-side pressure. This stands in contrast to the previous scenarios where M_{eva} was largely the most stable variable, confirming that $T_{cw,i}$ acts as the primary determinant of evaporator-side refrigerant inventory in the LiBr/H_2O cycle.

6.5 Comparative Discussion

The six step-change scenarios presented in Sections 6.2 through 6.4 collectively characterise the dynamic sensitivity of the single-effect LiBr/H_2O absorption chiller model to perturbations in its three primary thermal boundary inputs: the hot water inlet temperature $T_{hw,i}$, the cooling water inlet temperature $T_{clw,i}$, and the chilled water inlet temperature $T_{cw,i}$. Each input was perturbed by ±5 K or ±3 K from its nominal value, and the system was allowed to reach a new steady state in each case. This section synthesises the results across all scenarios to establish a ranked understanding of input sensitivity, compare transient characteristics, and confirm the overall robustness of the simulation model.

6.5.1 Master Steady-State Comparison

Table 11 presents the complete set of steady-state output values across all six scenarios alongside the nominal baseline, enabling a direct cross-scenario comparison of the chiller's response to each class of perturbation.

Table 11 - Master steady-state comparison across all scenarios

Parameter	Nominal	S1: $T_{hw,i}$=363K	S2: $T_{hw,i}$= 373K	S3: $T_{clw,i}$=309 K	S4: $T_{clw,i}$=301 K	S5: $T_{cw,i}$=291K	S6: $T_{cw,i}$=285K
$T_{hw,out}$(K)	360.7	356.5	364.9	362.0	359.4	360.2	361.2
$T_{cw,out(abs)}$(K)	308.5	308.2	308.9	311.9	305.2	308.8	308.3
$T_{cw,out(con)}$(K)	311.2	310.6	311.9	314.0	308.5	311.8	310.7
$T_{chw,out}$(K)	281.5	282.2	280.8	282.9	280.1	283.9	279.2
X_{strong}(wt%)	59.61	58.30	60.90	59.22	60.00	58.90	60.31
X_{weak}(wt%)	56.13	55.25	56.98	56.52	55.73	55.09	57.16
ΔX(wt%)	3.48	3.05	3.92	2.70	4.27	3.81	3.15
M_{gen}(kg)	19.22	24.17	14.26	14.20	23.35	15.95	22.64
M_{abs}(kg)	37.49	33.32	41.79	42.63	33.18	41.95	32.97
M_{con}(kg)	3.48	2.772	4.210	1.739	6.087	4.318	2.687
M_{eva}(kg)	7.31	7.239	7.235	8.936	4.886	5.287	9.205
$\dot{Q}_{gen}$(W)	9788	8753	10819	8024	11549	10483	9091
$\dot{Q}_{eva}$(W)	7031	6272	7781	5491	8576	7748	6324
$\dot{Q}_{con}$(W)	7370	6558	8173	5755	8990	8102	6644
$\dot{Q}_{abs}$(W)	9574	8563	10577	7857	11284	10258	8891
COP	**0.718**	**0.716**	**0.719**	**0.684**	**0.742**	**0.739**	**0.696**

6.5.2 Input Sensitivity Ranking

The three inputs produce distinctly different sensitivities across the key performance indicators, and a clear hierarchy emerges from the data in Table 10.

Coefficient of Performance.

The cooling water inlet temperature $T_{clw,i}$ is by far the dominant driver of COP variation, producing a range of 0.684–0.742 — a spread of 0.058 — across Scenarios 3 and 4. The chilled water inlet temperature $T_{cw,i}$ produces an intermediate range of 0.696–0.739 (spread of 0.043) across Scenarios 5 and 6. The hot water inlet temperature $T_{hw,i}$, by contrast, produces a negligible COP variation of only 0.716–0.719 (spread of 0.003) across Scenarios 1 and 2 — essentially invariant within the ±5 K perturbation range. This hierarchy arises because COP in a single-effect absorption chiller is fundamentally governed by the ratio of the evaporator heat load to the generator heat input, and both $T_{clw,i}$ and $T_{cw,i}$ influence the low-pressure side equilibrium directly, while $T_{hw,i}$ scales $\dot{Q}_{gen}$ and $\dot{Q}_{eva}$ nearly proportionally, leaving their ratio unchanged.

Chilled Water Outlet Temperature.

The chilled water inlet temperature $T_{cw,i}$ produces the largest absolute swing in $T_{chw,out}$, ranging from 279.2 K to 283.9 K — a total spread of 4.7 K — across Scenarios 5 and 6. The cooling water inlet temperature $T_{clw,i}$ produces a spread of 2.8 K (280.1 K to 282.9 K), and the hot water inlet temperature $T_{hw,i}$ produces the smallest spread of 1.4 K (280.8 K to 282.2 K). This ranking reflects the directness of the coupling between the chilled water stream and the evaporator: $T_{cw,i}$ sets the evaporator inlet condition directly, and any perturbation propagates immediately into $T_{chw,out}$ with minimal attenuation. The $T_{clw,i}$ influence is indirect — mediated through the condenser and absorber pressures before reaching the evaporator — while the $T_{hw,i}$ influence is the most distal, reaching the evaporator only through the generator desorption rate and subsequent refrigerant circulation.

Concentration Difference ΔX

The cooling water inlet temperature $T_{clw,i}$ produces the widest range of ΔX variation, from 2.70 wt% (Scenario 3) to 4.27 wt% (Scenario 4) — a spread of 1.57 wt%. The hot water inlet temperature $T_{hw,i}$ produces a spread of 0.87 wt% (3.05–3.92 wt%), and the chilled water inlet temperature $T_{cw,i}$ produces the narrowest spread of 0.66 wt% (3.15–3.81 wt%). A higher ΔX is generally associated with a stronger absorption driving force and greater refrigerant throughput, and the dominance of $T_{clw,i}$ in controlling ΔX confirms that the heat sink temperature governs the fundamental thermodynamic lift of the cycle more powerfully than either the heat source or load temperatures.

6.5.3 Component Mass Sensitivity

The mass redistribution patterns across scenarios reveal which components act as the primary refrigerant and solution buffers under each type of perturbation. The generator mass M_{gen} is most sensitive to $T_{hw,i}$ perturbations, ranging from 14.26 kg (Scenario 2) to 24.17 kg (Scenario 1) — a variation of 66% relative to nominal — because the generator is the direct thermal interface with the hot water stream and its solution inventory is governed by the balance between hot-side heat input and strong solution outflow. The condenser mass M_{con} is most sensitive to $T_{clw,i}$ perturbations, varying by a factor of 3.5 from 1.739 kg (Scenario 3) to 6.087 kg (Scenario 4), reflecting the strong nonlinear dependence of condensate accumulation on the saturation conditions set by the cooling water temperature. The evaporator mass M_{eva} is most sensitive to $T_{cw,i}$ perturbations, ranging from 5.287 kg (Scenario 5) to 9.205 kg (Scenario 6) — a variation of 74% — because the evaporator refrigerant inventory is directly governed by the balance between evaporation rate and absorption draw rate, both of which are strongly modulated by the low-side pressure set by $T_{cw,i}$. This component-specific sensitivity pattern is physically coherent and confirms that each thermal boundary input primarily governs the component it is thermodynamically closest to, with secondary effects propagating through the rest of the cycle.

6.5.4 Transient Dynamics Comparison

Beyond steady-state values, the six scenarios reveal consistent patterns in transient behaviour that have implications for control system design. The $T_{clw,i}$ perturbations (Scenarios 3 and 4) exhibit the fastest settling times of approximately 3000–5000 s, as the cooling side heat exchangers have relatively low thermal mass and the pressure-mediated coupling between the condenser and absorber allows rapid re-equilibration. The $T_{hw,i}$ perturbations (Scenarios 1 and 2) exhibit the slowest settling times of approximately 12000–15000 s, reflecting the large thermal inertia of the generator — the most massive solution-containing component — and the finite transport delays introduced by the discretised 8-stage solution heat exchanger model. The $T_{cw,i}$ perturbations (Scenarios 5 and 6) produce intermediate settling times but are distinguished by the most pronounced transient overshoots in $T_{chw,out}$, a consequence of the direct and immediate coupling between the chilled water stream and the evaporator pressure before the absorption side can respond.

A recurring transient feature across multiple scenarios is the brief opposite-direction spike in $T_{cw,out(con)}$ immediately following the step change — an undershoot in Scenario 3 and an overshoot in Scenario 4, and similar signatures in Scenarios 1, 2, 5, and 6. This phenomenon consistently reflects the momentary decoupling between the condenser heat load and the cooling water outlet temperature during the interval between the step application and the establishment of the new vapour generation rate equilibrium, and its reproducibility across all six scenarios confirms that it is a genuine dynamic feature of the model rather than a numerical artefact.

6.5.5 Model Robustness and Conservation Validation

A critical validation observation spans all six scenarios: in every case, the total system mass $M_{gen} + M_{abs} + M_{con} + M_{eva}$ converges to 67.50 ± 0.01 kg at the new steady state, confirming strict conservation of mass across all perturbations and all simulation durations. All variables converge to physically meaningful, thermodynamically consistent steady states — no scenario produced crystallisation risk (all concentrations remained below 62 wt%), negative masses, or pressure inversions. The numerical stability of the solver was maintained throughout all six transients, including at the moment of the instantaneous step change itself, validating the effectiveness of the dynamic condenser pressure scaling mechanism and the discretised SHX model introduced in Chapter 4. The consistency of the conservation checks and the physical interpretability of every transient feature together confirm that the model delivers reliable, high-fidelity dynamic predictions across a representative operating envelope of the single-effect LiBr/H_2O absorption chiller.

7 Conclusion

This thesis set out to develop, implement, and analyse a dynamic lumped-parameter simulation model of a single-effect lithium bromide-water ($LiBr/H_2O$) absorption chiller in the MATLAB/Simulink environment, motivated by the need for computationally efficient tools capable of predicting the transient behaviour of absorption cooling systems driven by low-grade thermal energy. Four objectives were defined at the outset: the derivation of a complete set of governing dynamic equations from first principles; the implementation of the model with the architectural modifications necessary for numerical stability; the subsystem-level modular verification of each component before full integration; and the systematic investigation of the model's dynamic behaviour under a nominal baseline and six parametric step-change scenarios. All four objectives have been successfully met.

A thermodynamically consistent dynamic model was derived for all seven subsystems — generator, absorber, condenser, evaporator, solution heat exchanger, throttle valves, and solution pump — grounded in the strict conservation of mass, species, and energy. The thermophysical property library, drawing on the correlations of Pátek and Klomfar (2006), Florides et al. (2003), and Kaita (2001), provided accurate and continuous evaluation of $LiBr/H_2O$ vapour pressure, enthalpy, specific heat capacity, and density across the full operating range, with refrigerant saturation temperatures recovered from pressure via the Antoine equation. Two targeted architectural modifications to the baseline state-space framework of Wen et al. (2019) were essential to achieving sustained operation. The dynamic condenser pressure scaling mechanism self-regulates refrigerant flow during severe transients including cold-start, preventing the solver divergence that afflicts conventional fixed-pressure formulations. The 8-stage spatially discretised counter-flow solution heat exchanger model, incorporating finite thermal mass at each stage, accurately captures the transport delays and heat recovery dynamics that quasi-steady approximations cannot reproduce under transient conditions. The modular construction methodology ensured that thermodynamic errors were identified and corrected at the component level before system integration, and the fully integrated model was confirmed to conserve total system mass to within rounding precision — $M_{gen} + M_{abs} + M_{con} + M_{eva} = 67.50 \pm 0.01$ kg — across all operating conditions.

The systematic investigation of six step-change scenarios across three input variables produced a clear and physically coherent sensitivity hierarchy. The cooling water inlet temperature $T_{clw,i}$ emerged as the dominant driver of COP variation, producing a range of

0.684–0.742 across a ±4 K perturbation. The chilled water inlet temperature $T_{cw,i}$ produced the largest absolute swing in chilled water outlet temperature $T_{chw,out}$ of 4.7 K and was the primary determinant of evaporator-side refrigerant inventory, with M_{eva} varying by 74% between its two scenarios. The hot water inlet temperature $T_{hw,i}$, while directly governing refrigerant production rate, left the COP nearly invariant at 0.716–0.719 across a ±5 K perturbation, as $\dot{Q}_{gen}$ and $\dot{Q}_{eva}$ scaled proportionally. All six step changes produced physically interpretable transient features and converged to thermodynamically consistent steady states, confirming that the model captures the nonlinear dynamic coupling between subsystems with fidelity.

Several limitations of the present work should be acknowledged. The lumped-parameter formulation cannot resolve internal spatial gradients or falling-film phenomena within components, no crystallisation prevention logic was implemented, and the solution pump frequency was held constant throughout all simulations. Future work should prioritise the integration of a feedback control layer — such as a PID or model predictive control scheme — to regulate $T_{chw,out}$ under varying load conditions, leveraging the dynamic model directly as the plant. Extension to a double-effect cycle, investigation of variable pump frequency as a control input, and experimental validation against a physical test rig represent further natural directions for development. Ultimately, the model developed in this thesis delivers a robust, computationally efficient, and physically transparent tool for predicting the complex transient behaviour of single-effect LiBr/H_2O absorption cooling systems providing a solid foundation for future control design and system optimisation studies.

References

[1] G. A. Florides, S. A. Kalogirou, S. A. Tassou, and L. C. Wrobel, 'Design and construction of a LiBr–water absorption machine', *Energy Convers. Manag.*, vol. 44, no. 15, pp. 2483–2508, Sep. 2003, doi: 10.1016/S0196-8904(03)00006-2.

[2] W. Salmi, J. Vanttola, M. Elg, M. Kuosa, and R. Lahdelma, 'Using waste heat of ship as energy source for an absorption refrigeration system', *Appl. Therm. Eng.*, vol. 115, pp. 501–516, Mar. 2017, doi: 10.1016/j.applthermaleng.2016.12.131.

[3] H. T. Chua, H. K. Toh, A. Malek, K. C. Ng, and K. Srinivasan, 'Improved thermodynamic property fields of LiBr-H2O solution', 2000.

[4] H. Wen, A. Wu, Z. Liu, and Y. Shang, 'A State-Space Model for Dynamic Simulation of a Single-Effect LiBr/H_2 O Absorption Chiller', *IEEE Access*, vol. 7, pp. 57251–57258, 2019, doi: 10.1109/ACCESS.2019.2913657.

[5] J. Pátek and J. Klomfar, 'A computationally effective formulation of the thermodynamic properties of LiBr–H2O solutions from 273 to 500K over full composition range', *Int. J. Refrig.*, vol. 29, no. 4, pp. 566–578, Jun. 2006, doi: 10.1016/j.ijrefrig.2005.10.007.

[6] S. Garimella, A. M. Brown, and A. K. Nagavarapu, 'Waste heat driven absorption/vapor-compression cascade refrigeration system for megawatt scale, high-flux, low-temperature cooling', *Int. J. Refrig.*, vol. 34, no. 8, pp. 1776–1785, Dec. 2011, doi: 10.1016/j.ijrefrig.2011.05.017.

[7] G. Evola, N. Le Pierrès, F. Boudehenn, and P. Papillon, 'Proposal and validation of a model for the dynamic simulation of a solar-assisted single-stage LiBr/water absorption chiller', *Int. J. Refrig.*, vol. 36, no. 3, pp. 1015–1028, May 2013, doi: 10.1016/j.ijrefrig.2012.10.013.

[8] Y. Kaita, 'Thermodynamic properties of lithium bromide–water solutions at high temperatures', *Int. J. Refrig.*, vol. 24, no. 5, pp. 374–390, Aug. 2001, doi: 10.1016/S0140-7007(00)00039-6.

[9] M. Arnaudo, J. Dalgren, M. Topel, and B. Laumert, 'Waste heat recovery in low temperature networks versus domestic heat pumps - A techno-economic and environmental analysis', *Energy*, vol. 219, p. 119675, Mar. 2021, doi: 10.1016/j.energy.2020.119675.

[10] C. T. Misenheimer and S. D. Terry, 'The development of a dynamic single effect, lithium bromide absorption chiller model with enhanced generator fidelity', *Energy Convers. Manag.*, vol. 150, pp. 574–587, Oct. 2017, doi: 10.1016/j.enconman.2017.08.005.

[11] G. Gediz Ilis, H. Demir, and B. B. Saha, ‘Analysis of operation and construction parameters for adsorption chiller performance with MATLAB/Simulink simulation’, *Appl. Therm. Eng.*, vol. 198, p. 117499, Nov. 2021, doi: 10.1016/j.applthermaleng.2021.117499.

[12] R. Muhumuza and P. Strachan, ‘Modelling, Implementation and Simulation of a Single-Effect Absorption Chiller in MERIT’, *2010*, 2010, [Online]. Available: https://scispace.com/pdf/modelling-implementation-and-simulation-of-a-single-effect-1jic7icpob.pdf

[13] Y. Zhou, L. Pan, X. Han, and L. Sun, ‘Dynamic modeling and thermodynamic analysis of lithium bromide absorption refrigeration system using Modelica’, *Appl. Therm. Eng.*, vol. 225, p. 120106, May 2023, doi: 10.1016/j.applthermaleng.2023.120106.

[14] P. Kohlenbach and F. Ziegler, ‘A dynamic simulation model for transient absorption chiller performance. Part I: The model’, *Int. J. Refrig.*, vol. 31, no. 2, pp. 217–225, Mar. 2008, doi: 10.1016/j.ijrefrig.2007.06.009.

[15] P. Kohlenbach and F. Ziegler, ‘A dynamic simulation model for transient absorption chiller performance. Part II: Numerical results and experimental verification’, *Int. J. Refrig.*, vol. 31, no. 2, pp. 226–233, Mar. 2008, doi: 10.1016/j.ijrefrig.2007.06.010.

[16] Eric W. Lemmon, Ian H. Bell, Marcia L. Huber, and Mark O. McLinden, ‘REFPROP Documentation’, 2018, [Online]. Available: https://www.nist.gov/document/refprop10apdf

[17] O. Marc, F. Sinama, J.-P. Praene, F. Lucas, and J. Castaing-Lasvignottes, ‘Dynamic modeling and experimental validation elements of a 30 kW LiBr/H2O single effect absorption chiller for solar application’, *Appl. Therm. Eng.*, vol. 90, pp. 980–993, Nov. 2015, doi: 10.1016/j.applthermaleng.2015.07.067.

[18] R. Turnbull and T. Muneer, ‘A Two Year Comparison of Energy and CO2 Emissions of an Industrial Refrigeration Plant after the Installation of a Waste Heat Recovery System’, *Energy Procedia*, vol. 161, pp. 251–258, Mar. 2019, doi: 10.1016/j.egypro.2019.02.089.

[19] A. Mahmoudi, M. Fazli, and M. R. Morad, ‘A recent review of waste heat recovery by Organic Rankine Cycle’, *Appl. Therm. Eng.*, vol. 143, pp. 660–675, Oct. 2018, doi: 10.1016/j.applthermaleng.2018.07.136.